# UC Santa Cruz

## UC Santa Cruz Electronic Theses and Dissertations

### Title

Improving Ocean-Monitoring Satellite and Airborne Sensor Validation

### Permalink

https://escholarship.org/uc/item/90k4p9qw

### Author

Bausell, Jesse

### Publication Date

2020

### Copyright Information

This work is made available under the terms of a Creative Commons Attribution License, availalbe at https://creativecommons.org/licenses/by/4.0/

Peer reviewed|Thesis/dissertation

eScholarship.org Powered by the California Digital Library
University of California

UNIVERSITY OF CALIFORNIA

SANTA CRUZ

# IMPROVING OCEAN-MONITORING SATELLITE AND AIRBORNE SENSOR VALLIDATION

A dissertation submitted in partial satisfaction
of the requirements for the degree of

DOCTOR OF PHILOSOPHY

in

OCEAN SCIENCES

by

**Jesse T. Bausell**

June 2020

The dissertation of Jesse T. Bausell is approved:

_____
Professor Raphael Kudela, Chair

_____
Professor Christopher Edwards

_____
Dr. John Ryan

_____
Quentin Williams
Acting Vice Provost and Dean of Graduate Studies

## Table of Contents

**List of Tables……iv**

**List of Figures……v**

**Executive Summary……vi**

**Acknowledgements……ix**

**INTRODUCTION……1**

**Chapter 1: COMPARISON OF TWO IN-WATER OPTICAL PROFILERS IN A DYNAMIC COASTAL MARINE ECOSYSTEM……10**

- **Abstract……10**
1. **Introduction……11**
2. **Methods……14**
3. **Results……30**
4. **Discussion……37**
5. **Conclusion……44**
6. **References……46**

**Chapter 2: STUCTURALLY EVALUATING END-MEMBER APPROACH, AN EMPIRICAL OCEAN COLOR METHOD FOR ESTIMATING $a_{CDOM}(440)$……52**

- **Abstract……52**
1. **Introduction……53**
2. **Methods……59**
3. **Results……72**
4. **Discussion……81**
5. **Conclusion……90**
6. **References……92**

**Chapter 3: COMPARISON OF DIFFERENT AC-S SCATTERING CORRECTION APPROACHES FOR IMPROVING OPTICAL CLOSURE IN A DYNAMIC COASTAL MARINE ECOSYSTEM……98**

- **Abstract……98**
1. **Introduction……99**
2. **Methods……105**
3. **Results……114**
4. **Discussion……123**
5. **Conclusion……129**
6. **References……131**

**CONCLUSION……135**

## List of Tables

**Chapter 1: COMPARISON OF TWO IN-WATER OPTICAL PROFILERS IN A DYNAMIC COASTAL MARINE ECOSYSTEM**

**Table 1. Hydrolight 5.3 Settings……26**
**Table 2. Station Sea Surface Biomass Descriptors……32**

**Chapter 2: STUCTURALLY EVALUATING END-MEMBER APPROACH, AN EMPIRICAL OCEAN COLOR METHOD FOR ESTIMATING $a_{CDOM}(440)$**

**Table 1. Hydrolight 5.3 Settings ……67**
**Table 2. K-means overview.……78**
**Table 3. Standard deviation of residuals (RMSE).……86**

**Chapter 3: COMPARISON OF DIFFERENT AC-S SCATTERING CORRECTION APPROACHES FOR IMPROVING OPTICAL CLOSURE IN A DYNAMIC COASTAL MARINE ECOSYSTEM**

**Table 1. Scattering Correction Approaches.……108**
**Table 2. Hydrolight 5.3 Settings.……112**
**Table 3. Scattering Correction Approach RMSE by station.……115**
**Table 4. Station Sea Surface Biomass Descriptors.……124**

## List of Figures

**Chapter 1: COMPARISON OF TWO IN-WATER OPTICAL PROFILERS IN A DYNAMIC COASTAL MARINE ECOSYSTEM**

**Figure 1. Map of Monterey Bay……16**
**Figure 2. Normalized water-leaving radiances: spectral……32**
**Figure 3. Normalized water-leaving radiances: absolute percent difference……33**
**Figure 4. Normalized water-leaving radiances: cast variability……33**
**Figure 5. Depth profiles: backscattering and chlorophyll……35**
**Figure 6. Depth profiles: reflectance……36**
**Figure 7. Optical Depth (490 nm) across stations……36**
**Figure 8. Normalized water-leaving radiances: CST17……41**

**Chapter 2: STUCTURALLY EVALUATING END-MEMBER APPROACH, AN EMPIRICAL OCEAN COLOR METHOD FOR ESTIMATING $a_{CDOM}(440)$**

**Figure 1. Map of NOMAD stations……61**
**Figure 2. Probability density functions: bio-optical constituents……64**
**Figure 3. Linear regression: bio-optical constituents……65**
**Figure 4. Spectral absorption and scattering components……71**
**Figure 5. Least-squares regression: phase functions……73**
**Figure 6. Least-squares regression: bootstrapped means……74**
**Figure 7. Box plots: IOP components (443 nm)……75**
**Figure 8. Ternary plots: absorption components (443 nm)……76**
**Figure 9. Least-squares regression: "conservative" ecosystems……80**
**Figure 10. Comparison of "non-conservative" ecosystems……80**
**Figure 11. Absorption vs. scatter (443 nm)……86**

**Chapter 3: COMPARISON OF DIFFERENT AC-S SCATTERING CORRECTION APPROACHES FOR IMPROVING OPTICAL CLOSURE IN A DYNAMIC COASTAL MARINE ECOSYSTEM**

**Figure 1. Diagram of WET Labs ac-s……102**
**Figure 2. Normalized water-leaving radiances: spectral……117**
**Figure 3. Normalized water-leaving radiances: selected spectra…118**
**Figure 4. Normalized water-leaving radiances: absolute percent difference……120**
**Figure 5. Comparisons of near surface spectral absorptions……122**
**Figure 6. Comparisons of near surface spectral backscattering……123**

## Executive Summary

**Jesse Turner Towson Bausell**

## IMPROVING OCEAN-MONITORING SATELLITE AND AIRBORNE SENSOR VALLIDATION

Ocean-monitoring satellites and airborne sensors characterize ecosystem bio-optical properties spatially. Predicated on radiative transfer theory, these sensors measure ecosystem watermass light fields from above, from which bio-optical data products are derived with the help of optical algorithms. These above-water sensors, however, are subject to uncertainties in their radiometric data products that are caused by atmospheric correction, environmental perturbations, and long-term degradation of the sensors themselves. What is more, optical algorithms contribute an additional layer of ecosystem-specific uncertainties. Because of this uncertainty, above-water sensors must be "validated" with ground truth radiometric measurements sampled from the ecosystems they seek to characterize. These measurements are traditionally obtained using in-water optical profilers (profilers), negatively buoyant radiometers that measure light fields, also known as apparent optical properties (AOPs), through the water column *in-situ*. Profilers are also important in the development of novel algorithms, as well as the validation of their bio-optical data products. My dissertation investigates the effectiveness of profilers in characterizing coastal (and by extension) inland ecosystems, as well as how to improve validation activities in these systems.

Our capacity to validate above-water sensors using profilers alone is limited, especially in coastal and inland ecosystems. Chapter 1 of this dissertation demonstrates that different commercially available profiler models are not comparable in a coastal ecosystem. High optical sensor sensitivity and vertical resolution are necessary for accurately measuring coastal (and inland) ecosystems. High spectral resolution is also important for validation, as profiler and above-water sensor channels need to be centered on similar wavelengths ($\lambda$). However, different profilers exhibit tradeoffs in these attributes, affording them limited capability for validating above-water sensors in coastal and inland ecosystems. Chapter 3 addresses the issue of profiler tradeoffs by demonstrating that accurate and reliable AOPs can be modeled above-water hyperspectrally, thus enabling the validation of above-water sensor channels in the visible. By evaluating an empirical algorithm using modeled data, Chapter 2 provides insight into the underlying factors responsible for the algorithm's varying levels success across different ecosystems. Applied broadly, Chapter 2 methodology can help determine which types of ecosystems and at which $\lambda$'s a particular algorithm is most likely to work.

With the advent of next-generation satellite sensors and unmanned aerial vehicles, my findings will advance our ability to characterize coastal and inland ecosystems. Chapter 2 will enable investigators to make informed decisions with

regard to selecting appropriate algorithm(s) and an above-water sensor in order to characterize an aquatic ecosystem of interest. By modeling AOPs hyperspectrally, Chapter 3 will improve the validation of the above-water sensor by ensuring that $\lambda$'s of validation data products align with the channels of the aforementioned sensor.

**Acknowledgements**

I could not have completed this dissertation without the support and encouragement of many individuals dedicated to education and the pursuit of science. First and foremost, I'd like to thank my faculty advisor, Professor Raphael Kudela (UC Santa Cruz), for his steadfast commitment to my research and his example of excellence that I strive to live up to. I will always appreciate the amount of time and effort that Professor Kudela has invested in making me a better scientist. I'd also like to thank my doctoral committee members, Professor Christopher Edwards (UC Santa Cruz) and Dr. John Ryan (MBARI), for their guidance and advice, as well as the countless hours they have invested in me, as I progressed through my doctorate. I'd be remiss if not to acknowledge the many courses that I took with Professor Edwards, which gave me a strong foundational knowledge in physical oceanography and the python programing language. I'd also like to thank Professor Edward's postdoctoral researcher, Dr. Jann Paul Mattern, for his important role in teaching me python.

Additionally, I would like to thank the Kudela Laboratory and its members past and present for their continued support, especially Ms. Kendra Hayashi Negrey for her leadership in running the day-to-day laboratory operations. Ms. Negrey was also instrumental in collecting much of the data on which Chapter 1 and 3 rely. I would be remiss not to thank Dr. Stanford Hooker (NASA Goddard) and

the staff at Biospherical Instruments for inviting me to participate in NASA's HARPOONS field campaign. Dr. Hooker and Mr. James Brown (U. Miami) also allowed me to access their software program, PROSIT, which was essential to my first chapter. Finally, I'd like to thank Dr. Liane Guild (NASA AMES) for her helpfulness and mentorship during my doctoral studies.

Finally, I would like to express my personal gratitude to Mr. Joel Wilson and Mr. Matthew Crawford, as well the members of Santa Cruz Masters Swimming and UCSC Swimming and Diving Teams, for their continued friendship and support. An additional heartfelt thank you to Rabbi Shlomo Chein of the Chabad Jewish Student Center for the spiritual guidance that he provides to me, fellow UCSC students, and Santa Cruz residents alike.

## INTRODUCTION

The ability of ocean-monitoring satellites and airborne sensors to characterize bio-optical properties spatially makes them increasingly important and ubiquitous in oceanographic research. These above-water sensors measure light fields, or "apparent optical properties" (AOPs) of watermasses as they emanate upwards [1, 2]. Bio-optical properties, such as concentrations of chlorophyll (Chl), colored dissolved organic material (CDOM), and total suspended matter (TSM), are estimated from these radiometric measurements with the help of optical algorithms [3-5]. These above-water sensors operate under the assumptions of radiative transfer theory [6]. Governing the propagation of light through a medium, radiative transfer theory assumes that absorption and scatter of bio-optical constituents are wavelength ($\lambda$) dependent, and that these "inherent optical properties" (IOPs) in turn impact AOPs [7, 8].

Collectively known as "validation activities", there are several considerations to take into account with regard to satellite and airborne imagery. These data must be corrected for atmospheric contamination, which can account for as much as 90% of the raw optical signal at the top of the atmosphere [9]. Investigators must also track the level of certainty in above-water sensor measurements and their algorithmic data products, and whether it changes over time. Otherwise, degradation of above-water sensors over the course of their lifespan can be

conflated with long-term biogeochemical trends in aquatic ecosystems [10]. These considerations are compounded by the fact that the level of certainty of satellites and their data products are ecosystem dependent [11]. Sensors therefore require ground truth measurements sampled within the aquatic ecosystems they seek to characterize. To this end, in-water optical profilers or "profilers", provide radiometric measurements that are directly comparable to above-water sensors. Negatively buoyant, these radiometers measure AOPs in-situ through the water column that are then extrapolated across the air-sea interface (sea surface) in order to calculate above-water AOPs, such as remote sensing reflectance ($R_{rs}(\lambda)$) and normalized water-leaving radiance ($[L_W(\lambda)]_N$). These measurements are directly comparable with satellite and airborne measurements and thus can be used for validation.

To date, several commercially available profilers are in use by the ocean color community. These profilers differ in their design specifications and consequently sample aquatic ecosystems at different vertical and spectral resolutions, and at different sensitivities [12, 13]. Moreover, investigators typically deploy only one profiler at a study site (e.g., [7, 14]). It is therefore unclear whether measurements from different profilers are comparable to one another and if this comparability varies from one ecosystem to the next. This question of interchangeability between above-water AOPs (e.g., $[L_W(\lambda)]_N$ and $R_{rs}(\lambda)$) measured with different profilers has important implications for constructing

datasets with which to validate above-water sensors. Chapter 1 seeks to address this by comparing $[L_W(\lambda)]_N$ measured by two profilers at five sampling stations in Monterey Bay, CA. A semi-enclosed embayment on the Central California Coast, Monterey Bay affords the opportunity to compare profilers within a range of biologically and optically distinct watermasses, not unlike different ecosystems. These watermasses range from those characterized by low phytoplankton biomass, located in the center of the bay, to those entrained into the northern bay where conditions commonly favor moderate to intense phytoplankton blooms [15, 16]. The two profilers, Compact Optical Profiling System (C-OPS) and HyperPro II (HP2) embody a classic tradeoff between spectral and vertical resolution. They are also compared at each station against $[L_W(\lambda)]_N$ modeled using Hydrolight, a software package that calculates AOPs according to radiative transfer theory. By comparing similarities between measured and modeled $[L_W(\lambda)]_N$, we can determine whether profiler measurements are indeed representative of the watermass IOPs that they attempt to characterize, also known as optical closure.

By providing insight into the comparability of two profilers within coastal watermasses, Chapter 1 helps to ensure consistency between profiler-measured AOPs that comprise validation datasets for above-water sensors. In addition to validating radiometric measurements, these data are also important in the development and validation of optical algorithms within different ecosystems

(e.g., [17]). Utility of optical algorithms varies by ecosystem, but cannot necessarily be predicted by uncertainties associated radiometric measurements, as algorithms add an additional layer of uncertainty to the retrieval of bio-optical properties [18]. Furthermore, most datasets on which such algorithms are derived and validated are often heavily skewed towards one or a small subset of ecosystems. Even a demonstratively robust algorithm can be difficult to predict in a particular ecosystem without field sampling.

Algorithms cannot be validated everywhere, as field sampling is inevitably limited by monetary, logistical, and time constraints. Chapter 2 therefore explores an alterative approach to evaluating algorithms in order to gain insight into the undergirding mechanisms on which they rely and the factors that impact their success or failure in estimating a particular bio-optical property. This information could then be used to predict in which ecosystems a particular algorithm is likely to work. The ideal dataset with which to achieve these ends would possess in-situ AOPs and IOPs that achieve optical closure and that are representative of a diverse array of ecosystems in terms of their bio-optical properties. The International Ocean Colour Coordinating Group (IOCCG) provides two large datasets for evaluating algorithms: one that measures AOPs and IOPs in-situ across an array of ecosystems, and a second that models AOPs using Hydrolight. These data are subject to shortcomings, however, as in-situ measurements do not achieve optical closure due to measurement errors, and

IOPs that undergird the modeled data represent a limited range of ecosystem bio-optical properties.

Chapter 2 evaluates Hooker et al. [7]'s end-member approach (EMA), an empirical method that estimates CDOM absorption at 440 nm ($a_{CDOM}(440)$) using diffuse attenuation coefficient end-member ratios. To address the limitations of the IOCCG datasets, Chapter 2 models optical properties of 1000 "ecosystems" using Hydrolight. Bio-optical properties used to model these ecosystems were based off of distributions and relationships between Chl, $a_{CDOM}(443)$, and TSM measured at 538 stations as part of the NASA bio-optical Marine Algorithm Dataset (NOMAD). By employing Latin Hypercube sampling and Cholesky decomposition in conjunction with modeling, Chapter 2 ensures that EMA is evaluated with a dataset of AOPs and IOPs that meet optical closure and that are based off of realistic bio-optical properties, including those of extreme aquatic ecosystem types such as intense phytoplankton blooms and waterways with high suspended sediment concentrations. By evaluating EMA, Chapter 2 provides insight into its reliance on correlations between bio-optical constituents, its sensitivity to phase function, its ability to estimate $a_{CDOM}(440)$ in extreme environments, and how these factors differ with $\lambda$.

With the advent of next-generation satellite sensors and unmanned aerial vehicles (UAVs) that are better equipped to characterize coastal and inland

ecosystems, insights from Chapter 2 could be leveraged to select ecosystems to monitor. In this context, the need for reliable ground truth radiometry data with which to validate these sensors will be ever present. Chapter 1 concludes that while C-OPS, with its centimeter-scale vertical resolution and high signal to noise ratio, appears well equipped to measure these systems at particular bands, its spectral resolution is inadequate. C-OPS could therefore be problematic for validating above-water sensors that are hyperspectral (e.g., HICO) with channels that are not aligned with C-OPS.

To address this shortcoming, Chapter 3 explores the possibility of modeling hyperspectral $[L_W(\lambda)]_N$ in Monterey Bay. In Chapter 1, Hydrolight-modeled $[L_W(\lambda)]_N$ was based on in-situ absorption and attenuation, as well as backscattering measurements collected with a WET Labs absorption attenuation meter (ac-s) and a HOBI Labs Hydroscat-6 (HS6). Chapter 3 hypothesizes that previously reported (Chapter 1) shortcomings in optical closure between $[L_W(\lambda)]_N$ measured by C-OPS and modeled by Hydrolight (notably in the green) could be explained by ac-s' long optical pathlength. This pathlength causes overestimations and underestimations in absorption and attenuation measurements respectively, due to undetected scattering inside ac-s flow tubes. Chapter 3 evaluates a number of different approaches for correcting scatter inside ac-s absorption tube in an attempt to improve optical closure between Hydorlight and C-OPS $[L_W(\lambda)]_N$ at $\lambda$'s measured by the latter. This evaluation

was carried out at the Monterey Bay stations previously evaluated as part of Chapter 1. In doing so the chapter not only seeks to determine which SCA(s) works best in Monterey Bay, but also whether ac-s and HS6 can reliably characterize hyperspectral $[L_W(\lambda)]_N$ in Monterey Bay through modeling.

This dissertation seeks to enhance the capacity of the ocean color community to validate satellite and airborne sensors. It also examines the feasibility of determining the underlying optical factors on which an empirical method relies and how they can be used in predicting the utility of sensor-specific algorithms (based on $\lambda$) across ecosystem types. An overarching theme is the use of modeling to enhance the applicability of data measured in-situ, both in terms of their predictive capacity and their applicability to different sensors. As such, this dissertation holds the potential to improve our ability to validate radiometric and algorithmic data products of above-water sensors by 1) evaluating the ability of profilers to sample a coastal ecosystem, 2) enhancing the spectral resolution of radiometric data used for validation, and 3) identifying target ecosystems for validating data products of above-water sensors based on the potential utility of their algorithms.

**References**

1. S. Hooker, and J. Brown, "Processing of Radiometric Observations of Seawater using Information Technologies (PROSIT): In-Water User Manual," NASA, ed. (2013).

2. C. D. Mobley, "Estimation of the remote-sensing reflectance from above-surface measurements," Applied Optics **38**, 7442-7455 (1999).

3. M. G. Allan, D. P. Hamilton, B. J. Hicks, and L. Brabyn, "Landsat remote sensing of chlorophyll a concentrations in central North Island lakes of New Zealand," International Journal of Remote Sensing **32**, 2037-2055 (2011).

4. A. Hilton, J. Bausell, and R. Kudela, "Quantification of Polychlorinated Biphenyl (PCB) Concentration in San Francisco Bay Using Satellite Imagery," Remote Sensing **10**, 1110 (2018).

5. D. Siegel, S. Maritorena, N. Nelson, D. A. Hansell, and M. Lorenzi‐Kayser, "Global distribution and dynamics of colored dissolved and detrital organic materials," Journal of Geophysical Research: Oceans **107** (2002).

6. S. Chandrasekhar, *Radiative Transfer* (Dover Publications Inc, 1960).

7. S. Hooker, J. Morrow, and A. Matsuoka, "The 1% and 1 cm perspective in deriving and validating AOP data products," Biogeosciences Discussions **9** (2012).

8. M. S. Twardowski, E. Boss, J. M. Sullivan, and P. L. Donaghay, "Modeling the spectral shape of absorption by chromophoric dissolved organic matter," Marine Chemistry **89**, 69-88 (2004).

9. H. R. Gordon, "In-orbit calibration strategy for ocean color sensors," Remote sensing of Environment **63**, 265-278 (1998).

10. R. A. Barnes, D. K. Clark, W. E. Esaias, G. S. Fargion, G. C. Feldman, and C. R. McClain, "Development of a consistent multi-sensor global ocean colour time series," International Journal of Remote Sensing **24**, 4047-4064 (2003).

11. S. W. Bailey, and P. J. Werdell, "A multi-sensor approach for the on-orbit validation of ocean color satellite data products," Remote Sensing of Environment **102**, 12-23 (2006).

12. Biospherical Instruments Inc., "Compact Optical Profiling System: Hardware User's Manual (Doc 006406UA)," (2010).

13. Satlantic, "Operation Manual For: Profiler II Document Number: SAT-DN-00223," (2009).

14. S. L. Palacios, R. M. Kudela, L. S. Guild, K. H. Negrey, J. Torres-Perez, and J. Broughton, "Remote sensing of phytoplankton functional types in the coastal ocean from the HyspIRI Preparatory Flight Campaign," Remote Sensing of Environment **167**, 269-280 (2015).

15. W. Graham, J. Field, and D. Potts, "Persistent “upwelling shadows” and their influence on zooplankton distributions," Marine Biology **114**, 561-570 (1992).

16. L. K. Rosenfeld, F. B. Schwing, N. Garfield, and D. E. Tracy, "Bifurcated flow from an upwelling center: a cold water source for Monterey Bay," Continental Shelf Research **14**, 931-964 (1994).

17. S. B. Hooker, A. Matsuoka, R. M. Kudela, Y. Yamashita, K. Suzuki, and H. F. Houskeeper, "A Global End-Member Approach to Derive a CDOM (440) from Near-Surface Optical Measurements," Biogeosciences Discussions, 1-51 (2019).

18. M. J. Behrenfeld, and P. G. Falkowski, "Photosynthetic rates derived from satellite‐based chlorophyll concentration," Limnology and oceanography **42**, 1-20 (1997).

# <u>Chapter 1:</u> Comparison of two in-water optical profilers in a dynamic coastal marine ecosystem

Jesse Bausell & Dr. Raphael M. Kudela

## Abstract

We compared mean normalized water-leaving radiances ($[\overline{L_W}(\lambda)]_N$) of two in-water optical profilers, Compact Optical Profiling System (C-OPS) and HyperPro II Optical Profiler (HP2), with modeled $[\overline{L_W}(\lambda)]_N$ at five stations in Monterey Bay, CA. Although C-OPS and HP2 $[\overline{L_W}(\lambda)]_N$'s were mostly within one standard deviation, C-OPS and modeled $[\overline{L_W}(\lambda)]_N$ showed the lowest absolute percent differences ($\leq$ 25% for most wavelengths) at four of the stations. We attribute this to C-OPS's high vertical resolution (~1 cm), which is important for detecting changes in optical layers and for measuring the upper 0 - 0.5 m of the water column. HP2's low vertical resolution (~ 50 cm), low signal to noise ratio, and inability to measure the upper 0 - 0.5 m are problematic in Monterey Bay. Although a significant component of the $[\overline{\boldsymbol{L_W}}(\boldsymbol{\lambda})]_{\boldsymbol{N}}$ differences between C-OPS and HP2 likely stems from fluctuating watermass IOPs, the 25% error in $[\boldsymbol{L_W}(\boldsymbol{\lambda})]_{\boldsymbol{N}}$'s processed from HP2 casts, compared to < 1 % for C-OPS, is also important.

## 1. Introduction

In-water optical profilers are utilized by the ocean color community for a variety of purposes pertaining to validation and research. Examples include validating satellite data products (e.g. [1, 2]), developing and validating bio-optical and atmospheric correction algorithms (e.g., [3-6]), and modeling radiative transfer (e.g., [7]). These negatively buoyant radiometers measure apparent optical properties (AOPs), such as downwelling irradiance ($E_d(\lambda)$) and upwelling radiance ($L_u(\lambda)$) of watermasses in-situ, as they descend through the water column. They simultaneously measure above-water solar irradiance ($E_S(\lambda)$) using a solar reference sensor. Above-water AOPs are computed from these data by first using empirically derived attenuation coefficients to extrapolate AOP values directly below the air-sea interface, and then 'propagating' these values across this interface. Profiler-derived above-water AOPs can be directly compared to those measured via ocean color satellites and airborne imagers [8, 9]. Because they are derived directly from the water column however, these above-water AOPs are assumed to follow radiative transfer and thus to be representative of the inherent optical properties (IOPs) of their respective watermasses [4, 8]. For this reason, profiler-derived above-water AOPs are not subject to confounding factors, such as atmospheric contamination, sunglint, and mixed pixels that contaminate airborne and satellite imagery, underscoring their aforementioned importance in the field of ocean color [9-11].

Remote sensing of coastal marine ecosystems represents an ongoing challenge for the ocean color community. The watermasses that comprise these ecosystems are often characterized by high concentrations of bio-optical constituents (e.g., phytoplankton, dissolved organic

matter, and suspended particulate matter) which commonly do not co-vary [12]. Further contributing to watermass optical complexity, these constituents are often vertically stratified [13-15]. They also commonly fluctuate over spatial and temporal scales that are smaller than those for which most present-day satellite and airborne sensors are designed [16]. Moreover, coastal satellite and airborne imagery is more difficult to atmospherically correct than imagery from the open ocean owing to aerosols from nearby landmasses [17]. In-water optical profilers play a pivotal role in overcoming these obstacles. At present there are several profiler models in use that differ in their sampling frequencies, rates of descent, as well as the number, spectral locations, and sensitivity of the channels with which they sample (e.g., [18, 19]). These differences will inevitably impact the vertical and spectral resolutions at which different profilers sample and could in turn impact values of the above-water AOPs they derive.

Because bio-optical constituents in coastal watermasses are commonly stratified into distinct vertical layers [13, 14], vertical resolution at which an in-water optical profiler samples cannot be overlooked. The utility of an in-water optical profiler in deriving accurate above-water AOPs in coastal watermasses may lie in its ability to accurately characterize these layers optically. Indeed Hooker et al. [4] demonstrate that artificially offsetting a profiler's pressure transducer relative to its optical sensors can cause observational errors in above-water AOPs. Sensitivity to these offsets increases with optical complexity of vertical structure; 4 cm and 1 cm offsets induce significant errors in above-water AOPs in coastal and inland (e.g., estuarine, riverine) watermasses respectively. Pressure transducer offsets could

lead to mischaracterizations of the presence or position of these layers in the water column, as reflected by in-water AOP depth profiles. These errors could propagate through the derivation process of above-water AOPs [4, 8]. Intuitively, sampling the light field at low vertical resolution could lead to similar types of errors. This is supported by D'Alimonte et al. [20] who demonstrate that evaluating AOPs at depths corresponding to the beginning or end of sensor integration times (rather than means) can lead to over- and underestimations of the attenuation coefficients used to extrapolate above-water AOPs. D'Alimonte et al. [20] also demonstrate that higher vertical resolution obtained from either a single vertical profile with slower descent or faster integration time, or through the use of multicast profiles, increases precision of above-water AOPs by increasing the precision of regression products used to derive above-water radiances.

As magnitude reflects concentration and vertical structure of bio-optical constituents, spectral shape of above-water AOPs is indicative of the constituents themselves. Different bio-optical constituents can distinctly impact spectral shape of IOPs [21-23]. Because above-water AOPs are a function of these IOPs, their spectral shapes hold information on the biogeochemical composition of watermasses [6, 9, 24]. Spectral shapes of above-water AOPs can be used to detect ecological phenomena, such as red tides, and demonstrate potential in delineating phytoplankton community structure [5, 6, 24, 25]. On a more rudimentary level, spectral position of above-water AOP maxima experience a directional shift away from the blue and into the green and red in response to increasing optical complexity of watermasses [4, 5, 24]. While optimal spectral resolution of in-water optical profilers is ultimately dependent on

research goals, resolution reduction may come at the expense of the information that their above-water AOP spectra may contain.

Studies relying on above-water AOPs propagated from in-water measurements typically utilize only one in-water optical profiler (e.g., [4, 6, 7]). In doing so, much of the ocean color community makes the implicit assumption that these profilers are interchangeable irrespective of their sampling attributes and their tradeoffs [26]. We test this assumption by comparing two commercially available in-water optical profilers, the Compact Optical Profiling System (C-OPS) and HyperPro II Optical Profiler (HP2) across five sampling stations in a coastal marine ecosystem. To provide context, we also compare above-water AOPs measured with C-OPS and HP2 with above-water AOPs modeled using Hydrolight 5.3 (HE53). The goals of these comparisons are threefold: First, we compare the accuracy of C-OPS and HP2 in extrapolating above-water AOPs within a dynamic coastal marine ecosystem. Second, we provide insight into the origin of intra-profiler variability between successive downcasts. Finally, we account for discrepancies between C-OPS, HP2, and HE53 above-water AOPs for the same watermasses.

## 2. Methods

### *2.1 Overview of Study Site*

We compared HP2 and C-OPS at five sampling stations located in Monterey Bay, CA a non-estuarine, open embayment situated on California's central coast (Figure 1) [27, 28]. Stations were sampled as part of three NASA airborne campaigns, COAST

(CST), OCEANIA (OCE), and C-HARRIER (CHR), carried out 28 Oct. 2011, 05 Nov. 2013, and 08 Sept. 2017. Data collection adhered to the standards outlined in the NASA Ocean Optics Protocols [29, 30]. At each station we deployed C-OPS and HP2 as well as a WETLabs spectral absorption and attenuation meter (ac-s) and a HOBI Labs Hydroscat-6 spectral backscattering sensor (HS6), with an integrated SeaBird CTD. These instruments, referred to hence forth as the 'IOP Package' (IOP-P) were affixed to a metal cage and lowered (≥ 15 m) and raised multiple times through the water column in succession. We also measured surface chlorophyll concentrations (Chl) at each station. Due to logistical constraints of our research vessel (*R/V John Martin*), C-OPS, HP2 and IOP-P were not simultaneously deployed. *R/V John Martin's* engines were placed in neutral, allowing the vessel to drift for the duration of sampling, with the vessel relocated to the original sampling position after each cast. All stations except CHR1 were sampled under clear skies.

Sampling stations represent a range of optical properties associated with Monterey Bay watermasses. CHR2, OCE18, and CST18 are located in northeastern Monterey Bay (Fig. 1). Known as the upwelling shadow (US), this region is physically, chemically, and biologically distinct from the rest of the bay throughout most of the year (~March-November) due to a high residence time (~8-12 days), which resembles a semi-enclosed embayment [31, 32]. CST18 is outside the region typically considered the US, but strongly influenced by advective circulation from the US, and CST18 is therefore included with CHR2 and OCE18. Phytoplankton blooms are common in proximity to the US region. Our final two stations, CHR1 and CST17, are located in central Monterey Bay at the site of the former MBARI M0

mooring (M0) (Fig. 1). M0 is in the path of low-biomass, optically deep watermasses that intrude into the bay from Pt. Año Nuevo/Pt. Sur upwelling centers as well as from the offshore California Current System. The availability of in-situ IOPs enables us to model above-water AOPs using HE53's radiative transfer model. This enhances our ability to compare C-OPS and HP2 by providing an objective measure by which to evaluate the derived AOPs, as well as insight into the underlying basis for any discrepancies between profilers.

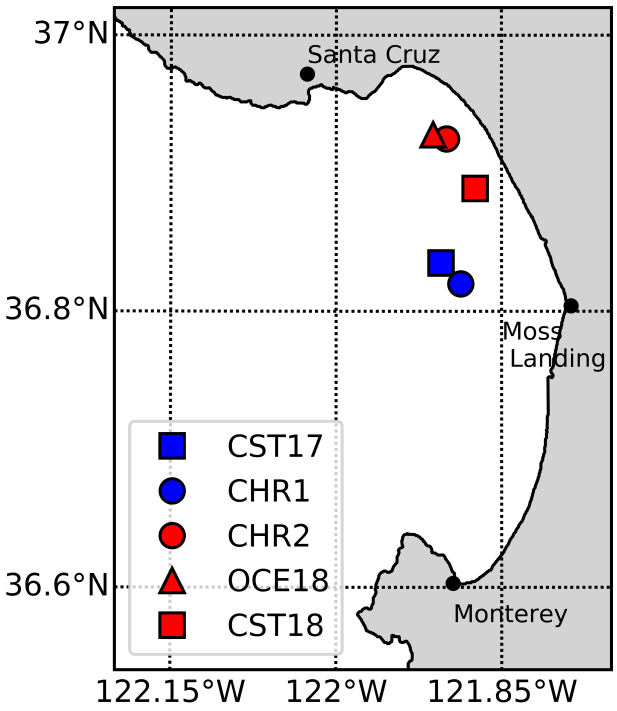



**Figure 1.** Map of Monterey Bay with M0 (blue) and US (red) stations. Marker shapes distinguish NASA airborne campaign.

*2.2 In-Water Optical Profilers*

*2.2.1 In-Water Optical Profilers: Instrumentation*

Manufactured by Biospherical Instruments, C-OPS is equipped with $L_u(\lambda)$ and $E_d(\lambda)$ sensors, as well as an above-water solar reference sensor for $E_S(\lambda)$. These are capable of synchronously sampling 19-20 channels centered 15-45 nm apart on user selectable wavelengths ($\lambda$'s) between 250-1100 nm. C-OPS is equipped with ancillary temperature, pressure, and tilt sensors. Its adjustable rate of descent (5-75 cm $s^{-1}$) coupled with a high-frequency and high sensitivity analog to digital converter (ADC) ($\leq$ 125 Hz; 24 bit) enables C-OPS to sample the water column at centimeter-scale vertical resolution [18]. Manufactured by Satlantic, HP2 also measures $L_u(\lambda)$, $E_d(\lambda)$, and $E_S(\lambda)$. Ancillary sensors include manufacturer-supplied CTD and tilt (pitch/roll) sensors, as well as a WET Labs ECO-BB2F-SAT combination backscatter meter and fluorometer, equipped with two channels centered at $\lambda$=470 & 700 nm, for the configuration used in this study. Compared to C-OPS, HP2 possesses low ADC sampling frequency (10 Hz) and sensitivity (16 bit) and thus low vertical resolution (~0.5 m) when combined with the manufacturer-specified minimum descent rate, which can be adjusted between 10-30 cm $s^{-1}$; its AOP sensors sample asynchronously. HP2 samples at much higher spectral resolution compared to C-OPS, providing 137 fixed channels spanning 350-800 nm and spaced ~3 nm apart [19]. However, this high spectral resolution is likely to come at a cost. Due to its high ADC frequency and slow rate of descent, C-OPS provides a typical vertical sample density of 100-150

measurements $m^{-1}$. On the other hand, HP2's higher descent rate and ADC frequency allow it to sample the water column at 2-3 measurements $m^{-1}$. This greatly increases HP2's susceptibility to large uncertainties for derived products [20].

An additional distinction between the two profilers is how they collect "dark" measurements, AOPs acquired in the absence of light used to calibrate raw data. HP2 typically collects dark measurements during data acquisition by incrementally 'shuttering', or blocking its sensors (although it can also be configured to use darks provided separately) [19]. C-OPS relies on 'deck corrections', running C-OPS pre- and post-sampling with lens caps attached to its sensors with dark values measured for each gain setting [18].

*2.2.2 In-Water Optical Profilers: Data Collection*

Prior to departure from Moss Landing Harbor, solar reference sensors are mounted above *R/V John Martin's* superstructure to prevent shading. Both profilers are placed in a shaded area on the ship deck during transit to the first sampling, in order to acclimate them to ambient environmental conditions. During the initial transit from Moss Landing Harbor, C-OPS 'dark measurements' are collected for several minutes (*section 2-B-3*). This is repeated post-sampling on the return trip to the harbor.

Deployment protocols are the same for C-OPS and HP2. Each in-water optical profiler is lowered off the side of *R/V John Martin.* The profiler is kept at the seasurface by gently

tugging at the telemetry cable, used to maintain physical and electronic contact with the *R/V John Martin* and kited away from the vessel by alternately providing slack and tension to the line. Casts are initiated by "popping" the $E_d(\lambda)$ sensor above the air-sea interface and then allowing the profiler to free-fall. Following "best practices" [18], we completed at least three to four separate casts for both in-water optical profilers at each station, with the exception of HP2 at CHR1 & 2, which was deployed in the *multi-cast* mode, during which HP2 is continuously profiled (free fall) and raised through the water column at least five times in rapid succession during data acquisition. Downcasts are combined and processed as a single cast to increase vertical resolution [33].

C-OPS and HP2 sampling frequencies were set to manufacturer-recommended defaults, 125 and 10 Hz respectively. 16 out of 19 C-OPS spectral channels were centered on the same $\lambda$'s for all five stations: 320, 340, 380, 395, 412, 443, 465, 490, 510, 532, 555, 625, 670, 683, 710, and 780 nm. During CST and OCE campaigns, two of the remaining three channels were centered on 560 and 665 nm; the third was configured to measure photosynthetically available radiation. C-OPS's remaining three channels were centered on 313, 589, and 875 nm for the CHR campaign.

*2.2.3 In-Water Optical Profilers: Data Processing*

Each in-water optical profiler cast is processed into a single normalized water-leaving radiance spectrum ($[L_W(\lambda)]_N$) employing *Processing of Radiometric Observations of Seawater using Information Technologies* (PROSIT), open source software

compatible with C-OPS and HP2 [8]. We processed only downcasts, or data acquired during the profiler's descent, referred to henceforth as *casts*. $[L_W(\lambda)]_N$ is an ideal above-water AOP for instrument comparisons. It accounts for solar geometry and variations in the atmosphere [34], minimizing differences between casts caused by short (typically <1 h) time intervals between deployments.

The processing is briefly described. First, cast data are uploaded into PROSIT, along with ancillary information: dark measurements, profiler specifications (e.g., sensor aperture diameters and offsets), and metadata, including latitude/longitude coordinates, start/stop time, and meteorological conditions. PROSIT then performs time-synchronization, pressure tare, dark calibration, tilt filtering (set at 5°), and a self-shading correction which utilizes measured Chl. User selects two AOP extrapolation intervals per cast: one in the blue-green, which we also used to process AOPs in the UV, and a second in the red-NIR [8]. Spectral attenuation coefficients, used to propagate AOPs across the sea-air interface and thus calculate above-water AOPs, are derived from these. PROSIT provides a graphical user interface with which users can visualize AOP data, select extrapolation intervals (the depth range over which measured in-water AOPs are used to extrapolate above-water AOPs), and examine statistical parameters associated with their selections [8]. Extrapolation intervals are selected to minimize relative percent differences (RPD) between $E_S(\lambda)$, as measured by solar reference sensors, and $E_d(\lambda)$, as propagated above-water through the air-sea interface.

In order to ensure protocol consistency, we selected extrapolation intervals according to standards outlined in Hooker et al. [8]. To summarize, for each cast we ensured that both extrapolation intervals share the same upper depth boundary, which we selected to be as close to the sea surface as possible. Lower depth boundaries are permitted to differ from one another. In selecting extrapolation intervals we attempted to optimize agreement between $E_d(\lambda)$ extrapolated and propagated above the sea surface and $E_S(\lambda)$ as measured by the profiler's solar reference sensor. We discarded discrete profiler casts if RPD < 25% in either the UV-green or the red-NIR could not be achieved. We also attempted to maximize linearity of (natural log-transformed) $E_d(\lambda)$ and $L_u(\lambda)$ within their boundaries. HP2 *multi-cast* data, collected at each CHR station, were processed both as one combined cast and separately as individual casts (*single-cast*). C-OPS cast extrapolation intervals typically contained > 50 in-water AOP measurements. Extrapolation intervals for HP2 in single-cast mode contained 3-4 measurements over the extrapolation interval, determined by the requirement that the extrapolation depth was similar for both C-OPS and HP2 for each station. Extrapolation intervals for HP2 multi-casts contained 14-18 measurements within the same depth range as for single-cast.

As previously mentioned (*section 2-B-1*), we calibrated C-OPS with dark measurements collected pre- and post-sampling. These measurements are temperature-dependent, creating an additional source of uncertainty with regard to C-OPS data. The impact of using pre- versus post-sampling dark measurements was negligible. Notwithstanding, we did observe that C-OPS dark measurements exceeded $\lambda$-dependent factory specified noise equivalent

signals for $E_d(\lambda)$ (0.8-9.0 x $10^{-6}$ $\mu$m $cm^{-2}$ $nm^{-1}$) and $L_u(\lambda)$ (0.68-5.0 x $10^{-6}$ $\mu$m $cm^{-2}$ $nm^{-1}$ $sr^{-1}$) sensors by a factor of three for some stations. Noise equivalent $E_d(\lambda)$ and $L_u(\lambda)$ for HP2 is estimiated to be -0.6-2.8 x $10^{-}$` $\mu$m $cm^{-2}$ $nm^{-1}$ and 0.36-4.8 $10^{-3}$ $\mu$m $cm^{-2}$ $nm^{-1}$ $sr^{-1}$, several orders of magnitude larger than C-OPS. Thus we propagated these uncertainties through data processing steps to examine the cumulative impact on $[L_W(\lambda)]_N$.

### *2.3 IOPs and Chl*

#### *2.3.1 IOPs and Chl: Instrumentation*

IOP-P is comprised of an ac-s and HS6, with an integrated CTD. Manufactured by WETlabs Inc., the ac-s measures spectral absorption ($a(\lambda)$) and attenuation ($c(\lambda)$) at 87-89 channels (instrument dependent) via two separate flow chambers, one for each parameter. Channels are centered between 3-4 nm apart and span 400-728/736 nm (instrument dependent). The ac-s was deployed with a Seabird SeaCAT CTD [35]. HS6, produced by HOBI Labs, measures the volume scattering function (VSF) at a single angle, 140°, from which it estimates backscattering coefficients at six channels ($\lambda$= 420, 442, 470, 510, 590, and 700 nm) [36]. The ac-s was equipped with an integrated Seabird MicroCAT CTD used for conductivity, temperature, and depth; the HS6 was equipped with a separate pressure sensor. We measured Chl as described below.

*2.3.2 IOPs and Chl: Data Collection*

Prior to each field campaign, we determined $a(\lambda)$ and $c(\lambda)$ of pure water by running deionized water through the ac-s flow chambers. To deploy, the IOP-P is lowered several meters into the water column using *R/V John Martin's* motorized winch to "debubble" the flow chambers. Data acquisition is initiated and the IOP-P is raised and lowered through the water column 3-4 times in succession. Similar to HP2's *multi-cast* mode, the ac-s and HS6 record continuously.

We sampled Chl using methods outlined in Kudela et al. [37]. Seawater is collected using a bucket pre-rinsed three times with ambient seawater. After mixing bucket contents thoroughly, three 250 mL seawater aliquots are filtered under low vacuum onto Whatman Glass Fiber Filters (GF/F; nominally 0.7 μm) and stored on dry ice for transit to the laboratory. Chlorophyll is extracted and measured following the non-acidification technique outlined in Welschmeyer [38]. We calibrated our Turner Designs 10-AU fluorometer using a Turner Designs Chl standard, which was verified using a spectrophotometric method (Arar [39]). We also sampled Chl at discrete depths ($\leq$ 15 m) for CST stations using Niskin bottles.

*2.3.3 IOPs and Chl: Data Processing*

As with C-OPS and HP2, we only processed IOP downcasts. Because the ac-s uses two holographic gratings, raw individual $a(\lambda)$ and $c(\lambda)$ commonly exhibit offsets, or

'jumps' between channels 41 and 42 (~553-557 nm) at CST and OCE. To correct these, we estimated offsets for each $a(\lambda)$ and $c(\lambda)$ by interpolating $a$ and $c$ at channel 42. For this we used Matlab's *spline* function, designating the preceding three channels (39-41) as inputs. We then calculated differences between measured and interpolated values at channel 42 and added them to the upper halves (channel $\geq$ 42) of their $a(\lambda)$ or $c(\lambda)$. We adhered to the same protocol for CHR, calculating offsets between channels 46 and 47 (~582-585 nm). Next we performed a series of calibrations and corrections on raw ac-s data. We first performed a pure-water calibration by subtracting pure-water $a(\lambda)$ and $c(\lambda)$ from ac-s data (*section 2-C-2*). We then corrected for biases caused by temperature ($T$) and salinity ($S$) [40], as well as scattering [41]. Finally, we grouped and averaged $a(\lambda)$'s and $c(\lambda)$'s by 0.5 m depth bins. Processed $a(\lambda)$ and $c(\lambda)$ pairs are excluded from binning if either contains a negative or aberrantly large value, which we defined as an order of magnitude larger than its two neighboring spectra. We also discarded a pair should $a(\lambda) > c(\lambda)$ at the same $\lambda$.

We processed raw HS6 backscattering coefficients by first subtracting pure water backscattering, approximated using Morel [42], yielding particulate backscattering ($b_{bp}(\lambda)$). Because of the HS6's long optical pathlength, $b_{bp}(\lambda)$'s are subject to absorption and scattering-induced error [36]. Known as sigma-correction, we corrected for these errors using methods prescribed in Doxaran et al. [43], which leverage aforementioned bin-averaged $a(\lambda)$ ($\bar{a}(\lambda)$), sampled concurrently with

$b_{bp}(\lambda)$. Each $b_{bp}(\lambda)$ was sigma-corrected using the $\bar{a}(\lambda)$ that encompassed the depth bin at which it was sampled. Processed $b_{bp}(\lambda)$'s were grouped into 0.5 m depth bins.

*2.4 Modeling $[L_W(\lambda)]_N$ with Hydrolight*

To provide context for our in-water optical profiler comparison, we modeled $[L_W(\lambda)]_N$ using HE53, proprietary software that completes radiative transfer, for two reasons: 1. To determine whether profilers achieve optical closure, and 2. To model uncertainty in $[L_W(\lambda)]_N$ associated with low vertical resolution, such as that of HP2 (~0.5 m). Specifying 'Measured IOPs', which relies on depth-binned, field-sampled IOP spectra ($a(\lambda)$, $c(\lambda)$, and $b_{bp}(\lambda)$) in order to define watermass IOPs, we ran HE53 100 times for each station using bootstrapping with replacement [44]. To summarize, we first grouped individual IOP spectra according to the 0.5 m depth bin in which they were sampled (e.g., 0-0.5 m, 0.5-1 m, etc.). Second we randomly drew $n$ IOP spectra from a given depth bin, with $n$ corresponding to the total number of spectra sampled within that bin. These spectra were drawn one at a time and subsequently returned to the selection pool immediately following their drawing. This enables the same IOP spectrum to be selected multiple times. We then averaged our $n$ randomly selected IOP spectra. Upon repeating this process twice for each depth bin, once for $a(\lambda)$ and $c(\lambda)$ (corresponding spectra are paired and selected together) and a second time for $b_{bp}(\lambda)$, we input depth-binned IOP spectra into HE53, which we ran using the settings laid out in Table 1. Aside from depth-binned IOP spectra, which we re-sampled for each of our 100 HE53 runs, all other HE53 settings remained the same

for each station. We limited $[L_W(\lambda)]_N$ outputs to 400-715 nm due to the inability of the ac-s and HS6 to sample in the UV, as well as limitations associated with the Rottgers et al. [41] scattering correction.

**Table 1. HE53 Settings**

| Parameter | Setting | Input Source | Notes |
|---|---|---|---|
| $a(\lambda)\&c(\lambda)$ | User-input $a(\lambda)\&c(\lambda)$ | Depth-binned ac-s data file | Section 2-D |
| Phase Function | Fournier-Forand subroutine w/ user-input $b_{bp}(\lambda)/b(\lambda)$[1] | Depth-binned HS6 data file | Section 2-D |
| Inelastic Scatter | Chl Fluorescence (No Raman Scatter) | Surface Chl (GF/F) | Constant w/ depth |
| $T$ & $S$ | User-input | Seabird SeaCAT CTD | Constant w/ depth |
| Sky Model#1 | RADTRAN-X subroutine w/ user-input $E_S(\lambda)$ | HP2 solar reference sensor | Partitions into direct & diffuse irradiances |
| Sky Model#2 | HCNRAD subroutine | Date/GMT/ LAT/LON of station | Computes sky radiance from solar angle & irradiances |
| ATM[2] | Air Pressure/ Humidity/wind speed | WeatherHawk wind meter | Measured at Santa Cruz Wharf |
| Output $\lambda$ | Range: 400-715 nm Resolution: 3 nm | --- | --- |
| Output Depth | Range: 0-16 m Resolution: 0.5 m | --- | --- |
| Bottom Boundary | Infinite | --- | IOPs constant below 16 m |

[1] $b(\lambda) = c(\lambda) - a(\lambda)$
[2] Atmospheric/Meteorological Parameters

*2.5 Modeling $[L_W(\lambda)]_N$ with Hydrolight*

We used two approaches to compare $[L_W(\lambda)]_N$ of our profilers across the five sampling stations. First, we compared mean $[L_W(\lambda)]_N$ ($[\overline{L_W}(\lambda)]_N$) across three

instrument types (C-OPS, HP2, and IOP-P/HE53) at each station. We did this by plotting $[\overline{L_W}(\lambda)]_N$'s, along with their upper and lower boundaries of standard deviation ($\sigma_{Lwn}(\lambda)$) from the mean. Second, we examined the absolute percent differences (APD) of $[\overline{L_W}(\lambda)]_N$'s, one for each matchup between two instrument types. Although we plotted hyperspectral $[L_W(\lambda)]_N$ for HP2 and HE53 in order to compare their spectral shapes (e.g. Figs. 2 & 6), we limited our $[L_W(\lambda)]_N$ comparisons to C-OPS-centered $\lambda$'s (*section 2-B-2*). Because AOPs are $\lambda$-dependent [4, 5] they must be compared at consistent $\lambda$'s, thus C-OPS's low spectral resolution for any cross-instrument $[\overline{L_W}(\lambda)]_N$ comparison. In instances where HP2 and HE53 $[L_W(\lambda)]_N$ did not align fully with C-OPS-centered $\lambda$'s (offsets < 2 nm), we interpolated using Matlab's (Mathworks) "spline" function (*section 2-C-3*). All interpolated HP2 and HE53 $[L_W(\lambda)]_N$ values could be overlaid directly with actual spectra, as shown in Figs. 2 & 6. At CHR stations, we plotted both single and multi-cast HP2 $[\overline{L_W}(\lambda)]_N$. APD comparisons were calculated using multi-cast HP2 $[\overline{L_W}(\lambda)]_N$, although we also calculated APD between single vs. multi-cast for HP2. $[\overline{L_W}(\lambda)]_N$ and APD approaches allow qualitative and quantitative evaluations of agreement between profilers. For this we defined qualitative agreement as overlap between $[\overline{L_W}(\lambda)]_N \pm \sigma_{Lwn}(\lambda)$ of the two profilers. Similarly, we defined optical closure as agreement between HE53 and a profiler (e.g., between measured and modeled AOPs).

To contextualize $[L_W(\lambda)]_N$ variability, both across instrument types as well as between successive casts of the same instrument type, we compared $\sigma_{Lwn}(\lambda)$. As before, we limited $\sigma_{Lwn}(\lambda)$ comparisons to C-OPS-centered $\lambda$'s. We also examined depth profiles (henceforth profiles) of $b_{bp}(\lambda)$ at 470 nm ($b_{bp}(470)$) measured with HP2 and IOP-P (C-OPS lacks $b_{bp}(470)$), as well as HP2-measured Chl profiles (*section* 2-B-1). We retroactively calibrated WET Labs ECO-BB2F-SAT fluorescence by fitting an exponential equation ($R^2$>0.9) to fluorescence values paired with discrete Chl samples (*section 2-C-2*) collected similar depths. For this we used data sampled at CST stations due to the availability of Niskin-sampled Chl and the deployment of HP2 after collection of Chl samples. To minimize elapsed time between paired measurements, we used fluorescence sampled by the first HP2 cast (cast 1). At OCE18, CHR1, and CHR2 we took the difference between discrete Chl and HP2 (cast 1) surface Chl and used this value as an offset to calibrate HP2 Chl profiles. Lastly, we compared in-water radiance reflectance profiles at 490 nm ($R(490,z)$ across C-OPS, HP2, and HE53, calculated as:

$$R(490,z) = \frac{L_u(490,z)}{E_d(490,z)} \qquad (1)$$

where $E_d(490,z)$ and $L_u(490,z)$ denote processed (*section 2-B-3*) $E_d(\lambda)$ and $L_u(\lambda)$ at $\lambda$=490 nm and depth $z$. We computed $R(490,z)$ for C-OPS casts by dividing depth-binned (0.1 m) $L_u(490,z)$ and $E_d(490,z)$. For HP2 casts, we used a nearest-neighbor approach with respect to depth to match asynchronously sampled $E_d(490,z)$ and $L_u(490,z)$, placing $R(490,z)$ midway between the depths. We also

calculated $R(490, z)$ for each HE53 run at depths of 1-16 m. We excluded $R(490,0)$ and $R(490,0.5)$, as ac-s and HS6 could not reliably sample IOPs at depths $\leq$ 0.5 m. $R(490, z)$ provides insight as to whether $[L_W(\lambda)]_N$ discrepancies reflect watermass IOPs.

Finally, we contrasted bio-optical properties across stations by examining mean surface Chl (*section 2-C-2*) and mean optical depth at 490 nm ($\overline{\mathrm{OD}}_{490}$) calculated as:

$$\overline{OD}_{490} = \frac{1}{N}\sum_{i=1}^{N}\frac{1}{K_d(490)_i} \qquad (2)$$

where $K_d(490)$ is diffuse attenuation coefficient at $\lambda$=490 nm of C-OPS casts, as processed by PROSIT, $i$ is cast number, and $N$ is the number of casts per station. We chose C-OPS because of its centimeter-scale vertical resolution and the higher ADC conversion rates. $\overline{\mathrm{OD}}_{490}$ is a proxy for watermass bio-optical constituents [45]. It is also correlated with optical depth of photosynthetically available radiation across coastal watermasses [46]. To determine whether discrepancies in profiler $[\overline{L_W}(\lambda)]_N$ are driven by concentrations of bio-optical constituents present in the water column, we used weighted least squares to compare $\mathrm{OD}_{490}$ against absolute percent difference ($APD$), and absolute difference of C-OPS and HP2 $[\overline{L_W}(490)]_N$ across our five stations.

## 3. Results

With the exception of CST18 at $\boldsymbol{\lambda}$ = 412, 443, & 510 nm and CHR1 at $\boldsymbol{\lambda}$ < 600 nm, C-OPS and HP2 exhibit qualitative agreement. We cannot determine overlap between multi and single-cast HP2 at CHR stations, but $[\overline{\boldsymbol{L_W}}(\boldsymbol{\lambda})]_{\boldsymbol{N}}$ differences between them in the visible appear very small. Multi-cast HP2 does greatly reduce noise in the NIR and UV, however (Fig. 2). We also note that we discarded several CHR single casts (casts 3-5 at CHR1 and cast 5 at CHR2) consistent with *section 2-B-3*. Optical closure with at least one profiler is achieved in the blue and red at four of our five stations, the only exception being CHR2 and OCE18 at $\boldsymbol{\lambda}$ = 412 (Fig. 2). For CHR1, optical closure is not achieved for several $\boldsymbol{\lambda}$'s in the blue (Fig. 2). Optical closure is not achieved in the green for either profiler, with HE53 underestimating $[L_W(\lambda)]_N$. Despite this, HP2 and HE53 do exhibit similar spectral shapes across all five stations, as HE53 successfully characterizes spectral locations of $[L_W(\lambda)]_N$ maxima relative to HP2. Across stations we observe two general patterns in spectral shape. M0 $[L_W(\lambda)]_N$ increases more or less linearly from the UV-green, while US $[L_W(\lambda)]_N$ increases concavely over the same range. US stations exhibit diminished blue $[L_W(\lambda)]_N$, relative to M0, but more pronounced fluorescence peaks (addressed in *section 4*) (Fig. 2). These shapes may be related to surface phytoplankton biomass. Chl at M0 stations was 2-17 times lower than US station Chl. Additionally, M0 $\overline{\mathrm{OD}}_{490}$'s, (which overlap by one standard deviation) are 2-5 times greater than those of US stations, depending on the station (Table 2).

Except for multi vs. single-cast, which exhibits the lowest APD (excluding the NIR), C-OPS vs. HE53 shows the best quantitative agreement between $[\overline{L_W}(\lambda)]_N$ across four of five stations; this is followed by C-OPS vs. HP2 (Fig. 3a-d). The only consistent exception to this pattern is the lower C-OPS vs. HP2 APD in the green, notably at $\boldsymbol{\lambda}$ = 555 & 560 nm (Fig. 3a-d), corresponds to HE53's underestimating $[L_W(\lambda)]_N$ in the green (Fig. 2). APD also accentuates differences associated with low $[\overline{L_W}(\lambda)]_N$'s, which could explain our second exception, HP2 vs. HE53's APD being lowest in the red at OCE18 (Figs. 2d & 3d). CST18 exhibits a different pattern with regard to APD. C-OPS vs. HE53 still shows the best quantitative agreement in the blue, but APD is much higher than for the other stations (> 23%) and remains high across most of the spectrum. C_OPS vs. HP2 is especially poor in the blue (> 50%); except for a handful of $\lambda$'s it remains > 25%. HP2 vs. HE53 is inconsistent across the visible (Fig. 3e). C-OPS and HP2 $\sigma_{Lwn}(\lambda)$ are consistently larger, often several times so, than HE53 across all stations (Fig. 4). Nevertheless, no clear hierarchy is identified between C-OPS and HP2 $\sigma_{Lwn}(\lambda)$ across stations, except for CST17 where HP2 $\sigma_{Lwn}(\lambda)$ is substantially greater than C-OPS. Although C-OPS's noise-equivalent signals were negligible. HP2 noise can account for 25% of diffuse attenuation coefficient ($K_d(\lambda)$) and $[L_W(\lambda)]_N$ signals, meaning that HP2 $\sigma_{Lwn}(\lambda)$ (Fig. 4) may be artifact.

**Table 2. Station Sea surface Biomass Descriptors**

| Station | $\overline{\text{Chl}}$ (mg L$^{-1}$) | $\overline{OD}_{490}$ (m) | Location |
|---|---|---|---|
| CST17 | 6.81±0.275 | 3.72±0.43 | M0 |
| CHR1 | 3.13±0.016 | 3.92±0.31 | M0 |
| OCE18 | 12.31±0.01 | 1.89±0.87 | US |
| CHR2 | 17.64±0.35 | 2.04±0.02 | US |
| CST18 | 52.84±0.62 | 0.75±0.12 | US |

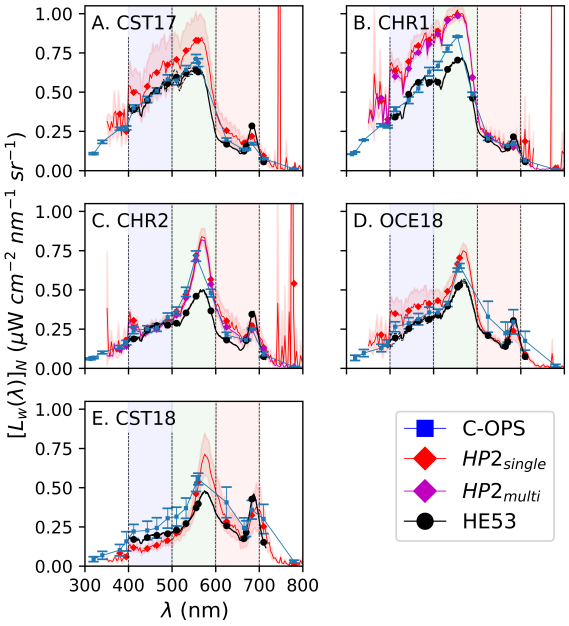



**Figure 2.** $[\overline{L_W}(\lambda)]_N \pm \sigma_{Lwn}(\lambda)$ for C-OPS (error bars), HP2 (red shading), and HE53 (bin = 0.5 m) (dashed lines). Markers denote C-OPS centered $\lambda$'s.

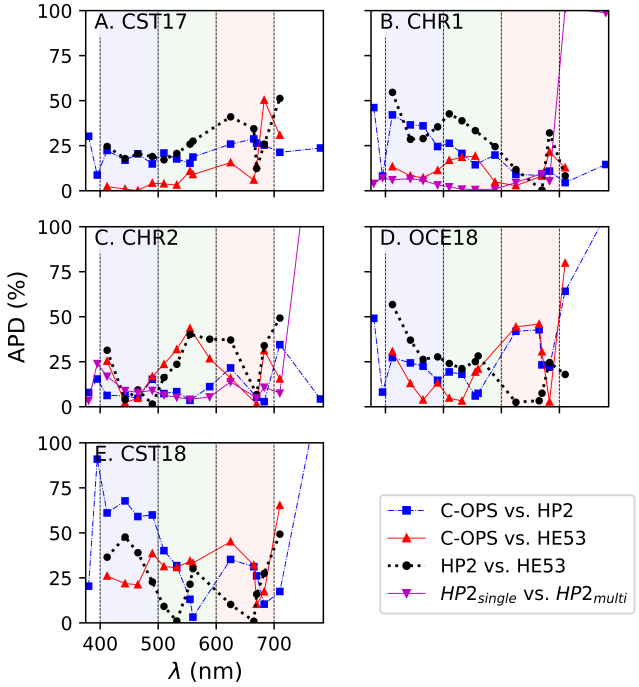



**Figure 3.** Comparison of $[\overline{L_W}(\lambda)]_N$'s for C-OPS, HP2, and HE53 (bin = 0.5 m) at C-OPS-centered $\lambda$'s using APD.

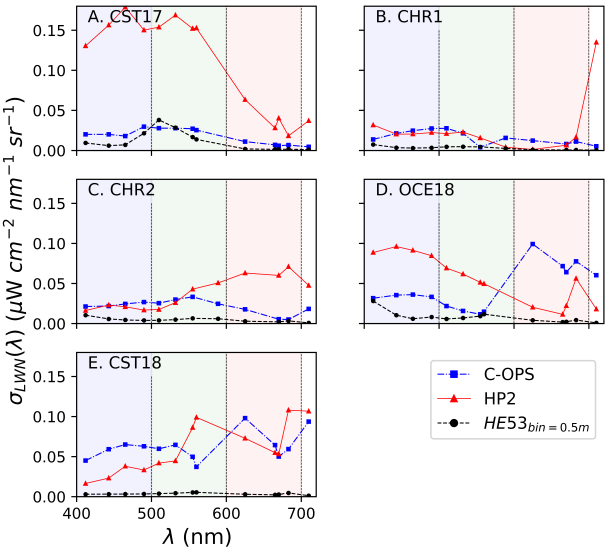



**Figure 4.** $\sigma_{Lwn}(\lambda)$ comparison of bootstrapped HE53-modeled C-OPS, and HP2. Blue, green, and red spectral ranges are shaded by their respective colors. HP2 $\sigma_{Lwn}(\lambda)$ at CHR1 & CHR2 calculated from partitioned single casts.

HP2 $b_{bp}(470)$ and Chl profiles exhibit similar trends in shape and magnitude, both within and across stations, implying that $b_{bp}(470)$ is likely linked to phytoplankton (Fig. 5). CST17 and CHR1 $b_{bp}(470)$ profiles are relatively consistent with depth. HP2 $b_{bp}(470)$ profiles are less than IOP-P profiles at both stations, exhibiting a ~ 0.001- 0.002 $m^{-1}$ offset. In the upper 1.5 m of the water column of CST17 however, there is an abrupt increase in $b_{bp}(470)$ for HP2 cast 1 (which overlaps with IOP-P) and similar decreases in $b_{bp}(470)$ for HP2 casts 2 & 3 (Fig. 5a&b). The absence of these trends in Chl profiles suggests that they are not directly tied to phytoplankton. We are unsure whether they are artifacts or fluctuations in watermass IOPs, which could have explained the high HP2 $\sigma_{Lwn}(\lambda)$ at CST17. Unlike $b_{bp}(470)$, HP2 $R(490, z)$ profiles at CST17 are highly variable, crisscrossing with both C-OPS and HE53 $R(490, z)$ through most of the water column (Fig. 6a). Similar to $b_{bp}(470)$, HP2 $R(490, z)$ profiles are offset from those of HE53 (and C-OPS) at CHR1 (Figs. 5b & 6b). For CHR2 and OCE18 $b_{bp}(470)$ and $R(490, z)$, profiles overlap in upper water columns. At CHR2 both $b_{bp}(470)$ and $R(490, z)$ profiles (measured by HP2 and IOP-P) diverge below 6 m. $b_{bp}(470)$ profiles re-converge at ~15 m, but $R(490, z)$ profiles do not (Figs. 5c & 6c). Despite no observed overlap in HP2 and IOP-P OCE18 $b_{bp}(470) > 3$ m, HP2 and HE53 $R(490, z)$ profiles overlap over most of the water column. C-OPS $R(490, z)$ profiles appear more similar to those of HP2 than HE53 at both CHR2 and OCE18 (Figs. 5d & 6d). At CST18 HP2 and IOP-P $b_{bp}(470)$ differ for depths < 6 m. HP2 cast 1 detects a subsurface (~2-6 m) $b_{bp}(470)$ maximum (Fig. 5e). This maximum is also present in HP2 cast 1 Chl and $R(490, z)$ profiles (Fig. 5e). $b_{bp}(470)$ and

$R(490, z)$ profiles measured by HP2 casts 2 & 3 do not detect a maximum, instead resembling those of IOP-P/HE53 (Figs. 5e, & 6e). A subsurface maximum is detected however by discrete Chl, collected prior to HP2, as well as C-OPS cast 3 $R(490, z)$, sampled directly prior to Niksin bottles (Figs. 5e & 6e). We observe no relationship between $\mathrm{OD}_{490}$ and APD (Fig. 7a), nor $\mathrm{OD}_{490}$ and absolute difference between C-OPS and HP2 $[\overline{L_W}(490)]_N$(Fig. 7b) across stations.

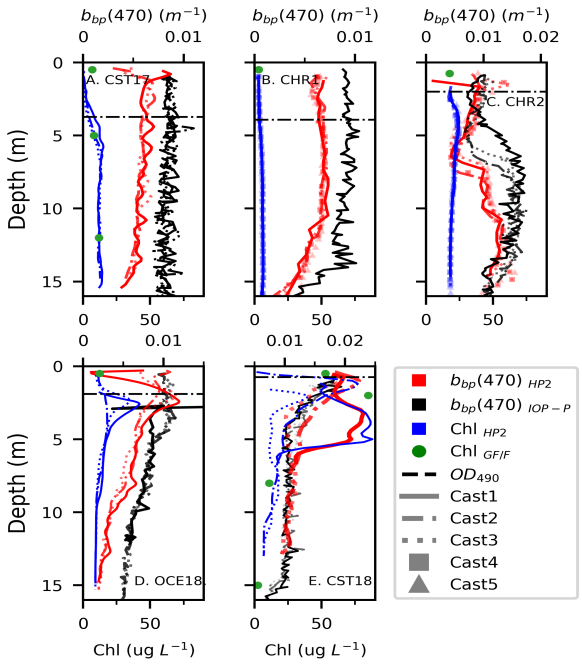



**Figure 5.** HP2 and IOP-P $b_{bp}(470)$ profiles overlaid with Chl profiles, GF/F Chl, and $\overline{\mathrm{OD}}_{490}$. Sequentially ordered casts are denoted by their line texture and by degree of shading (darkest to lightest).

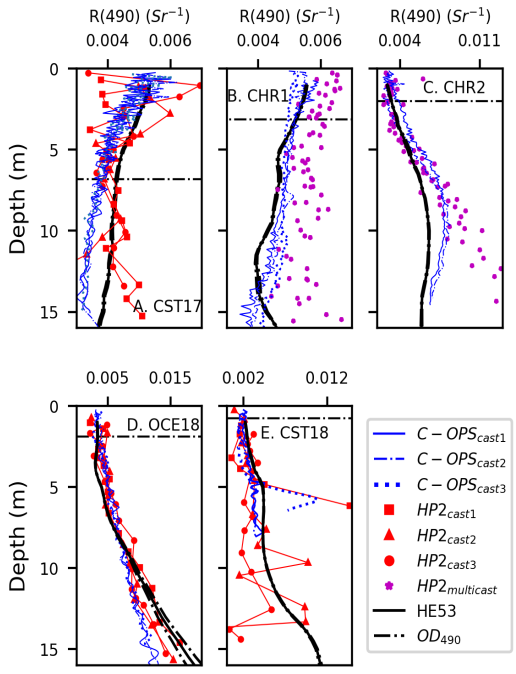



**Figure 6.** Comparison of $R(490, z)$ profiles and $\overline{\mathrm{OD}}_{490}$ at each station. C-OPS and HP2 profiles (single casts) are displayed individually, HP2 multi-cast profiles combined, and HE53 profiles are displayed as mean +/- standard deviation (dashed line).

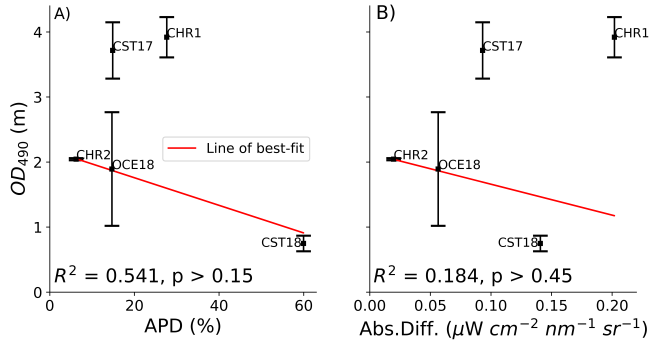



**Figure 7.** Cross-station comparison of $\mathrm{OD}_{490}$ (with standard deviation error bars) and $[\overline{L_W}(490)]_N$ discrepancies between C-OPS and HP2 expressed in terms of APD (a) and absolute difference (b). Weighted-least squares best-fit lines, coefficients of determination ($R^2$) and p-values (p) are displayed on each panel.

## 4. Discussion

The green as well as secondary red $[L_W(\lambda)]_N$ maxima we observe across our stations are characteristic of coastal watermasses, likely the result of increased turbidity and chlorophyll fluorescence [4, 47]. We also infer this from Spyrakos et al. 's [47] classification of 4045 above-water AOPs, which identifies two k-means clusters, C6 and I1, that respectively resemble M0 and US spectral shapes. I1 watermasses exhibit high chlorophyll and turbidity. This is in line with our suggestion that elevated phytoplankton concentrations, which lead to increased $a(\lambda)$ in the blue and fluorescence in the red, are primarily responsible for $[L_W(\lambda)]_N$ spectral shape differences between M0 and US stations [22, 23]. Similarities between spectral shapes (Fig. 2) and high instances of overlap in the blue and red between HP2 and HE53 $[L_W(\lambda)]_N$'s further support this suggestion. They also indicate that HP2 $[L_W(\lambda)]_N$ is representative of watermass IOPs. Qualitative comparisons however, indicate that for C-OPS-centered $\lambda$'s C-OPS is not only most representative of watermass AOPs, but also that $[\overline{L_W}(\lambda)]_N$'s for C-OPS and HE53's have a higher degree of similarity than for C-OPS and HP2.

The low C-OPS vs. HE53 APD relative to C-OPS vs. HP2 and HP2 vs. HE53, coupled with the comparatively low $\sigma_{Lwn}(\lambda)$ of bootstrapped HE53 $[L_W(\lambda)]_N$'s suggests that theoretically, a profiler with 0.5 m depth resolution is should be able to adequately characterize Monterey Bay watermasses (Fig. 4). Additionally, lack of a consistent hierarchy between C-OPS and HP2 $\sigma_{Lwn}(\lambda)$ and our inability to establish a relationship between

$\overline{\mathrm{OD}}_{490}$ and profiler $[\overline{L_W}(490)]_N$ disparities across stations (Figs. 3 & 5) reiterate that both profilers exhibit comparable variability between casts and that neither this variability nor profiler $[\overline{L_W}(\lambda)]_N$ discrepancies can be directly attributed to $\overline{\mathrm{OD}}_{490}$, or more broadly, bio-optical constituent concentrations in the water column (Figs. 2, 3, & 5; Table 2). Moreover, CHR1 and CST18, the stations with the poorest agreement between C-OPS and HP2 $[\overline{L_W}(\lambda)]_N$, exhibit the highest and lowest $\overline{\mathrm{OD}}_{490}$'s respectively.

While broad trends in optical properties cannot explain discrepancies in profiler $[\overline{L_W}(\lambda)]_N$ and $\sigma_{Lwn}(\lambda)$ across stations, they do in large part account for these discrepancies within stations. The relationships between IOPs and above-water AOPs can be approximated by:

$$R_{rs}(\lambda) \sim \frac{b_b(\lambda)}{b_b(\lambda) + a(\lambda)} \qquad (3)$$

where $R_{rs}(\lambda)$ is remote sensing reflectance. While Eq. (3) is a simplification of radiative transfer, it helps to contextualize differences in $[L_W(\lambda)]_N$ observed between successive casts and across instrument types. Shape and magnitude similarities between HP2 $b_{bp}(470)$ and Chl profiles (Figs 5) strongly suggest Monterey Bay IOPs to be phytoplankton-driven. We therefore expect increases in phytoplankton biomass to be accompanied by increases in both $b_{bp}(\lambda)$ and $a(\lambda)$, resulting in decreases in above-water AOPs [48]. This relationship for example, can explain differences in $[\overline{L_W}(\lambda)]_N$ between HP2 and HE53 at CHR1. CHR1's proximity to M0 means that it possesses low biomass, as evidenced by its consistently low $b_{bp}(470)$ (< 0.01 $m^{-1}$), low Chl (< 4 mg $L^{-1}$), and high $\overline{\mathrm{OD}}_{490}$ (> 3.7 $m^{-1}$). Nevertheless, the existence of offsets between both $b_{bp}(470)$ and $R(490, z)$ measured by HP2 and IOP-P

indicates HP2's higher $[\overline{L_W}(\lambda)]_N$ is a result of lower phytoplankton biomass [Eq. (3)] [48]. Similarities in $[\overline{L_W}(\lambda)]_N$ as well as $R(490, z)$ profiles between HE53/IOP-P and C-OPS suggest they sampled similar watermass IOPs (Figs. 2-6b).

High overlap between HP2 and IOP-P $b_{bp}(470)$ profiles in the upper 3-5 m of CHR2 and OCE18 water columns (Fig. 5c & d) explains HP2's optical closure in the blue and red at both of these stations (Figs. 5c-d & 5c-d). Moreover, C-OPS's optical closure in the red and blue is on par with HP2; C-OPS exhibits better quantitative agreement (APD) with HE53 than with HP2 for the majority of $\lambda$'s for which they were compared. This suggests that C-OPS, HP2, and HE53 $[\overline{L_W}(\lambda)]_N$ products are derived from similar watermass IOPs, as further evidenced by the overlaps between C-OPS, HP2, and HE53 $R(490, z)$ profiles in the upper 3-5 m water columns at both stations. Although CHR2 and OCE18 $b_{bp}(470)$ and $R(490, z)$ profiles decouple below 3 and 5 m, this is unlikely to impact $[\overline{L_W}(\lambda)]_N$, since $\overline{\mathrm{OD}}_{490}$ , the layer of the water column in which $[L_W(\lambda)]_N$ is predominantly determined, is < 3 m at both stations [8, 49, 50].

The lower overall APD observed between C-OPS and HE53, compared to C-OPS vs. HP2 or HE53 vs. C-OPS, across CST17, OCE18, and CHR1 & 2, may be attributed to the high error associated with HP2-derived $[L_W(\lambda)]_N$, equivalent to HE53 $\sigma_{Lwn}(\lambda)$ (Fig. 4). HP2's low signal to noise ratio, coupled with its low vertical resolution, increases its susceptibility to environmental perturbations (e.g. shading, wave focusing, and platform perturbations) [51]. Although multi-cast mode lowers error (~10%), it still remains high compared to C-OPS and

HE53. Consequently, while HP2 and C-OPS $[L_W(\lambda)]_N$'s do overlap in Monterey Bay, HP2 $[L_W(\lambda)]_N$'s, and thus $[\overline{L_W}(\lambda)]_N$ are less representative of watermass IOPs than C-OPS (Fig. 4). We believe this phenomenon is aptly demonstrated by CST17. Here, as with CHR1, there is an offset between HP2 and IOP-P $b_{bp}(470)$ profiles and HP2 $[\overline{L_W}(\lambda)]_N$ is greater than HE53 $[\overline{L_W}(\lambda)]_N$, as would be expected for inversely related IOPs and above-water AOPs in phytoplankton-dominated ecosystems Eq. [3] [48]. However, examining individual HP2 casts indicate that $[\overline{L_W}(\lambda)]_N$ is not representative of the CST17 watermass; rather it is midway between two extremes (Figs. 2a & 8). These extremes are consistent with HP2 $R(490, z)$ profiles, which oscillate erratically in the upper water column (Fig. 6a). Judging by its consistent $b_{bp}(470)$ profiles, HP2's extreme $[L_W(\lambda)]_N$'s and very high $\sigma_{Lwn}(\lambda)$ are likely a reflection of low signal to noise than spatial variability or 'patchiness' of watermass IOPs. This problem is especially acute in the UV and NIR. Here many of our HP2 single casts are unusable due to extreme levels of noise. Consistent with D'Alimonte et al. [20], multi-cast significantly improves HP2 $[\overline{L_W}(\lambda)]_N$ at UV and NIR $\lambda$'s, underscoring the necessity for high vertical resolution in order to characterize these spectral regions (Figs. 2-3b&c). Because single and multi-cast were very similar (Fig. 4b&c), it is difficult to determine whether multi-cast improved $[\overline{L_W}(\lambda)]_N$ at visible $\lambda$'s.

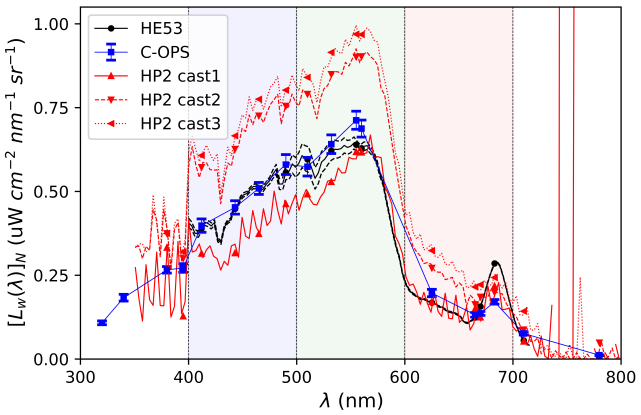



**Figure 8**. C-OPS and HE53 $[\overline{L_W}(\lambda)]_N$ with standard deviations compared against HP2 $[L_W(\lambda)]_N$ of individual casts for CST17.

CST18 illuminates the limitations of HP2 and IOP-P with regard to characterizing Monterey Bay watermasses. With $\overline{\text{Chl}}$ and $\overline{\text{OD}}_{490}$ of 52.8 mg $L^{-1}$ and 0.75 m, CST18 has the highest phytoplankton biomass of our five stations. Moreover, it exhibits high variability, or 'patchiness' in watermass AOPs, which is commonly associated with intense phytoplankton blooms [14, 24, 52]. This patchiness is nicely demonstrated by the detection of a subsurface phytoplankton aggregation by C-OPS cast 3, discrete Chl collected at depth, and HP2 cast 1 (e.g., $b_{bp}(470)$, Chl, and $R(490, z)$) (Figs. 5e & 6e). R/V John Martin typically drifts 20-30 m between successive casts. If an instrument change is required between casts however, it may drift > 100 m because of the added time required for instrument retrieval and re-deployment. Judging by the phytoplankton aggregation's initial detection in C-OPS cast 3 and eventual disappearance in HP2 cast 2, we believe that R/V John Martin drifted ~100-140 m inside of it (although not necessarily in a straight line). This may serve as a rough estimate as to the spatial scale over which IOPs fluctuate in high biomass regions of Monterey Bay.

Most importantly however, $\overline{\mathrm{OD}}_{490}$< 1 m at CST18. This is important because HP2 and IOP-P do not reliably sample the upper meter of the water column as deployed in this study, meaning that they cannot derive $[L_W(\lambda)]_N$ from the layer of the water column that predominantly impacts airborne and satellite-measured above-water AOPs [8, 49, 50]. C-OPS utility in sampling the upper 0.5 m of the water column means that at CST18, C-OPS $[L_W(\lambda)]_N$'s are extrapolated from a region of the water column that HP2 and HE53 did not reliably measure (e.g. Fig. 6e). Due to CST18's extreme patchiness coupled with vertical motility of dinoflagellates [14], the source of this bloom, IOPs in the upper meter of the water may fluctuate independently from the rest of the water column from cast to cast. Therefore, we might not be able to accurately extrapolate $[L_W(\lambda)]_N$ across the air-sea interface without directly measuring the upper 0.5 m of the water column. This would explain the increased APD between C-OPS and HE53 observed at CST18. It would also suggest that the improved APD of HP2 vs. HE53 at CST18 (relative to C-OPS vs. HE53) more likely resulted from similar extrapolation intervals (e.g., > 1 m) than inaccuracies involving C-OPS.

In closing we would like to acknowledge the limitations of our study. Prominent among these is that C-OPS, HP2, and IOP-P were deployed consecutively, not simultaneously. This is especially relevant in coastal marine ecosystems like Monterey Bay where watermass IOPs can vary over short spatial scales of several meters (e.g., Figs. 5 & 6). As a consequence of *R/V John Martin's* drifting with the current, watermass IOPs can fluctuate between casts (e.g., Fig. 5). However, to avoid casting shadows on each other and potentially becoming entangled, C-OPS, HP2, and IOP-P would likely need to be spaced tens of meters apart if deployed simultaneously. This is comparable to distances between profiler casts that are

sampled 2-3 minutes apart (as is the case in our study), as Monterey Bay current velocities are typically 10-20 cm $s^{-1}$ [53]. By serving as a proxy for watermass IOPs, $b_{bp}(470)$ profiles help to mitigate this shortcoming by providing context for $[L_W(\lambda)]_N$ comparisons. Because HP2 $b_{bp}(470)$ is ancillary and not used in processing above-water AOPs, comparing $b_{bp}(470)$, $R(490, z)$, and $[\overline{L_W}(\lambda)]_N$ between HP2 and IOP-P/HE53, offers insight into the impact of IOPs on $[\overline{L_W}(\lambda)]_N$. Although the unavailability of ancillary $b_{bp}(470)$ for C-OPS precludes a direct comparison, its cm scale vertical resolution is even more likely to be sensitive to IOP vertical structure. $R(490, z)$ profiles allow for indirect comparisons of watermass IOPs sampled by C-OPS, HP2, and IOP-P.

We were also unable to adequately address HE53's consistent underestimation of $[\overline{L_W}(\lambda)]_N$ in the green, as well as whether it was the result of HS6 underestimating green $b_{bp}(\lambda)$, ac-s overestimating $a(\lambda)$ in the green, a combination thereof, or a lack of sampling for IOPs in the upper meter of the water column. Tuchow et al. [7], which reported similar above-water AOP underestimations in Monterey Bay, speculated that HS6's reliance on Oishi's [54] proportionality argument and its $\lambda$-independent conversion factor may be problematic in phytoplankton-dominated watermasses, while the use of a standard (25 cm) pathlength ac-s in high biomass waters is less than optimal. Tuchow et al. () also suggest that Doxaran et al. [43] sigma-correction should eliminate differences $b_{bp}(\lambda)$ between HS6 and ECO-BB2F-SAT (attached to HP2) despite these instruments measuring VSF at different scattering angles, 140° and 117°, and the latter not requiring a sigma-correction due to its short optical pathlength. In light of this, we continue to assert the significance of our work in further

understanding the underlying mechanisms responsible for discrepancies in above-water AOPs between in-water optical profilers.

## 5. Conclusion

Our study's purpose was to compare two in-water optical profilers that sample AOPs at different depth and spectral resolutions within a dynamic coastal ecosystem. Our methodology is well suited for this purpose in that: 1) our methodology processes C-OPS and HP2 measurements using the same software, eliminating the likelihood of discrepancies in $[\overline{L_W}(\lambda)]_N$ being caused by different processing protocols; 2) it relies on modeled data to ascertain whether $[L_W(\lambda)]_N$'s from profiler casts meet optical closure; 3) it gauges impacts of vertical resolution and error propagation on $\sigma_{Lwn}(\lambda)$; and 4) it improves our understanding of the impact of watermass properties on profiler $[L_W(\lambda)]_N$ by comparing HP2 and IOP-P $b_{bp}(470)$ profiles. Our most far-reaching finding is that while fluctuations in watermass IOPs over short spatial scales can sometimes explain $[\overline{L_W}(\lambda)]_N$ differences between profilers, low HP2 signal to noise ratio, especially in highly attenuating waters, may also contribute [20]. This underscores the importance not only of rapid and/or coincident deployments to prevent aliasing between instrument types, but also of sampling Monterey Bay watermasses at adequate vertical resolution to mitigate the impacts of sensor drift and confounding environmental factors. Miniaturizing in-water optical profilers and IOP sensors would enable instruments to be simultaneously deployed without shading. It

would also enable these instrument suites to fully measure the upper meter of the water column, which is very important in high biomass watermasses (e.g., CST18).

More generally, we identified several takeaways regarding in-water optical profilers and their use in Monterey Bay. First, C-OPS ~1 cm vertical resolution and its ability to measure the upper 0.5 m of the water column are important for accurately characterizing above-water AOPs, especially in the UV and NIR (Figs. 2 & 3). Comparatively, HP2's low vertical resolution and signal to noise ratio result in substantial $[L_W(\lambda)]_N$ variability between casts that is unconnected to the actual watermass IOPs. Our findings demonstrate that by averaging $[\overline{L_W}(\lambda)]_N$ from multiple casts, investigators can arrive at a reasonable $[\overline{L_W}(\lambda)]_N$ in the visible. This however comes at the cost of high $\sigma_{Lwn}(\lambda)$., a high proportion of which could be connected to HP2's high noise signal rather than environmental variability. HP2's high noise signal may also diminish the accuracy of its $[\overline{L_W}(\lambda)]_N$. This is a plausible explanation as to why APD for C-OPS vs. HE53 was lower than APD for HP2 vs. C-OPS or HP2 vs. HE53 at four of our five stations. Furthermore, it is questionable as to whether HP2 and IOP-P/HE53 can characterize CST18 due to their inabilities to measure the upper 0.5 of the water column. We do point out however, that HP2 and IOP-P/HE53's high spectral resolution is also important. Both instrument types characterized spectral features that C-OPS misses, such as location of $[L_W(\lambda)]_N$ peaks. Given concurrent measurement of in-situ IOPs, HE53 can be used to model the spectral shape of above-water AOPs, which could in turn be constrained using C-OPS. This is perhaps ideal,

as it would allow for the best of both worlds: accurate and reliable characterization of spectral shape and magnitude of above-water AOPs, including in the UV and NIR. While largely ignored here, the increasing importance of UV and NIR to the ocean color community will require careful consideration of appropriate instrumentation for calibration/validation of planned next-generation satellites (e.g., PACE) that are expected to possess spectral ranges beyond the visible.

**Funding Information.** National Aeronautics and Space Administration (NASA) (NNH11ZDA001N, NNX14AI30A, NNX17AK89G).

**Acknowledgment**. We thank Dr. Stanford Hooker (NASA/Goddard Space Flight Center) and Mr. James Brown (University of Miami) for access and technical assistance with PROSIT. We also thank Mrs. Kendra N. Hayashi (University of California Santa Cruz) for her role in field sampling and Prof. Christopher Edwards for his assistance in data analysis.

## 6. References

1. C. O. Davis, N. Tufillaro, J. Nahorniak, B. Jones, and R. Arnone, "Evaluating VIIRS ocean color products for west coast and Hawaiian waters," in *Ocean Sensing and Monitoring V*(International Society for Optics and Photonics2013), p. 87240J.

2. M. E. Ondrusek, E. Stengel, M. A. Rella, W. Goode, S. Ladner, and M. Feinholz, "Validation of ocean color sensors using a profiling hyperspectral radiometer," in *SPIE Sensing Technology + Applications*(SPIE2014), p. 12.

3. R. Amin, D. Lewis, R. W. Gould, W. Hou, A. Lawson, M. Ondrusek, and R. Arnone, "Assessing the application of cloud–shadow atmospheric correction algorithm on HICO," IEEE Transactions on Geoscience and Remote Sensing **52**, 2646-2653 (2014).

4. S. Hooker, J. Morrow, and A. Matsuoka, "The 1% and 1 cm perspective in deriving and validating AOP data products," Biogeosciences Discussions **9** (2012).

5. S. Hooker, J. Morrow, and A. Matsuoka, "Apparent optical properties of the Canadian Beaufort Sea; Part 2: The 1% and 1 cm perspective in deriving and validating AOP data products," Biogeosciences **10**, 4511 (2013).

6. S. L. Palacios, R. M. Kudela, L. S. Guild, K. H. Negrey, J. Torres-Perez, and J. Broughton, "Remote sensing of phytoplankton functional types in the coastal ocean from the HyspIRI Preparatory Flight Campaign," Remote Sensing of Environment **167**, 269-280 (2015).

7. N. Tuchow, J. Broughton, and R. Kudela, "Sensitivity analysis of volume scattering phase functions," Optics express **24**, 18559-18570 (2016).

8. S. Hooker, and J. Brown, "Processing of Radiometric Observations of Seawater using Information Technologies (PROSIT): In-Water User Manual," NASA, ed. (2013).

9. C. D. Mobley, "Estimation of the remote-sensing reflectance from above-surface measurements," Applied Optics **38**, 7442-7455 (1999).

10. J. Sun, X. Xiong, A. Angal, H. Chen, A. Wu, and X. Geng, "Time-dependent response versus scan angle for MODIS reflective solar bands," IEEE Transactions on Geoscience and Remote Sensing **52**, 3159-3174 (2014).

11. M. Wang, and W. Shi, "Detection of ice and mixed ice–water pixels for MODIS ocean color data processing," IEEE Transactions on Geoscience and Remote Sensing **47**, 2510-2518 (2009).

12. J. T. Kirk, *Light and photosynthesis in aquatic ecosystems* (Cambridge university press, 1994).

13. M. M. Dekshenieks, P. L. Donaghay, J. M. Sullivan, J. E. Rines, T. R. Osborn, and M. S. Twardowski, "Temporal and spatial occurrence of thin phytoplankton layers in relation to physical processes," Marine Ecology Progress Series **223**, 61-71 (2001).

14. J. P. Ryan, M. A. McManus, and J. M. Sullivan, "Interacting physical, chemical and biological forcing of phytoplankton thin-layer variability in Monterey Bay, California," Continental Shelf Research **30**, 7-16 (2010).

15. J. H. Morrow, S. B. Hooker, C. R. Booth, G. Bernhard, R. N. Lind, and J. W. Brown, "Advances in measuring the apparent optical properties (AOPs) of optically complex waters," NASA Tech. Memo **215856**, 42-50 (2010).

16. C. O. Davis, M. Kavanaugh, R. Letelier, W. P. Bissett, and D. Kohler, "Spatial and spectral resolution considerations for imaging coastal waters," in *Coastal Ocean Remote Sensing*(International Society for Optics and Photonics2007), p. 66800P.

17. F. Mélin, and G. Zibordi, "Aerosol variability in the Po Valley analyzed from automated optical measurements," Geophysical Research Letters **32** (2005).

18. Biospherical Instruments Inc., "Compact Optical Profiling System: Hardware User's Manual (Doc 006406UA)," (2010).

19. Satlantic, "Operation Manual For: Profiler II Document Number: SAT-DN-00223," (2009).

20. D. D'Alimonte, G. Zibordi, and T. Kajiyama, "Effects of integration time on in-water radiometric profiles," Optics express **26**, 5908-5939 (2018).

21. R. M. Pope, and E. S. Fry, "Absorption spectrum (380–700 nm) of pure water. II. Integrating cavity measurements," Applied optics **36**, 8710-8723 (1997).

22. M. S. Twardowski, E. Boss, J. M. Sullivan, and P. L. Donaghay, "Modeling the spectral shape of absorption by chromophoric dissolved organic matter," Marine Chemistry **89**, 69-88 (2004).

23. L. Prieur, and S. Sathyendranath, "An optical classification of coastal and oceanic waters based on the specific spectral absorption curves of phytoplankton pigments, dissolved organic matter, and other particulate materials," Limnology and Oceanography **26**, 671-689 (1981).

24. J. P. Ryan, C. O. Davis, N. B. Tufillaro, R. M. Kudela, and B.-C. Gao, "Application of the hyperspectral imager for the coastal ocean to phytoplankton ecology studies in Monterey Bay, CA, USA," Remote Sensing **6**, 1007-1025 (2014).

25. S. Alvain, C. Moulin, Y. Dandonneau, and H. Loisel, "Seasonal distribution and succession of dominant phytoplankton groups in the global ocean: A satellite view," Global Biogeochemical Cycles **22** (2008).

26. S. A. Freeman, C. W. Proctor, and P. J. Werdell, "Obtaining Remote-Sensing Reflectance from Multiple Instrument Systems," (2014).

27. W. M. Graham, and J. L. Largier, "Upwelling shadows as nearshore retention sites: the example of northern Monterey Bay," Continental Shelf Research **17**, 509-532 (1997).

28. J. T. Pennington, and F. P. Chavez, "Seasonal fluctuations of temperature, salinity, nitrate, chlorophyll and primary production at station H3/M1 over 1989–1996 in Monterey Bay, California," Deep Sea Research Part II: Topical Studies in Oceanography **47**, 947-973 (2000).

29. J. Mueller, J. MuelIer, C. Pietras, S. Hooker, D. Clark, A. M. R. Frouin, and G. Fargion, "Ocean optics protocols for satellite ocean color sensor validation, revision 3, volumes 1 and 2," in *NASA tech. memo*(2002).

30. J. L. Mueller, and R. W. Austin, *Ocean optics protocols for SeaWiFS validation* (National Aeronautics and Space Administration, Goddard Space Flight Center, 1992).

31. W. Graham, J. Field, and D. Potts, "Persistent "upwelling shadows" and their influence on zooplankton distributions," Marine Biology **114**, 561-570 (1992).

32. L. K. Rosenfeld, F. B. Schwing, N. Garfield, and D. E. Tracy, "Bifurcated flow from an upwelling center: a cold water source for Monterey Bay," Continental Shelf Research **14**, 931-964 (1994).

33. Satlantic, "Prosoft 8.1 User Manual Doc: SAT-DN-00228," (2014).

34. H. R. Gordon, O. B. Brown, R. H. Evans, J. W. Brown, R. C. Smith, K. S. Baker, and D. K. Clark, "A semianalytic radiance model of ocean color," Journal of Geophysical Research: Atmospheres **93**, 10909-10924 (1988).

35. WET Labs Inc., "Spectral Absorption and Attenuation Meter User's Guide," (2008).

36. H.-O. B. I. Laboratories, "HydroScat-6P Spectral Backscattering Sensor & Fluorometer (Revision J)," (2010).

37. R. M. Kudela, W. P. Cochlan, T. D. Peterson, and C. G. Trick, "Impacts on phytoplankton biomass and productivity in the Pacific Northwest during the warm ocean conditions of 2005," Geophysical Research Letters **33** (2006).

38. N. A. Welschmeyer, "Fluorometric analysis of chlorophyll a in the presence of chlorophyll b and pheopigments," Limnology and Oceanography **39**, 1985-1992 (1994).

39. E. Arar, "Method 446.0 In Vitro Determination of Chlorophylls a, b, c1+ c2 and//Visible Spectrophotometry. Revision 1.2 National Exposure Research Laboratory," (US Environmental Protection Agency Cincinatti, OH, 1997).

40. J. M. Sullivan, M. S. Twardowski, J. R. V. Zaneveld, C. M. Moore, A. H. Barnard, P. L. Donaghay, and B. Rhoades, "Hyperspectral temperature and salt dependencies of absorption by water and heavy water in the 400-750 nm spectral range," Applied Optics **45**, 5294-5309 (2006).

41. R. Röttgers, D. McKee, and S. B. Woźniak, "Evaluation of scatter corrections for ac-9 absorption measurements in coastal waters," Methods in Oceanography **7**, 21-39 (2013).

42. Morel, "Optical Aspects of Oceanography," in *Optical Aspects of Oceanography*, M. G. Jerlov, and E. S. Nielsen, eds. (Academic Press Inc, 1977).

43. D. Doxaran, E. Leymarie, B. Nechad, A. Dogliotti, K. Ruddick, P. Gernez, and E. Knaeps, "Improved correction methods for field measurements of particulate light backscattering in turbid waters," Optics express **24**, 3615-3637 (2016).

44. B. Efron, "Bootstrap methods: another look at the jackknife," Annals of Statistics, 1-26 (1979).

45. D. C. Pierson, S. Kratzer, N. Strömbeck, and B. Håkansson, "Relationship between the attenuation of downwelling irradiance at 490 nm with the attenuation of PAR (400 nm–700 nm) in the Baltic Sea," Remote Sensing of Environment **112**, 668-680 (2008).

46. W. Scott-Pegau, H. Maske, R. Lara-Lara, S. Alvarez-Borrego, R. Cervantes-Duarte, and E. Valdez-Holguín, "The determination of PAR levels from absorption coefficient profiles at 490 nm," Ciencias Marinas **25**, 487-507 (1999).

47. E. Spyrakos, R. O'Donnell, P. D. Hunter, C. Miller, M. Scott, S. G. Simis, C. Neil, C. C. Barbosa, C. E. Binding, and S. Bradt, "Optical types of inland and coastal waters," Limnology and Oceanography **63**, 846-870 (2018).

48. Y. Xiong, X. Zhang, S. He, and D. J. Gray, "Re-examining the effect of particle phase functions on the remote-sensing reflectance," Applied optics **56**, 6881-6888 (2017).

49. H. R. Gordon, and W. McCluney, "Estimation of the depth of sunlight penetration in the sea for remote sensing," Applied optics **14**, 413-416 (1975).

50. D. R. Mishra, S. Narumalani, D. Rundquist, and M. Lawson, "Characterizing the vertical diffuse attenuation coefficient for downwelling irradiance in coastal waters: Implications for water penetration by high resolution satellite data," ISPRS Journal of photogrammetry and remote sensing **60**, 48-64 (2005).

51. G. Zibordi, S. Hooker, J. Berthon, and D. D'Alimonte, "Autonomous above-water radiance measurements from an offshore platform: a field assessment experiment," Journal of Atmospheric and Oceanic Technology **19**, 808-819 (2002).

52. J. Ryan, M. McManus, R. Kudela, M. L. Artigas, J. Bellingham, F. Chavez, G. Doucette, D. Foley, M. Godin, and J. Harvey, "Boundary influences on HAB phytoplankton ecology in a stratification-enhanced upwelling shadow," Deep Sea Research Part II: Topical Studies in Oceanography **101**, 63-79 (2014).

53. CeNCOOS, "HF Radar Hourly Surface Currents (6km)," https://data.cencoos.org/.

54. T. Oishi, "Significant relationship between the backward scattering coefficient of sea water and the scatterance at 120," Applied Optics **29**, 4658-4665 (1990).

# Chapter 2: Structurally evaluating end-member approach, an empirical ocean color method for estimating CDOM absorption at 440 nm

Jesse Bausell, Dr. Christopher A. Edwards, & Dr. Raphael M. Kudela

## Abstract

End-member approach (EMA) is an empirical method that can be applied to remotely sensed ocean color data to estimate absorption of colored dissolved organic material at 440 nm ($a_{CDOM}(440)$). It relies on an empirical relationship between $a_{CDOM}(440)$ and spectral end-member ratios of diffuse attenuation coefficient ($k_d(\lambda)$), occupying the ultraviolet (UV)-blue ($k_d(\lambda_1)$) and red-near infrared (NIR) ($k_d(\lambda_2)$) regions of the spectrum. In the field, EMA has been shown to estimate $a_{CDOM}(440)$ across a diverse array of aquatic ecosystems using several different $k_d(\lambda_1)/k_d(\lambda_2)$ ratios. Here we evaluated EMA's underlying structure and its potential robustness across a variety of conditions by testing it on a series (n = 1000) of modeled aquatic ecosystems. The optical properties of these modeled ecosystems were assumed to follow lognormal distributions. Means and standard deviations ($\sigma$) of these distributions were determined from measurements sampled by the NASA bio-optical Marine Algorithm Dataset (NOMAD). Their optical properties were modeled with the radiative transfer software package Hydrolight 5.3, using nine different Fournier-Forand phase functions. Employing least-squares regression, we then assessed EMA's ability to estimate $a_{CDOM}(440)$ with two different $k_d(\lambda_1)/k_d(\lambda_2)$ ratios: $k_d(320)/\ k_d(780)$ ($\tilde{k}_{d1}$) and $k_d(412)/\ k_d(667)$ ($\tilde{k}_{d2}$). Similar to previous findings,

we report linear and parabolic relationships between $\tilde{k}_{d1}$vs. $a_{CDOM}(440)$ and $\tilde{k}_{d2}$ vs. $a_{CDOM}(440)$, respectively, with both ratios accounting for high proportions of $a_{CDOM}(440)$ variance ($R^2 > 0.95$). However, $\tilde{k}_{d2}$ is more sensitive to phase function ($>$ 14% coefficient uncertainty), and thus optical properties of suspended particle assemblages than is $\tilde{k}_{d1}$ (< 4.5% coefficient uncertainty). $\tilde{k}_{d2}$'s increased sensitivity suggests that while EMA does have potential to be applied to airborne and satellite sensors, it would be the most reliable with sensors that measure in the ultraviolet (UV) and near-infrared (NIR). Our findings indicate that EMA's accuracy declines with increasing concentrations of bio-optical constituents, and as such EMA works best in open ocean and low-biomass coastal ecosystems, as corroborated by K-means cluster analysis. EMA's overall ability to accurately estimate $a_{CDOM}(440)$ in modeled ecosystems indicates whether or not it is based on radiative transfer theory.

## 1. Introduction

The measurement of ocean color with *in situ*, above-water, airborne, and space-based optical sensors is used to characterize optically active biogeochemical, or bio-optical constituents within aquatic ecosystems. Its potential for characterizing these ecosystems spatially makes ocean color an increasingly important component of limnology and oceanography [1, 2]. Because they have no contact with the aquatic ecosystems that they measure, satellite and airborne sensors rely on optical algorithms to estimate biogeochemical properties from optical measurements. These algorithms are assumed to obey radiative transfer theory [3], namely that biological and chemical

constituents selectively absorb and scatter light at different wavelengths ($\lambda$) and that these inherent optical properties (IOPs) impact the light fields, or apparent optical properties (AOPs) of aquatic ecosystems [4-8]. The advent of next-generation satellites with spectral capabilities that extend into the UV and NIR promises to expand the breadth of habitats where bio-optical properties can be measured to include coastal, estuarine, lacustrine, and riverine ecosystems. However, these next-generation sensors will require the development of novel bio-optical algorithms that are compatible with them [1, 9, 10]. In addition to next-generation sensors, these novel algorithms would ideally be applicable to $\lambda$'s measured by legacy and present-day optical sensors as well.

End-member approach (EMA) is a novel method proposed by Hooker et al. [4] for empirically estimating absorption of colored dissolved organic material (CDOM) at 440 nm ($a_{CDOM}(440)$), by relying on diffuse attenuation coefficient ($k_d(\lambda)$) spectral end-member ratios. It exhibits promise as a foundation for global $a_{CDOM}(440)$ algorithms, as it was initially shown to estimate $a_{CDOM}(440)$ across a variety of chemically and optically distinct aquatic ecosystems ($R^2 \geq 0.94$) [4, 11]. Contrary to previous $a_{CDOM}(440)$ algorithms (e.g., [12-14]), EMA is not confined to specific salinity, turbidity, or geographical ranges. It also doesn't require $k_d(\lambda)$ end-members at specific $\lambda$'s, only that these end-members be located within UV-blue ($k_d(\lambda_1)$) and red-NIR ($k_d(\lambda_2)$) spectral regions. $k_d(\lambda_1)$ and $k_d(\lambda_2)$ represent spectral regions where absorption and scattering properties respectively predominate. Because field

data indicates that EMA can estimate $a_{CDOM}(440)$ with a variety of $k_d(\lambda_1)/k_d(\lambda_2)$ ratios, it also has the potential to be applied to a multitude of optical sensors. Field evaluations on extended collection of aquatic ecosystems, for example, have demonstrated EMAs ability to estimate $a_{CDOM}(440)$ using $k_d(320)/\ k_d(780)$ ($\tilde{k}_{d1}$) and $k_d(412)/\ k_d(670)$ ($\tilde{k}_{d2}$) [15]. These two ratios, $\tilde{k}_{d1}$ and $\tilde{k}_{d2}$ are respectively comparable to proposed next-generation satellites, which will possess channels centered in the UV and NIR, and Moderate Resolution Imaging Spectroradiometer (MODIS), a present-day ocean monitoring satellite.

Improving estimations of $a_{CDOM}(440)$ would be an important contribution to interpreting ocean color. $a_{CDOM}(440)$ is a direct indicator of concentrations of CDOM and dissolved organic carbon more generally [13, 16]. $a_{CDOM}(440)$'s relationship to phytoplankton abundance and primary productivity is significant but more complex, fluctuating both seasonally and geographically [17]. This increase in complexity is because while phytoplankton components contribute to CDOM [18], CDOM can also absorb a significant portion of photosynthetically active radiation, precluding its utilization by phytoplankton [19]. $a_{CDOM}(440)$ is also locally correlated with salinity, heavy metals, and freshwater algal toxins [20-22]. By evaluating EMA using a theoretical (modeling) perspective, our work helps to facilitate its development and eventual extension to airborne and satellite sensors. This extension of EMA to airborne and satellite sensors would pave the way for, as an example, improved estimations of primary productivity as well as the delineation,

classification, and tracking of watermasses as they move through aquatic habitats [22, 23].

EMA's success estimating $a_{CDOM}(440)$ in the field and its ability to do so at different $k_d(\lambda_1)/k_d(\lambda_2)$ ratios alludes to its global potential. Notwithstanding, its empirical nature obfuscates the underlying mechanisms responsible for its success, as well as confounding factors that could introduce error. Hooker et al. [4, 11, 15] report strong correlations between $k_d(\lambda_1)/k_d(\lambda_2)$ ratios, indicating that $k_d(\lambda_1)$) is more responsive to CDOM increases than $k_d(\lambda_2)$. While both end-members increase with $a_{CDOM}(440)$, $k_d(\lambda_1)$ increases are an order of magnitude larger than $k_d(\lambda_2)$. This disparity between $k_d(\lambda_1)$ and $k_d(\lambda_2)$ is intuitive from a theoretical radiative transfer standpoint. $k_d(\lambda)$ is a function of total absorption ($a(\lambda)$) and scattering ($b(\lambda)$) and while phytoplankton and non-algal particles absorb and scatter at $k_d(\lambda_1)$ and $k_d(\lambda_2)$ [6, 24, 25], $a_{CDOM}(\lambda)$ is characterized by exponential decay and is negligible at $k_d(\lambda_2)$ [8]. Moreover, being comprised of particles < 0.2 $\mu$m in diameter, CDOM scattering is also assumed to be negligible [8, 26]. CDOM's negligible scattering means that on a theoretical basis, CDOM should only impact $k_d(\lambda_1)$, not $k_d(\lambda_2)$. Increases in $k_d(\lambda_2)$ in response to $a_{CDOM}(440)$ are likely to be the result of the correlations between CDOM, phytoplankton, and sediments observed broadly across aquatic ecosystems [10]. However, because phytoplankton and sediments also contribute to $k_d(\lambda_1)$, it is difficult to determine whether EMA's utility in estimating $a_{CDOM}(440)$ stems from a CDOM-dominated $k_d(\lambda_1)/k_d(\lambda_2)$ signal, correlations

between bio-optical constituents, or a combination of the two. Both explanations could account for why EMA, contrary to Siegel et al. [14], can estimate $a_{CDOM}(440)$ in turbid environments. Alternatively, it is possible that EMA does not obey radiative transfer theory.

Structurally evaluating EMA, in order to determine its robustness and the underlying mechanisms responsible for its initial success, will require an improved understanding of which types of ecosystems EMA is likely and unlikely to estimate $a_{CDOM}(440)$. It will also require knowledge of the IOPs associated with these ecosystems. The availability of high-quality field measurements of in-situ $k_d(\lambda)$ and $a_{CDOM}(440)$ (e.g., [4, 11, 15]) has enabled the establishment of reliable empirical relationships between $a_{CDOM}(440)$ using several different $k_d(\lambda_1)/k_d(\lambda_2)$ ratios. To establish these empirical relationships, Hooker et al.'s [15] only included field stations, or "watermasses" (referred to henceforth as watermasses) that they hypothesized as being "conservative", or possessing sufficient inflows and outflows to constrain bio-optical constituents. Hooker et al. [15] also sampled and evaluated EMA in "non-conservative" watermasses, watermasses which they hypothesized to exhibit extreme bio-optical properties caused by exposure to "stressors". However, these non-conservative watermasses were excluded in Hooker et al.'s [15] establishment of empirical relationships between $\tilde{k}_{d1}$ vs. $a_{CDOM}(440)$ and $\tilde{k}_{d2}$ vs. $a_{CDOM}(440)$. Rather, Hooker et al. [15] subdivided these watermasses into 15 categories based on the stressor(s) to which they are exposed (e.g., restricted

inflow/outflow, heightened primary productivity, increased sediment loading and re-suspension, proximity to glaciers, and various anthropogenic forcings, etc.) and compared them to the aforementioned $\tilde{k}_{d1}$ vs. $a_{CDOM}(440)$ empirical relationship that was established using conservative watermasses.

Classifying ecosystems in which EMA is field-tested is an important first step in evaluating the method's strengths and limitations. Nonetheless, the dearth of IOPs and bio-optical measurements available for these watermasses limits our ability to understand how EMA works. Identifying and classifying "non-conservative" watermasses according to their exposure to potential "stressors" necessitates a degree of arbitrariness in the absence of bio-optical constituent and IOP data. It remains unclear how or even if the Hooker et al. [15]-identified stressors impact IOPs and AOPs of watermasses. Moreover, *it is impossible to sample everywhere*, and the inherent monetary, logistical, and time constraints associated with field sampling limit our ability to comprehensively evaluate EMA. Here, we structurally evaluate EMA by circumventing the limitations associated with field sampling. We examine the relationships between $a_{CDOM}(440)$ and $k_d(\lambda_1)/k_d(\lambda_2)$ using a series of computer-modeled watermasses, or "ecosystems" (referred to henceforth as ecosystems). These ecosystems were created using Hydrolight 5.3 (HE53), a software package that uses radiative transfer theory to calculate AOPs based on user-supplied inputs. We designed this ecosystem series to represent, as realistically as possible, the diversity of ecosystem optical properties likely to be characterized by EMA. We

utilized these ecosystems to determine whether or not EMA obeys radiative transfer theory, its sensitivity to phase function, and where it is likely to estimate $a_{CDOM}(440)$ effectively.

## 2. Methods

Evaluating EMA structurally requires several steps. First, to ensure that our series of ecosystems reflects nature to the fullest extent possible, realistic ranges and relationships between bio-optical constituents (e.g., phytoplankton, CDOM, and sediments) or IOPs must be established. Second, it is important to model ecosystem optical properties using different scattering phase functions to examine how changes in suspended particle assemblages could impact EMA's utility. Third, establishing empirical relationships for $a_{CDOM}(440)$ at two different end-member ratios, $k_d(320)/k_d(780)$ ($\tilde{k}_{d1}$) and $k_d(412)/k_d(667)$ ($\tilde{k}_{d2}$), can provide insight into whether EMA relies on the same underlying mechanisms at different $\lambda$'s. It can also provide insight into the feasibilities of applying EMA to next-generation, as well as present day satellites, such as MODIS. Finally, classifying ecosystems by 'type' and evaluating abilities of $\tilde{k}_{d1}$ and $\tilde{k}_{d2}$ to estimate $a_{CDOM}(440)$ within these ecosystem types can provide insight into *where* next-generation satellites and MODIS are likely to reliably estimate $a_{CDOM}(440)$ using EMA.

*2.1 Bio-optical constituent distributions*

To maximize the likelihood that ecosystems were characterized by a comprehensive, but also a realistic suite of optical properties, we assumed the ubiquity of three bio-optical constituent types: phytoplankton, suspended sediments, and CDOM. To estimate their ranges and their relationships to one another, we utilized NASA bio-Optical Marine Algorithm Dataset (NOMAD). NOMAD is a publically available repository of in-situ bio-optical data, collected specifically for purposes of ocean color algorithm development and validation. It comprises 4,459 field stations worldwide, sampled between 1991 – 2008 [10]. NOMAD data were sampled and quality controlled in a manner consistent with NASA Ocean Optics Protocols and can therefore be considered reliable [27, 28]. Of the 4,459 available NOMAD stations, 538 contain surface measurements for chlorophyll concentration (Chl) ($\mu g\ L^{-1}$), in-situ remote sensing reflectance at 670 nm ($R_{rs}(670)$) ($sr^{-1}$), and $a_{CDOM}(443)$ ($m^{-1}$), which we use as proxies for phytoplankton, suspended sediments, and CDOM. While this subset of stations is limited to the Atlantic Ocean Basin, it comprises a geographically diverse assemblage of habitats. These habitats include the Gulf of Maine, Delaware Bay, Scotia Sea, Equatorial Current, Brazil Current, Falkland Current, Canary Current, outer Amazon River Plume, Chesapeake Bay, Delaware Bay, Gulf of Mexico, as well as the open ocean (Fig. 1).

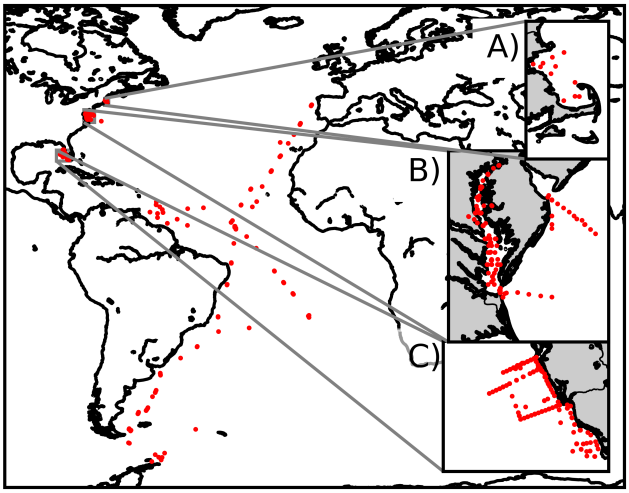



**Figure 1.** Map of the subset of NOMAD sampling stations (n=538) used to determine global distributions of Chl, $a_g(443)$, and $R_{rs}(670)$, including close-ups of southern Gulf of Maine (a), Chesepeake and Delaware Bays (b), and the west coast of Florida (c).

While our NOMAD station subset (referred to henceforth as "NOMAD") affords a unique opportunity to access high-quality bio-optical constituent data from a geographically diverse assemblage of sampling stations, these in-situ data were collected exclusively from the coasts, open ocean, and navigable estuaries (e.g., Chesapeake Bay) (Fig. 1). Their bio-optical constituent ranges are thus constrained, and do not encompass the full range of values, such as those values exhibited by inland aquatic habitats or intense phytoplankton blooms, watermasses likely to be categorized as non-conservative [15]. Structurally evaluating EMA therefore requires a dataset that not only represents realistic relationships between bio-optical constituents (e.g., NOMAD), but also comprehensive ranges of bio-optical constituents that account for the more extreme habitats. We used NOMAD as a

template off of which to simulate such a dataset. We first assumed that “global" distributions of bio-optical constituents are lognormal, as aquatic ecosystems are predominantly oceanic and thus exhibit low concentrations of phytoplankton, CDOM, and sediment. As bio-optical constituents increase, we also assumed that the cumulative surface area (e.g., number of ecosystems) that they characterize decreases. Additionally, we postulated that despite their constrained bio-optical constituent ranges, means and standard deviations ($\sigma$) of log-transformed NOMAD data characterize global distributions of Chl, $R_{rs}(670)$, and $a_{CDOM}(443)$. As such, we theorized that correlations between NOMAD-measured constituents are robust and therefore apply to ecosystems outside of the NOMAD ranges. We also assumed that all ecosystems, including those with the most extreme bio-optical constituent values, fall within mean $\pm\,\sigma$ of log-transformed NOMAD data.

To characterize bio-optical constituent distributions, we computed means and $\sigma$’s of (natural) log-transformed values measured by NOMAD (Chl, $R_{rs}(670)$, and $a_{CDOM}(443)$) (Figs. 2a, 2c, & 2e). Employing simple linear regression, we then built a Pearson’s r correlation matrix for our three log-transformed constituents, after testing for (Watson-Durbin) and when necessary correcting for (Cochrane Orcutt) residual autocorrelation (see Fig. 3). We designed our ecosystem series (n = 1000) based on means, $\sigma$’s, and correlations of bio-optical constituents collected from NOMAD (Figs. 2 & 3). First, we created three fixed arrays, one for each bio-optical constituent, of 1000 consecutively ordered and evenly spaced (0.001) probabilities

ranging from 0.0005 to 0.9995. We utilized Latin hypercube sampling [29] to semi-randomly assign three probabilities, one per bio-optical constituent array, to each ecosystem. Using constituent-specific cumulative density functions that were constructed with means and $\sigma$ 's calculated from NOMAD (Figs. 2 & 3), we computed log-transformed Chl, $R_{rs}(670)$, and $a_{CDOM}(443)$ values for each ecosystem based on assigned probabilities. We then employed Cholesky decomposition to create dependence between log-transformed Chl, $R_{rs}(670)$, and $a_{CDOM}(443)$ values using the aforementioned Pearson's r correlation matrix. Lastly, we calculated inverses of log-transformed values. Because NOMAD does not directly measure turbidity, we calculated total suspended matter (TSM) from $R_{rs}(670)$ using the Nechad turbidity algorithm [30]. Nechad-calculated TSM was unrealistic for ecosystem #331, the ecosystem that was assigned the highest $R_{rs}(670)$. As such, we assigned it a TSM of 1000 $g\ m^{-3}$, which is characteristic of an extremely turbid ecosystem [31, 32].

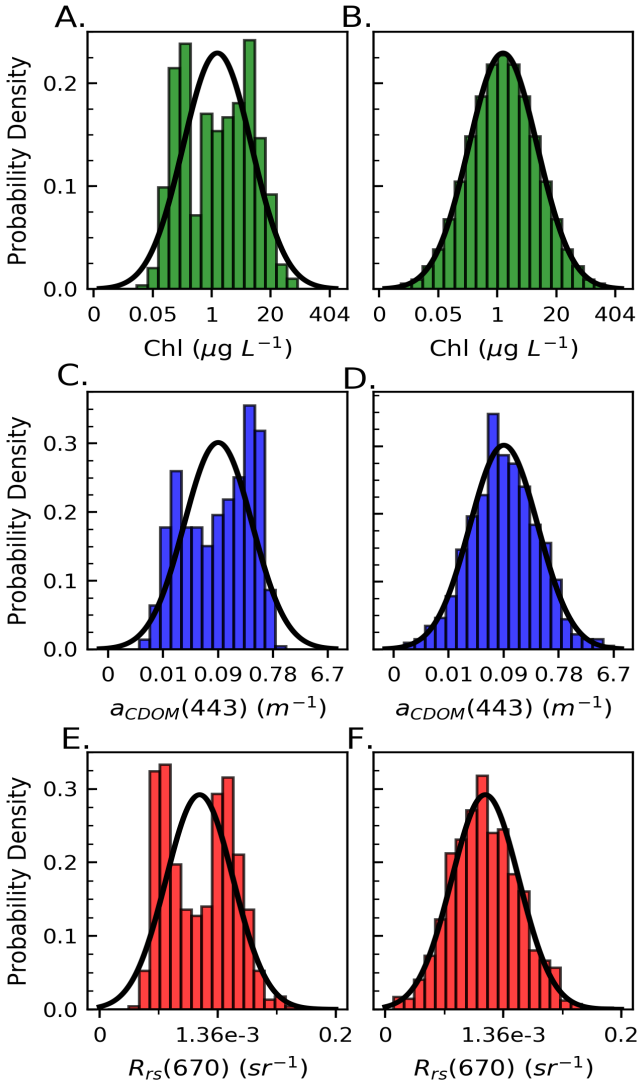



**Figure 2.** Probability density functions for Chl, $a_{CDOM}(443)$, and $R_{rs}(670)$ for NOMAD stations (left) and simulated ecosystems (right), overlaid with Gaussian curves calculated using means and $\sigma$'s computed from NOMAD stations.

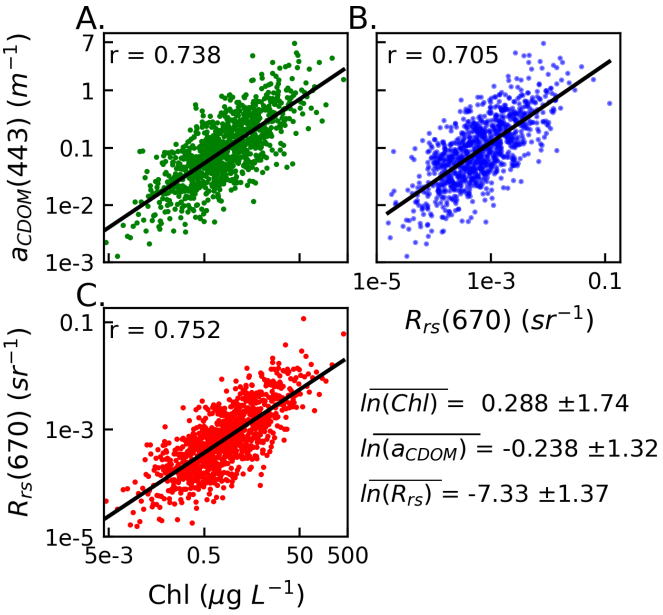



**Figure 3.** Scatterplot comparisons of log-transformed bio-optical ecosystem constituents plotted with logarithmic axes. $a_{CDOM}(443)$ vs. Chl (a), $R_{rs}(670)$ vs. Chl (b), and $R_{rs}(670)$ vs. $a_{CDOM}(443)$ (c) are overlaid with least squares best-fit lines and correlation coefficients. Mean $\pm\ \sigma$ of log-transformed constituents are displayed on the bottom right quadrant.

The series of 1000 ecosystems produced by our methodology satisfied three conditions that we deemed important for evaluating EMA: 1) means and $\sigma$'s of log-transformed bio-optical constituents assigned to our 1000 ecosystem series are equal to those of NOMAD measurements (Fig. 2); 2) bio-optical constituents reflected the same dependences (Pearson's r's) as NOMAD (Fig. 3); and 3) ecosystems expand upon the ranges of bio-optical constituents measured by NOMAD (Fig. 2). While NOMAD stations exhibit maximum Chl, $a_{CDOM}(443)$, and TSM of 77.9 $\mu g\ L^{-1}$, 1.52 $m^{-1}$, and 62.75 $g\ m^{-3}$, our ecosystem series extends these maxima to 408.9 $\mu g\ L^{-1}$, 6.7 $m^{-1}$, and 1000 $g\ m^{-3}$, respectively. By adhering to the conditions stated above,

we ensure that the optical properties that our ecosystems exhibit are diverse, comprehensive, and also realistic. Preserving dependences between bio-optical constituents can also help determine whether EMA's reported field success could be based on existing correlations between phytoplankton, CDOM, and sediments across watermasses. Additionally, by increasing the number of ecosystems from 538 to 1000 while ensuring against duplicates, Latin hypercube sampling enables us to significantly expand the number bio-optical properties under which we can evaluate EMA.

*2.2 Ecosystem Modeling: Hydrolight 5.3*

We modeled ecosystem optical properties specifying HE53's "case 2 IOPs" model, which relies on user-input Chl, TSM, and $a_{CDOM}(440)$ to model optical properties. It also uses Fournier-Forand phase function, which assumes suspended particles to be Mie-scattering, spherical, non-absorbing, Junge size-distributed [33]. The Fournier-Forand phase function requires two $\lambda$-independent fractions of particulate backscattering ($b_{bp}(\lambda)$) over $b(\lambda)$ to characterize it, one for phytoplankton ($\tilde{b}_{ph}$) and one for minerals ($\tilde{b}_{min}$). Table 1 describes HE53 settings in detail.

**Table 1. HE53 settings as specified using "case 2 IOPs".**

| Parameter | Setting | Input Source | Notes |
|---|---|---|---|
| IOP Component 1: Pure water | Pope & Fry 1997 | --- | --- |
| IOP Component 2: Phytoplankton | $a_{ph}(\lambda) = a^*_{ph}(\lambda)Chl^{0.65}$<br>$b_{ph}(\lambda) = 0.407Chl^{0.795}\left(\frac{660}{\lambda}\right) - a_{ph}(\lambda)$<br>Phase function: Fournier-Forand w/$\tilde{b}_{ph}$ | User-supplied Chl & $\tilde{b}_{ph}$ | $a^*_{ph}(\lambda)$ are normalized, $\lambda$-dependent coefficients ($m^2\ g^{-1}$) |
| IOP Component 3: CDOM | $a_g(\lambda) = a_g(440)e^{\gamma(\lambda-440)}$ | User-supplied $a_g(440)$ | $\gamma$ = - 0.015 $m$ |
| IOP Component 4: Minerals | $\Psi_{min}(\lambda) = \Psi^*_{min}(\lambda)TSM$<br>Phase function: Fournier-Forand w/$\tilde{b}_{min}$ | User-supplied TSM & $\tilde{b}_{min}$ | $\Psi^*_{min}(\lambda)$ are normalized $\lambda$-dependent $a$ or $b$ coefficients ($m^2\ g^{-1}$) |
| Inelastic Scatter | Chl Fluorescence (No Raman Scatter) | --- | --- |
| $T$ & $S$ | $\lambda$-independent index of refraction ($n$) | $n$ = 1.34 | --- |
| Sky Model #1 | RADTRAN-X subroutine | --- | Partitions into direct & diffuse irradiances |
| Sky Model#2 | HCNRAD subroutine | Solar zenith = $0^o$<br>Latitude = $0^o$ | Computes sky radiance from solar angle & irradiances[2] |
| ATM[1] | Air Pressure, humidity, & wind speed | --- | Default Values |
| Output $\lambda$ | $\lambda$ = 320, 412, 443, 667, & 780 nm | --- | --- |
| Output Depth | Range: 0-2 m<br>Resolution: 0.5 m | --- | --- |
| Bottom Boundary | Infinite | --- | --- |

[1.] Atmospheric/Meteorological Parameters
[2.] Solar irradiances represent yearly equatorial average
* All inputs are constant with depth

To better understand the impact of particle characteristics on EMA, we used three different $\tilde{b}_{ph}$ and $\tilde{b}_{min}$ values each (low, intermediate, and high) to characterize our phase functions. $\tilde{b}_{ph}$ and $\tilde{b}_{min}$ are impacted by size frequency distribution, shape, as

well as chemical composition of their respective particles [34-36]. For our low value, we used the quantity 0.005 for both $\tilde{b}_{ph}$ and $\tilde{b}_{min}$. Representative of the lower range of what is considered "typical" for oceanic waters, 0.005 is intended to characterize pico size-dominated phytoplankton communities and similarly sized mineral particles with low reflectance [37-39]. For nano and meso size-dominated phytoplankton communities and more typical inorganic mineral assemblages, which exhibit higher $b_{bp}(\lambda)$ than most phytoplankton, we selected $\tilde{b}_{ph}$= 0.1 and $\tilde{b}_{min}$ = 0.2 as intermediate values [37, 38]. Finally, our high values, $\tilde{b}_{ph}$= 0.3 and $\tilde{b}_{min}$ = 0.6 represent large centric diatoms and highly reflective minerals [34, 39]. We ran HE53 for each ecosystem using all possible combinations of $\tilde{b}_{ph}$ and $\tilde{b}_{min}$, nine phase functions in total. The completed modeled data set consisted of nine HE53 runs per ecosystem (9000 in total).

*2.3 Evaluating and Analyzing EMA*

Linear least-squares regression was employed to determine EMA's utility across ecosystems by examining the relationship between $\tilde{k}_{d1}$ and $a_{CDOM}(440)$ for each phase function individually. This process entailed determining a goodness of fit line via least-squares regression, calculating absolute residuals ($res$) for each ecosystem (Eq. 1), and then computing root mean squared error ($\sigma_{res}$). Upon excluding the outliers, identified as ecosystems for which $res > 5\sigma_{res}$, we re-applied least-squares regression and calculated the coefficient of determination ($R^2$). $\tilde{k}_{d2}$ followed similar

process as $\tilde{k}_{d1}$, except that it used parabolic, rather than linear, least-squares regression.

$$res = |a_{CDOM}(440) - \hat{a}_{CDOM}(440)| \quad (1)$$

Equation 1: Absolute residual ($res$) for a given ecosystem, calculated as the absolute difference between measured ($a_{CDOM}(440)$) and least-squares predicted ($\hat{a}_{CDOM}(440)$) CDOM absorption at 440 nm.

Bootstrapping with replacement was employed to determine average relationships between $\tilde{k}_{d1}$ and $\tilde{k}_{d2}$ vs. $a_{CDOM}(440)$ as predicted via least-squares regression ($\hat{a}_{CDOM}(440)$), as well as to quantify uncertainties in these relationships associated with phase function. For a given bootstrap resample, each ecosystem was randomly assigned one of its nine values for $\tilde{k}_{d1}$, modeled using different Fournier-Forand phase functions. As before, we determined goodness of fit, excluded outliers, and re-calculated the goodness of fit line ($\tilde{k}_{d1}$ vs. $\hat{a}_{CDOM}(440)$) once $\tilde{k}_{d1}$ was randomly selected for all ecosystems. Upon completing 1000 total bootstrap-resamples, we calculated means and $\sigma$'s for bootstrapped least-squares coefficients and overlaid this new mean best-fit line on top of mean $\tilde{k}_{d1}$ vs. $a_{CDOM}(440)$, as averaged from the resamples. $\tilde{k}_{d1}$ was considered to have successfully estimated $a_{CDOM}(440)$ for a given ecosystem when $res \leq \sigma_{res}$. Aside from substituting polynomial for a linear least-squares regression, $\tilde{k}_{d2}$ relied on the same process as $\tilde{k}_{d1}$. We reported $\sigma$'s of mean least-squares coefficients as both values and as percentages of their respective signals.

To assess how different ecosystem types might impact EMA's utility, we performed a cluster analysis, presetting the number of clusters to 12 based on the elbow method. To group them according to their underlying characteristics, clustered ecosystems were based on the IOPs modeled off of bio-optical constituents, or "IOP components", at $\lambda$ = 443 nm: $a_{CDOM}(443)$, $a_{ph}(443)$, $a_{min}(443)$, $b_{ph}(443)$, and $b_{min}(443)$. All three constituents absorb and scatter significantly at $\lambda$ = 443 nm, making it ideal for comparing their relative impacts on ecosystem light fields (Fig. 4). Moreover, unlike Chl, TSM, and $a_{CDOM}(443)$, IOP components are quantified by the same units of measurement ($m^{-1}$), which allow for direct comparisons between them. After running k-means, we compared the proportion of ecosystems within each cluster for which $\tilde{k}_{d1}$ and $\tilde{k}_{d2}$ had successfully estimated $a_{CDOM}(440)$; we also examined which clusters contained the outliers.

Lastly, we categorized modeled ecosystems as conservative and non-conservative in order to compare our findings with Hooker et al. [15]. Conservative ecosystems constituted cases in which averaged bootstrapped $\tilde{k}_{d1}$ successfully estimated $a_{CDOM}(440)$; non-conservative ecosystems constituted cases where averaged bootstrapped $\tilde{k}_{d1}$ did not estimate $a_{CDOM}(440)$ successfully. We then re-evaluated the relationship between averaged bootstrapped $\tilde{k}_{d1}$ vs. $a_{CDOM}(440)$ and $\tilde{k}_{d2}$ vs. $a_{CDOM}(440)$ for conservative ecosystems using linear least-squares regression and compared it to Hooker et al. [15]. $\tilde{k}_{d1}$ vs. $a_{CDOM}(440)$ of non-conservative

ecosystems were overlaid onto this best-fit line to compare them with watermasses deemed to be non-conservative by Hooker et al. [15].

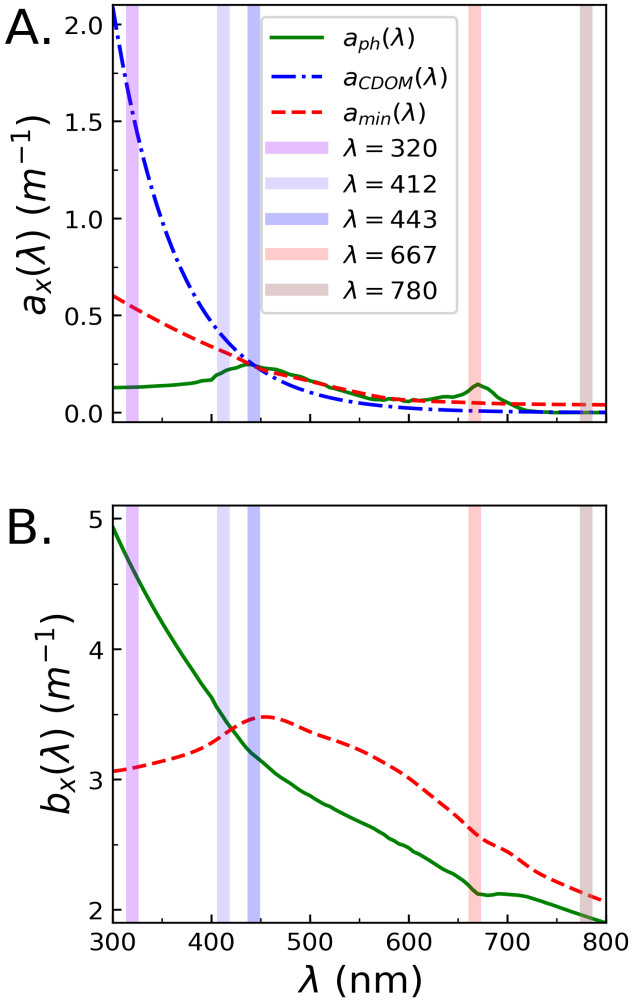



**Figure 4.** Spectral absorption (a) components and scattering (b) components as computed for ecosystem #175 overlaid with color-coded vertical lines indicating $\lambda =$ 320, 412, 443, 670, and 780 nm. Bio-optical constituent HE53 inputs were as follows: Chl = 8.845 $\mu g\ L^{-1}$, $a_g(443) = 0.256\ m^{-1}$, and TSM = 3.89 $g\ m^{-3}$.

## 3. Results

Our results demonstrated EMA's utility in estimating $a_{CDOM}(440)$ for each of our nine phase functions ($R^2 > 0.95$). Phase functions for $\tilde{k}_{d1}$ and $\tilde{k}_{d2}$ also indicated that the steepness, or slope of goodness of fit curves increase with $\tilde{b}_{ph}$ and $\tilde{b}_{min}$ (Fig. 5), although the $\tilde{k}_{d1}$ vs. $\hat{a}_{CDOM}(440)$ relationship was much less sensitive to phase function than $\tilde{k}_{d2}$ vs. $\hat{a}_{CDOM}(440)$ (Figs. 5 & 6). Bootstrapped linear coefficients used to characterize $\tilde{k}_{d1}$ vs. $a_{CDOM}(440)$ exhibited $\sigma$'s that accounted for <1.7% of slope and < 4.5% of y-intercept signals (Fig. 6a). In contrast, $\sigma$'s of bootstrapped parabolic coefficients, used to characterize $\tilde{k}_{d2}$ vs. $a_{CDOM}(440)$, accounted for >14% of their signals (Fig. 6b). The impact of phase function on $\tilde{k}_{d2}$ became more pronounced as $\tilde{k}_{d2}$ increased (Fig. 5b). Importance of phase function also increased with $\tilde{k}_{d1}$, but to a lesser degree (Fig. 5a).

According to our criteria, $\tilde{k}_{d1}$ and $\tilde{k}_{d2}$ successfully estimated $a_{CDOM}(440)$ for 934 and 944 of ecosystems, respectively. Six and eight of the ecosystems that $\tilde{k}_{d1}$ and $\tilde{k}_{d2}$ could *not* estimate were outliers (Fig. 6). Ecosystems with the highest and second highest IOP component for each bio-optical constituent were also $\tilde{k}_{d1}$ outliers (Fig. 7). Three of the six $\tilde{k}_{d1}$ outliers also sorted into their own k-means cluster (Fig. 7). For five of the $\tilde{k}_{d1}$ outliers, $a_{min}(443)$ or $a_{CDOM}(443)$ accounted for > 70% $a(443)$ (Fig. 8a). $\tilde{k}_{d2}$ outliers did not demonstrate the same consistency as $\tilde{k}_{d1}$. Only two $\tilde{k}_{d2}$

outliers, #331 and #472 were also $\tilde{k}_{d1}$ outliers (Fig. 6). Of the remaining six, we observed no overarching patterns (Figs. 7 & 8b).

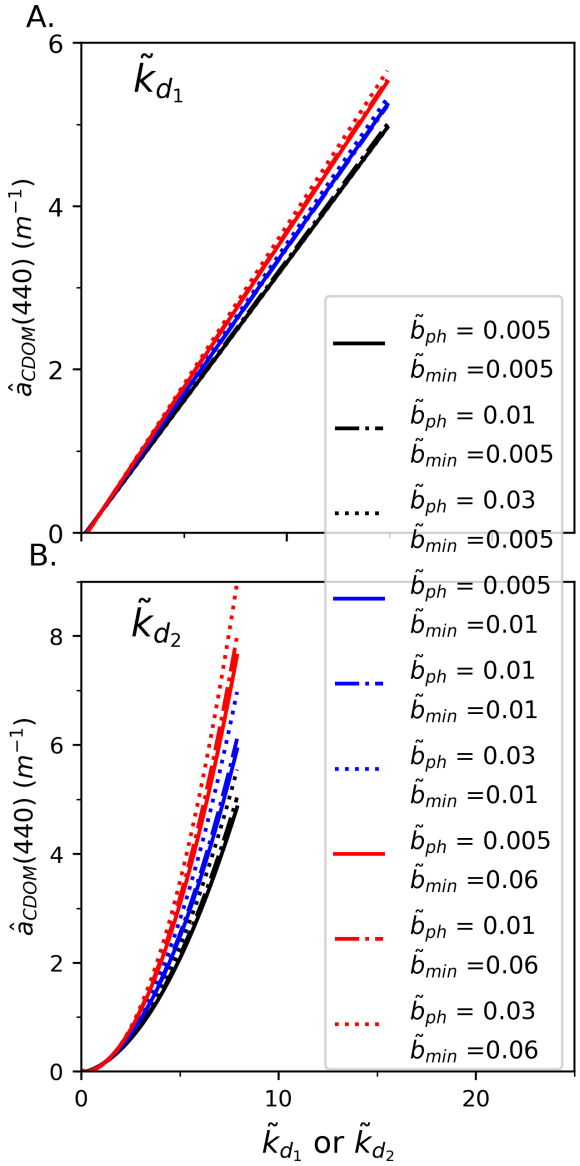



**Figure 5.** $\tilde{k}_{d1}$ vs. $\hat{a}_{CDOM}(440)$ (a) and $\tilde{k}_{d2}$ vs. $\hat{a}_{CDOM}(440)$ (b) least-squares regressions for all nine Fournier-Forand phase functions.

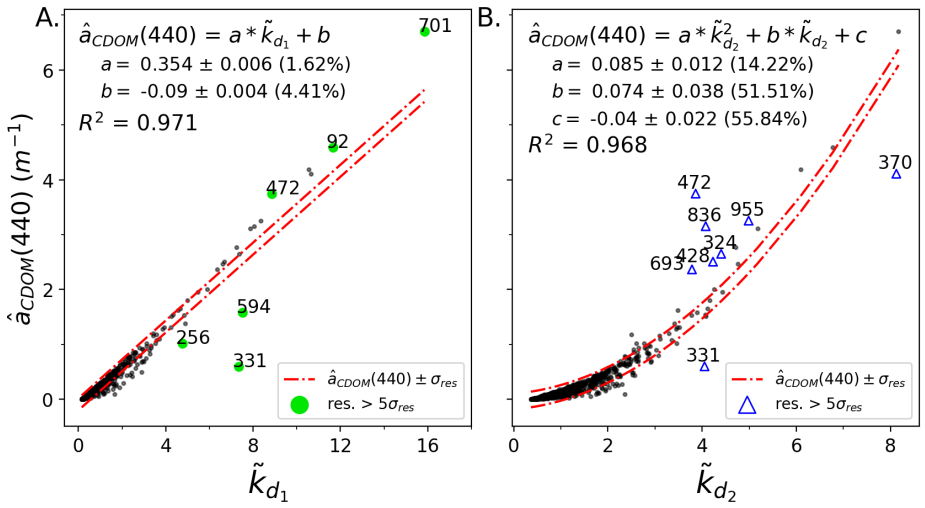



**Figure 6.** Comparisons of bootstrapped mean $\tilde{k}_{d1}$ vs. $a_{CDOM}(440)$ (a) and $\tilde{k}_{d2}$ vs. $a_{CDOM}(440)$ (b) of all ecosystems, overlaid with curves indicating the threshold for EMA successfully estimating $a_{CDOM}(440)$. Excluded from least-squares regression, ecosystem outliers are indicated with alternative markers. Least-squares coefficients, their phase function associated uncertainties, and $R^2$'s are also displayed.

K-means indicated different success rates for EMA across clusters. Four of the clusters contained only one ecosystem each. Three of these single-ecosystem clusters, C-2 (#594), C-3 (#331), and C-10 (#256), represented outliers for $\tilde{k}_{d1}$. C-3's single ecosystem (#331) is an outlier for both $\tilde{k}_{d1}$ and $\tilde{k}_{d2}$ (Fig. 7). The fourth cluster, C-4 (#324), represented an outlier for $\tilde{k}_{d2}$. These single cluster ecosystems had the four highest TSM values: 1000, 731.9, 146.8, and 75.2 $g\ m^{-3}$. Of these four clusters, $a_{CDOM}(440)$ was successfully estimated only for C-2 (#594) and only with $\tilde{k}_{d2}$.

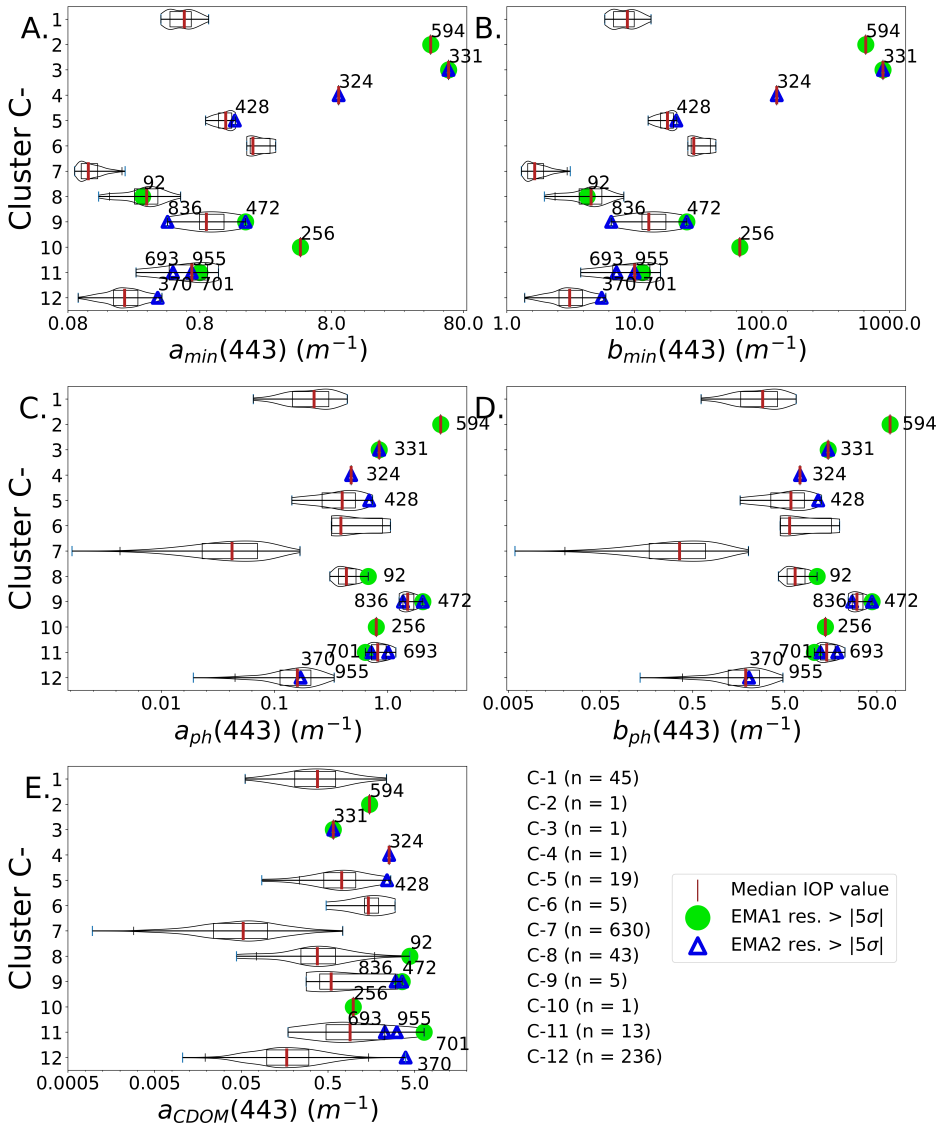



**Figure 7.** Boxplots with probability densities for $a_{min}(443)$ (a), $b_{min}(443)$ (b), $a_{ph}(443)$ (c), $b_{ph}(443)$ (d), and $a_{CDOM}(443)$ (e) for k-means clusters. $\tilde{k}_{d1}$ and $\tilde{k}_{d2}$ outlier values are overlaid with labels on top of their clusters. Median values are denoted with red lines.

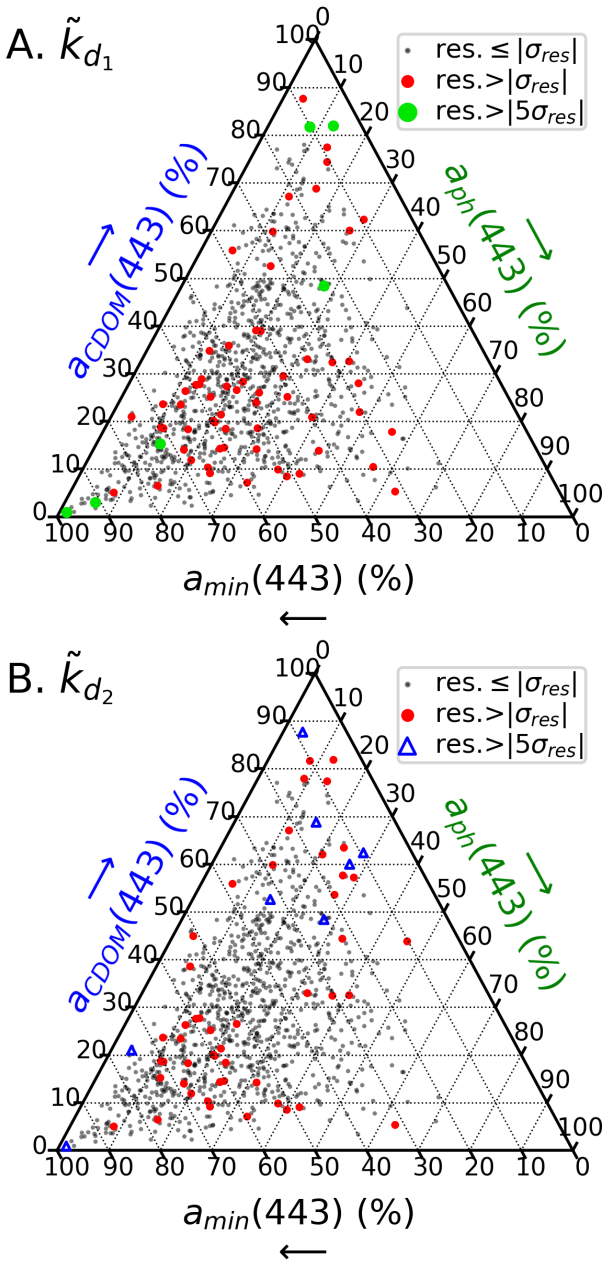



**Figure 8.** Ternary plots depicting the relative contributions (%) of $a_{CDOM}(443)$, $a_{ph}(443)$, and $a_{min}(443)$ for ecosystems. Black and red circles denote ability and inability of $\tilde{k}_{d1}$ (a) and $\tilde{k}_{d2}$(b) to estimate $a_g(440)$. Outliers are labeled and denoted with green circles ($\tilde{k}_{d1}$) or blue triangles ($\tilde{k}_{d2}$).

Clusters C-7, C-12, and C-8, comprise ~91% of the modeled ecosystems (n = 909). C-7, the largest of our 12 clusters (n = 630), exhibits 100% utility in estimating $a_{CDOM}(440)$ with $\tilde{k}_{d1}$ and $\tilde{k}_{d2}$ (Table 2). C-7 is indicative of low-biomass, oligotrophic ecosystems, typical of the open ocean, as evidenced by low IOP components (Fig. 7). C-12 and C-8 with their low suspended sediments and heightened CDOM and phytoplankton concentrations, resemble case-1 aquatic ecosystems, for which bio-optical constituents (e.g., CDOM) co-vary with phytoplankton [40]. However, as phytoplankton and CDOM IOP components increased, success of $\tilde{k}_{d1}$ and $\tilde{k}_{d2}$ to estimate $a_{CDOM}(440)$ diminished. $\tilde{k}_{d1}$ and $\tilde{k}_{d2}$ successfully estimated $a_{CDOM}(440)$ in >99% of cases for C-12, but this decreased to 86% and 78% for C-8, which exhibited increased phytoplankton and CDOM IOP components relative to C-12 (Table 2). $\tilde{k}_{d1}$ and $\tilde{k}_{d2}$ demonstrated decreased ability to estimate $a_{CDOM}(440)$ for C-1 compared to C-8 ecosystems, estimating $a_{CDOM}(440)$ in 53% and 64% of cases (Table 2). C-1 exhibited increased overall $a_{min}(443)$ and $b_{min}(443)$, but decreased $a_{ph}(443)$ and $b_{ph}(443)$ relative to C-8; $a_{CDOM}(443)$ levels were similar between the two clusters (Fig. 7). C-1's increased suspended sediment and decreased phytoplankton IOP components, relative to C-8, may share similarities with coastal ecosystems that are subject to terrigenous runoff (e.g., river plumes). We would expect them to be high in sediment and CDOM.

**Table 2. Overview of k-means cluster analysis indicating the cluster ID, number of ecosystems assorted into each cluster ($n_i$), success rate (utility) of $\widetilde{k}_{d1}$ and $\widetilde{k}_{d2}$ in estimating $a_{CDOM}(440)$.**

| Cluster ID | $n_i$ | $\tilde{k}_{d1}$ Utility | $\tilde{k}_{d2}$ Utility |
|---|---|---|---|
| C-1 | 45 | 53.3% | 64.4% |
| C-2 | 1 | 0% | 100% |
| C-3 | 1 | 0% | 0% |
| C-4 | 1 | 0% | 0% |
| C-5 | 19 | 21.1% | 52.6% |
| C-6 | 5 | 40% | 20% |
| C-7 | 630 | 100% | 100% |
| C-8 | 43 | 86% | 79.1% |
| C-9 | 5 | 0% | 40% |
| C-10 | 1 | 0% | 0% |
| C-11 | 13 | 15.3% | 23.1% |
| C-12 | 236 | 99.6% | 99.2% |

$\tilde{k}_{d1}$ and $\tilde{k}_{d2}$ were less reliable at estimating $a_{CDOM}(440)$ within C-5, C-6, C-9, and C-11 ecosystems, achieving success rates of $\leq 60\%$, with respective lows of 0% and 20% at C-9 and C-6 (Table 2). We believe that these four clusters are similar to lacustrine, riverine, and estuarine ecosystems, which are known for being highly productive and case-2, with CDOM and suspended sediment comprising significant components of the optical properties [40]. With regard to their IOP components, these clusters resembled C-1; however, each cluster exhibited two IOP components whose ranges exceeded those of C-1 (Fig. 7). C-1, C-5, C-6, C-9, and C-11 all exhibited overlapping $a_{CDOM}(443)$ ranges (Fig. 7e). C-1, C-9, and C-11 ecosystems exhibited overlapping $a_{min}(443)$ and $b_{min}(443)$ values, but $a_{ph}(443)$ and $b_{ph}(443)$ values

exhibited by C-9 and C-11 exceeded those of C-1. Conversely, $a_{ph}(443)$ and $b_{ph}(443)$ values of C-5 and C-6 ecosystems overlapped with C-1 ecosystems, while $a_{min}(443)$ and $b_{min}(443)$ values (with the exception of one C-5 ecosystem) were greater than C-1 (Figs. 7a, b, d, & e). Assuming that C-1 is indicative of river plumes and C-5, C-6, C-9, and C-11 are indicative of inland habitats, these results are intuitive. As inland waters empty into the ocean, their highly concentrated bio-optical constituents would begin to dilute, lowering their IOPs.

In comparing the goodness of fits for conservative ecosystems, we report slopes and y-intercepts of 0.34 and -0.072 for $\tilde{k}_{d1}$ vs. $a_{CDOM}(440)$, and 0.367 and -0.215 for $\tilde{k}_{d2}$ vs. $a_{CDOM}(440)$ (Fig. 9). These $\tilde{k}_{d1}$ and $\tilde{k}_{d2}$ vs. $a_{CDOM}(440)$ slopes differed by 31.6% and 4.7% from slopes reported by Hooker et al. [15] (Fig. 9). We also report that despite the exclusion from the analysis of all values of $a_{CDOM}(440) > 2$ and $\tilde{k}_{d2} > 5$, a parabolic curve ($R^2$=0.964) fit these data better than a straight line ($R^2$=0.902). Moreover, excluding non-conservative ecosystems altered parabolic coefficients by $\leq$ 8.1%, well within the $>$ 14% margins of uncertainty established by bootstrapping (Figs. 6b). With the exception of C-2, C-3, and C-10, non-conservative ecosystems did not segregate by cluster along the $\tilde{k}_{d1}$ vs. $\hat{a}_{CDOM}(440)$ curve (Fig. 10).

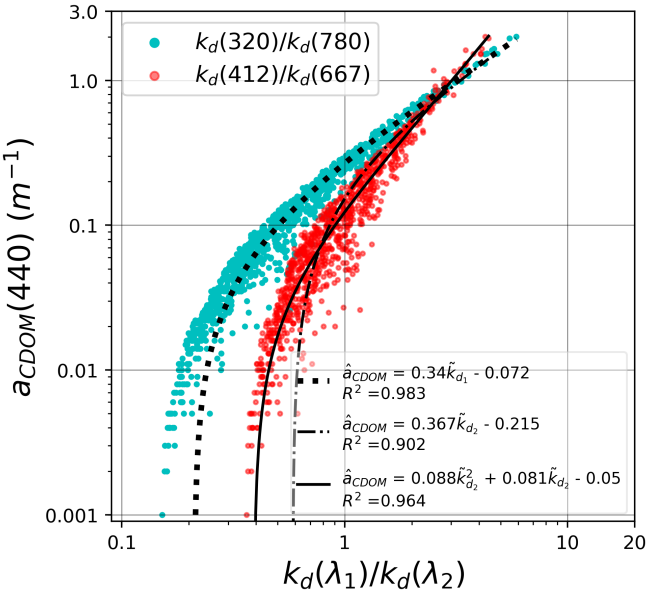



**Figure 9.** Comparisons of bootstrapped mean $\tilde{k}_{d1}$ vs. $a_{CDOM}(440)$and $\tilde{k}_{d2}$ vs. $a_{CDOM}(440)$ of conservative ecosystems, overlaid with linear and parabolic ($\tilde{k}_{d2}$ only) best fits calculated via least-squares regression. Similar to Hooker et al. [15], data were plotted on logarithmic axes.

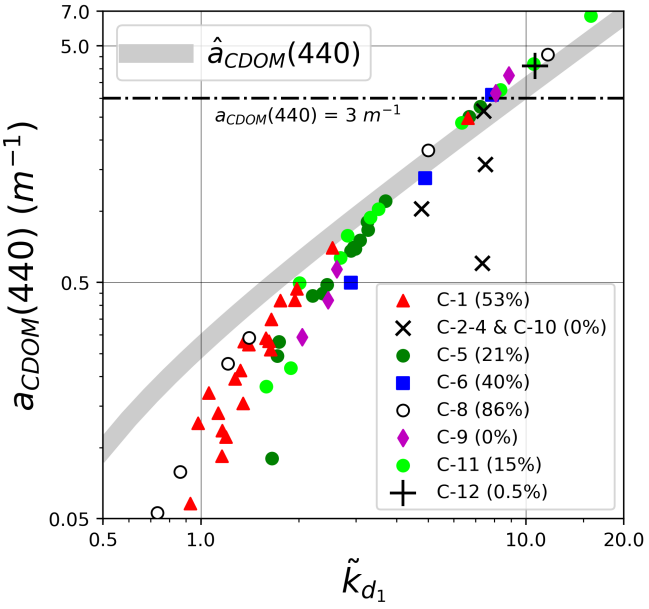



**Figure 10.** Comparisons of bootstrapped mean $\tilde{k}_{d1}$ vs. $a_{CDOM}(440)$ of non-conservative ecosystems overlaid with the $\tilde{k}_{d1}$ vs. $\hat{a}_{CDOM}(440)$ curve for conservative ecosystems (Fig. 9).

## 4. Discussion

The high percentage of variance in $a_{CDOM}(440)$ that is explained by both $\tilde{k}_{d1}$ and $\tilde{k}_{d2}$ indicates that EMA follows radiative transfer theory. Consistent with Hooker et al. [4, 11, 15], our results show that $\tilde{k}_{d1}$ and $\tilde{k}_{d2}$ are highly correlated with $a_{CDOM}(440)$ (Figs 5 & 6). However, an algorithm's sensitivity to phase function is an extremely important factor when establishing its ability to characterize different aquatic habitat types. $\tilde{k}_{d1}$'s low degree of phase function-induced uncertainty is ideal in this regard as it is less likely to be susceptible to particle assemblages of a given ecosystem (Fig. 6a). On the other hand, the relationship between $\tilde{k}_{d2}$ and $a_{CDOM}(440)$ could be much more dependent on particle assemblages and their scattering characteristics, as evidenced by $\tilde{k}_{d2}$'s higher degree of uncertainty associated with phase function (Figs. 5b & 6b). This higher degree of uncertainty means that prior knowledge of an ecosystem's particle phase function (e.g., $\tilde{b}_{ph}$ and $\tilde{b}_{min}$) may be necessary in order to improve $a_{CDOM}(440)$ estimations using $\tilde{k}_{d2}$. Phase function, however, is difficult to predict without in-situ measurements. For example, $\tilde{b}_{ph}$ typically increases with cell size, which has been observed to be correlated with nutrient abundance [41]. Nutrients, in turn, are typically more abundant in ecosystems with high concentrations of bio-optical constituents (e.g., inland and coastal) (Figs. 5 & 6). Theoretically, because $\tilde{k}_{d1}$ and $\tilde{k}_{d2}$ are related to the total concentration of these constituents, nutrient abundance would intuitively be related to $\tilde{b}_{ph}$ as well. However, this assumption is problematic, as relationships

between cell size and $\tilde{b}_{ph}$ do not account for differences in phytoplankton functional type (e.g., silicate cell walls) [34]. Furthermore, relationships between biomass (e.g., Chl) and $\tilde{b}_{ph}$ are inconsistent (e.g., [42, 43]). $\tilde{b}_{min}$ is highly dependent on chemical composition of mineral particulates, namely their proportion of inorganic minerals relative to detritus [37, 44]. Suspended particle characteristics are also dictated in large part by geography [23, 45-47]. Taking into account the difficulty in predicting $\tilde{b}_{ph}$ and $\tilde{b}_{min}$, our findings suggest $\tilde{k}_{d1}$to be more reliable in estimating $a_{CDOM}(440)$, especially with limited knowledge of a watermass' particle assemblage (Fig. 6). $\tilde{k}_{d2}$'s increased sensitivity to phase function offers a plausible explanation for its increased deviation from $\hat{a}_{CDOM}(440)$, as observed in the field [4, 11, 15]. Moreover, similarity of our $\tilde{k}_{d2}$ vs. $a_{CDOM}(440)$ goodness of fit slope (Fig. 9) with that of Hooker et al. [15] lend credence to the adequacy of Fournier-Forand's [33] phase function in approximating $\tilde{k}_{d2}$'s general relationship with $a_{CDOM}(440)$.

Similar to our findings for non-conservative ecosystems (e.g., Fig. 10), Hooker et al.'s [15] field-sampled ecosystems did not segregate along $\tilde{k}_{d1}$ vs. $\hat{a}_{CDOM}(440)$ by subcategory. Overlapping non-conservative ecosystems belonging to C-1, C-5, C-6, C-9, and C-11 (Fig. 10), were comparable to watermasses subcategorized by Hooker et al. [15] as "drought-stricken", "refilled", [subject to] "re-suspension", and [in close proximity to a] "harbor". In addition to the aforementioned subcategories, C-1 coincided with watermasses in close proximity to glaciers, subcategorized as "closer to ice" [15]. All of these subcategories are associated with high sediment and

underreported $a_{CDOM}(440)$ with respect to $\hat{a}_{CDOM}(440)$. We attribute this underreported $a_{CDOM}(440)$ to sediments disproportionately contributing to increases in $\tilde{k}_{d1}$ relative to CDOM and shifting it to the right of the $\tilde{k}_{d1}$ vs. $\hat{a}_{CDOM}(440)$ curve. We also believe that disproportionate sediment contributions explain positions of C-2, C-3, and C-10 relative to the $\tilde{k}_{d1}$ vs. $\hat{a}_{CDOM}(440)$ curve. These clusters are positioned similarly to White Lake and Lake Oroville, both "refilled" lakes [15]. We note that despite our previous assertion about C-1, none of our ecosystems could be classified as being "farther from ice" or "river mouths". These subcategories were characterized by $a_{CDOM}(440) < 1\ m^{-1}$, but over reported $a_{CDOM}(440)$ with respect to $\hat{a}_{CDOM}(440)$.

Four of the six non-conservative C-8 ecosystems ($a_{CDOM}(440) < 0.3\ m^{-1}$) resemble C-1 (Fig. 10) [15]. In addition to the aforementioned watermass subcategories that are high in sediment, these C-8 ecosystems also overlap with "harmful algal bloom" watermasses, sampled predominantly from Monterey Bay. Monterey Bay has several similarities with C-8 ecosystems, namely constrained sediments with co-varying CDOM and phytoplankton. In these circumstances, we believe that phytoplankton acts similarly to sediment by increasing $\tilde{k}_{d1}$relative to $a_{CDOM}(440)$. However, as $a_{CDOM}(440)$ increases ($> 1\ m^{-1}$) in conjunction with phytoplankton, as is the case in highly productive lakes (e.g., Pinto and Dog Lakes), $\tilde{k}_{d1}$ underestimates $a_{CDOM}(440)$ (Fig. 10). This underestimation may result from $\tilde{b}_{ph} < \tilde{b}_{min}$ [37, 44], which means that $\tilde{k}_{d1}$ is less sensitive to increases in phytoplankton than increases in sediment. An

equally plausible, non-mutually exclusive explanation is the non-linear relationship between IOPs and AOPs, meaning that $\tilde{k}_{d1}$'s sensitivity to IOPs gradually diminishes as the latter increases. Because bio-optical constituents correlate in our dataset, ecosystems with $a_{CDOM}(440) > 3\ m^{-1}$ also exhibit extremely high $a(\lambda)$ and $b(\lambda)$, which could explain why all such ecosystems (regardless of cluster) over reported $a_{CDOM}(440)$ with respect to $\hat{a}_{CDOM}(440)$. Intuitively we would surmise that in nature, such watermasses (e.g., small lakes, bogs, shallow creeks, high-residence time estuaries, etc.) are also likely to exhibit correlations between phytoplankton, sediments, and CDOM (Fig. 3), which suggests that $\tilde{k}_{d1}$ may be prone to underestimating $a_{CDOM}(440)$ at extreme CDOM concentrations. However, Hooker et al. [15] did not sample watermasses for which $a_{CDOM}(440) > 3\ m^{-1}$, possibly due to the physical limitations associated with in-water profilers (e.g., water column being too shallow).

Based on our analysis, we hypothesize that the primary predictor of EMA's success in estimating $a_{CDOM}(440)$ is an ecosystem's total concentration of bio-optical constituents, as quantified by $a(\lambda)$ and $b(\lambda)$. This hypothesis is supported by our k-means cluster analysis, which suggests that $\tilde{k}_{d1}$best estimates $a_{CDOM}(440)$ within clusters characterized by low IOPs, and that its utility diminishes as IOP components increase (Table 2; Fig. 7). Fig. 11 demonstrates this diminishing utility more clearly by showing the existence of an IOP threshold ($a(443) > 1\ m^{-1}$ and $b(443) > 10\ m^{-1}$), above which the utility of $\tilde{k}_{d1}$ (and $\tilde{k}_{d2}$) drops precipitously. It can also be

demonstrated quantitatively by comparing $\sigma_{res}$ of ecosystems that fall above and below this IOP threshold, which differ by factors of 8.2 ($\tilde{k}_{d1}$) and 2.4 ($\tilde{k}_{d2}$) (Table 3). The lack of a discernible pattern between $\tilde{k}_{d1}$'s utility and relative $a_g(443)$, $a_{ph}(443)$, and $a_{min}(443)$ (Fig. 8), further supports our assertion that relative contribution of bio-optical constituents to IOPs is less important than total IOPs (Fig. 11). Because phytoplankton, CDOM, and minerals absorb and scatter differently at 320 and 780 nm (Fig. 4), their relative contributions differentially impact $k_d(320)$, $k_d(780)$, and ultimately $\tilde{k}_{d1}$. We theorize that strong empirical relationships between $\tilde{k}_{d1}$ and $a_{CDOM}(440)$ are based on the broadly observed correlations between phytoplankton, CDOM, and sediments (e.g., Fig. 3) and that $\tilde{k}_{d1}$ successfully estimates $a_{CDOM}(440)$ in ecosystems in which IOP components exist within certain ratios. We hypothesize that at low bio-optical constituent concentrations (e.g., C-7), $\tilde{k}_{d1}$ is relatively insensitive to ratio changes in IOP components, but becomes increasingly more so as IOPs increase. At very high IOPs, even modest proportional changes in ratios of IOP components could have a pronounced effect on $k_d(\lambda)$. This increased sensitivity in response to IOP increases would explain $\tilde{k}_{d1}$'s disproportionate failure to estimate $a_{CDOM}(440)$ in ecosystems with high $a(\lambda)$ and $b(\lambda)$ as we would expect in many of Hooker et al.'s [15] non-conservative watermasses; it would also explain the aforementioned inconsistency between relative $a_{CDOM}(443)$, $a_{ph}(443)$, and $a_{min}(443)$ and utility of $\tilde{k}_{d1}$ (Fig. 8).

**Table 3. $\sigma_{res}$ of ecosystems partitioned above and below the IOP threshold of $a(443) > 1\ m^{-1}$ and $b(443) > 10\ m^{-1}$ ($\tau$) for average bootstrapped $\tilde{k}_{d1}$ and $\tilde{k}_{d2}$ vs. $a_{CDOM}(440)$.**

| | $\leq \tau$ | $> \tau$ |
|---|---|---|
| $\tilde{k}_{d1}$ | 1.22 | 10.67 |
| $\tilde{k}_{d2}$ | 5.92 | 14.39 |

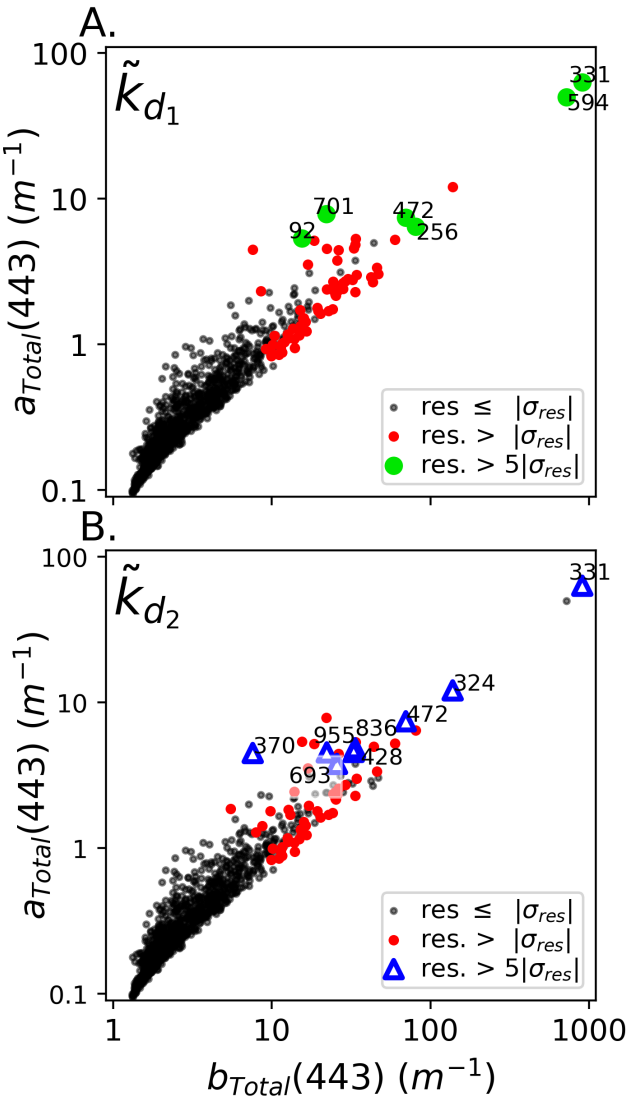



**Figure 11.** Scatterplot of total absorption ($a(443)$) over total scattering ($b(443)$) coefficients at $\lambda = 443$ nm for ecosystems. Black and red circles depict ability and

inability of $\tilde{k}_{d1}$ (a) and $\tilde{k}_{d2}$ (b) to estimate $a_g(440)$. Ecosystem outliers are labeled and denoted with green circles ($\tilde{k}_{d1}$) or blue triangles ($\tilde{k}_{d2}$).

The persistence of a parabolic relationship between $\tilde{k}_{d2}$ and $a_{CDOM}(440)$, despite the removal of all ecosystems with $a_{CDOM}(440) > 2$ and $\tilde{k}_{d2} > 5$ (Fig. 9), suggests that it is not an artifact. Hooker et al. [4, 11] report a similar relationship between $\tilde{k}_{d2}$ and $a_{CDOM}(440)$ in the field, further suggesting this parabolic relationship to be based on radiative transfer theory. The exponential nature of $a_{CDOM}(\lambda)$ (Fig. 4; Table 1), coupled with negligible $a(\lambda)$ and diminished $b(\lambda)$ in the NIR, means that the farther $k_d(\lambda_1)$ and $k_d(\lambda_2)$ are located in the UV and NIR, the stronger the $a_{CDOM}(\lambda)$ signal on $k_d(\lambda_1)/k_d(\lambda_2)$. These observations could explain the linear relationship between $\tilde{k}_{d1}$ and $a_{CDOM}(440)$ reported by Hooker et al. [4, 11] and corroborated by our findings (Figs. 6a & 7a). Alternatively, as $k_d(\lambda_1)$ moves into the blue the impact of $a_{CDOM}(\lambda)$, relative to $a_{ph}(\lambda)$ and $a_{min}(\lambda)$ decreases. Moreover, the migration of $k_d(\lambda_2)$ from the NIR into the red not only increases its sensitivity to $b(\lambda)$ and $b_{bp}(\lambda)$), but also $a_{ph}(\lambda)$, which absorbs strongly in the red (Fig. 4). These changes likely resulted in the truncated $\tilde{k}_{d2}$ scale (relative to $\tilde{k}_{d1}$), as well as its parabolic relationship with $a_{CDOM}(440)$ reported here (Figs. 5b & 6b) and in the field [4, 11]. Notwithstanding, $\tilde{k}_{d2}$ exhibited the same broad patterns as $\tilde{k}_{d1}$ with respect to $R^2$, its performance across different clusters (Table 2), and its diminishing utility with increasing IOPs (Fig. 11b). We attribute these similarities to the aforementioned relationships between bio-optical coefficients on which NOMAD, and by extension

our ecosystems, are based (Figs. 2 & 3). $\tilde{k}_{d2}$'s ability to estimate $a_{CDOM}(440)$ may also be dependent on the adherence of ecosystems to a particular ratio of IOP components, and like $\tilde{k}_{d1}$, $\tilde{k}_{d2}$'s sensitivity to this ratio could increase with the total concentration of bio-optical constituents (and IOPs) (Figs. 8b & 11b). However, $a_{CDOM}(\lambda)$'s decreased signal with respect to $\tilde{k}_{d2}$ suggests that this ratio may differ from that of $\tilde{k}_{d1}$. This decreased signal could explain why $\tilde{k}_{d2}$ estimated $a_{CDOM}(440)$ for some ecosystems for which $\tilde{k}_{d1}$ did not (and vice versa) as well as the discrepancies between $\tilde{k}_{d1}$ and $\tilde{k}_{d2}$ outliers (Fig. 11).

Judging by high values for $R^2$ (e.g., Figs 5 & 6), our findings as well as those of Hooker et al. [4, 11, 15] suggest that both $\tilde{k}_{d1}$ and $\tilde{k}_{d2}$ can estimate $a_{CDOM}(440)$ across a wide range of habitats. It is important to note however, that all of our individual analyses, including average bootstrapped $\tilde{k}_{d1}$and $\tilde{k}_{d2}$, assumed the same phase function across all ecosystems. However, its increased sensitivity with regard to phase function makes $\tilde{k}_{d2}$ less reliable than $\tilde{k}_{d1}$ for estimating $a_{CDOM}(440)$, especially in ecosystems with moderate to high concentrations of bio-optical constituents. Hooker et al. [4, 11] appear to reflect this sensitivity by reporting a decline in $R^2$ (0.99 to 0.94) associated with $\tilde{k}_{d2}$. However, this modest decline in $R^2$ may be an overly optimistic assessment of $\tilde{k}_{d2}$ because Hooker et al. [4, 11] only sampled watermasses within a limited number of habitats (e.g., Mackenzie River and Beaufort Sea). Thus Hooker et al. [4, 11] may have underestimated $\tilde{k}_{d2}$'s phase

function sensitivity, as we would expect watermasses within the same river to exhibit greater similarities in their suspended particle populations than would geographically diverse ecosystems. Indeed Hooker et al. [15], which evaluated EMA in an assemblage of ecosystems spanning North America, report a five-fold difference in RMSE between $\tilde{k}_{d2}$ and $\tilde{k}_{d1}$ when characterizing $a_{CDOM}(440)$ empirically.

In closing, we point to several assumptions and potential sources of error connected to our work. First, it is important to disclose that NOMAD sampled Chl using fluorometric and HPLC techniques at different stations. We decided to use these values interchangeably after comparing a subset of all NOMAD stations that measured Chl using both techniques and finding no discernible offsets or biases associated with them. We also acknowledge that $R_{rs}(670)$ is an indirect proxy for sediment and thus Nechad et al. [30] are subject to error. Although HE53 assumed TSM to be exclusively a "mineral", or non-algal component, $a_{min}(\lambda)$ and $b_{min}(\lambda)$ do account for organic particles. While there is no substitute for directly measured TSM, we point out that Nechad et al. [30] have been demonstrated to be reliable (e.g., [32, 48]) and concentration ranges of non-algal sediments ranges are three orders of magnitude greater than those of phytoplankton pigments [10, 31, 42]. As with any study that relies on modeling, we had to resort to some oversimplifications due to time and computational constraints. As such, $a_{ph}(\lambda)$ is based on the average compliment of photosynthetic pigments present in the "typical" phytoplankton; all $a_{CDOM}(\lambda)$ use a constant spectral slope; and $a_{min}(\lambda)$ and $b_{min}(\lambda)$ were spectral

'averages' for brown earth, red clay, yellow clay, and calcareous sand. We accept that these approximations of spectral IOP components may be overly simplistic, and may account at least partially for $\tilde{k}_{d1}$ vs. $a_{CDOM}(440)$ slope differences between our conservative ecosystems and those of Hooker et al. [15]. However, we believe that EMA's reliance on end-members, rather than spectral shapes, significantly mitigates the potential scopes of these errors. We also understand that several of the assumptions surrounding Fournier-Forand phase functions (e.g., spherical, homogeneously-distributed, non-absorbing particles) may be unrealistic for certain habitats. However, our purpose in using multiple phase functions was to demonstrate EMA's potential sensitivity to changing particle assemblages. Finally, all field data including NOMAD are subject to a degree of selection bias. Although our synthetic dataset expands upon NOMAD, it is still reflects NOMAD in terms of the distributions and relationships of both its bio-optical constituents and its optical properties. The two datasets compiled by International Ocean Color Coordinating Group (IOCCG), one in-situ and one simulated, set precedent for our methodology [49]. To an extent, our simulated dataset builds upon IOCCG data by providing the best of both worlds: AOPs and IOPs based on an assortment of actual watermasses without errors caused by measurement procedures.

## 5. Conclusion

The purpose of our study was to structurally evaluate EMA's global potential by examining its conformity to radiative transfer theory, as well as by evaluating its

potential strengths and limitations using modeled data. Modeled data offer several advantages in evaluating empirical algorithms: 1) modeled data allow us to evaluate algorithms under an expanded scope of ecosystem properties relative to field data; 2) data acquisition is not limited significantly by money or time constraints; 3) modeled data can predict where and under which circumstances an algorithm is likely to work; and 4) modeled data allow us to examine the underlying mechanisms that impact algorithm performance. In fulfilling these advantages modeled data are important not only for evaluating EMA, but also for extending its usage to airborne and satellite sensors. For example, $\tilde{k}_{d1}$'s robustness with regard to phase function (relative to $\tilde{k}_{d2}$) suggests that EMA would work best in conjunction with next-generation satellite sensors that are capable of measuring in the ultraviolet (UV) and near-infrared (NIR) (e.g., PACE). Conversely, it can still be applied to MODIS bands but could be less reliable in estimating $a_{CDOM}(440)$, as indicated by $\tilde{k}_{d2}$'s sensitivity to phase function, especially in habitats with high bio-optical constituent concentrations, such as rivers, estuaries, lakes, or phytoplankton blooms. For these systems, studies relying on MODIS imagery would benefit from pre-existing knowledge of particle populations and the phase functions that characterize them. However, applying EMA to MODIS could prove challenging in dynamic ecosystems in which characteristics of suspended particles are continually in flux. Although satellite algorithms exist that are designed to determine particle size distributions, they are limited in scope, especially in highly productive aquatic ecosystems [50, 51]. Their continued development could greatly enhance our capacity to estimate $a_{CDOM}(440)$ with MODIS.

Finally, it is important to note that $k_d(\lambda)$ is not directly measured with airborne or satellite sensors and must be estimated. Multiple algorithms exist that estimate $k_d(\lambda)$ from above-water measurements (e.g., [52-55]). These algorithms first need to be validated across a wide range of ecosystems to determine their utility before they can be applied to satellites. This validation will likely involve Hydrolight modeling, as well as the simultaneous deployment of in-water optical profilers and airborne instrumentation. The extra step of estimating $k_d(\lambda)$ above-water will add additional error to $a_{CDOM}(440)$ estimations, especially in the aforementioned riverine, estuarine, and coastal ecosystems. However, we believe that despite these decreases in accuracy, the validation of above-water $k_d(\lambda)$ algorithms could enable satellite and airborne sensors to spatially characterize relative differences in $\hat{a}_g(440)$, which could then be used to classify, fingerprint, and track the movement of those watermasses.

## 6. References


1. A. Charo, and W. Abdalati, "The 2017-2027 National Academies Decadal Survey for Earth Science and Applications from Space: An Overview of the Report," in *42nd COSPAR Scientific Assembly*(2018).

2. S. Sarthyendranath, "Remote sensing of ocean colour in coastal, and other optically-complex, waters," (2000).

3. S. Chandrasekhar, *Radiative Transfer* (Dover Publications Inc, 1960).

4. S. Hooker, J. Morrow, and A. Matsuoka, "The 1% and 1 cm perspective in deriving and validating AOP data products," Biogeosciences Discussions **9** (2012).

5. R. M. Pope, and E. S. Fry, "Absorption spectrum (380–700 nm) of pure water. II. Integrating cavity measurements," Applied optics **36**, 8710-8723 (1997).

6. L. Prieur, and S. Sathyendranath, "An optical classification of coastal and oceanic waters based on the specific spectral absorption curves of phytoplankton pigments, dissolved organic matter, and other particulate materials," Limnology and Oceanography **26**, 671-689 (1981).

7. N. Tuchow, J. Broughton, and R. Kudela, "Sensitivity analysis of volume scattering phase functions," Optics express **24**, 18559-18570 (2016).

8. M. S. Twardowski, E. Boss, J. M. Sullivan, and P. L. Donaghay, "Modeling the spectral shape of absorption by chromophoric dissolved organic matter," Marine Chemistry **89**, 69-88 (2004).

9. S. A. Garver, and D. A. Siegel, "Inherent optical property inversion of ocean color spectra and its biogeochemical interpretation: 1. Time series from the Sargasso Sea," Journal of Geophysical Research: Oceans **102**, 18607-18625 (1997).

10. P. J. Werdell, and S. W. Bailey, "An improved in-situ bio-optical data set for ocean color algorithm development and satellite data product validation," Remote sensing of environment **98**, 122-140 (2005).

11. S. Hooker, J. Morrow, and A. Matsuoka, "Apparent optical properties of the Canadian Beaufort Sea; Part 2: The 1% and 1 cm perspective in deriving and validating AOP data products," Biogeosciences **10**, 4511 (2013).

12. E. J. D'Sa, and M. Korobkin, "Colored dissolved organic matter in the northern Gulf of Mexico using ocean color: seasonal trends in 2005," in *SPIE Remote Sensing*(International Society for Optics and Photonics2008), pp. 710505-710505-710508.

13. A. Mannino, M. E. Russ, and S. B. Hooker, "Algorithm development and validation for satellite‐derived distributions of DOC and CDOM in the US Middle Atlantic Bight," Journal of Geophysical Research: Oceans **113** (2008).

14. D. Siegel, S. Maritorena, N. Nelson, D. A. Hansell, and M. Lorenzi‐Kayser, "Global distribution and dynamics of colored dissolved and detrital organic materials," Journal of Geophysical Research: Oceans **107** (2002).

15. S. B. Hooker, A. Matsuoka, R. M. Kudela, Y. Yamashita, K. Suzuki, and H. F. Houskeeper, "A Global End-Member Approach to Derive a CDOM (440) from Near-Surface Optical Measurements," Biogeosciences Discussions, 1-51 (2019).

16. A. Matsuoka, A. Bricaud, R. Benner, J. Para, R. Sempéré, L. Prieur, S. Bélanger, and M. Babin, "Tracing the transport of colored dissolved organic matter in water masses of the Southern Beaufort Sea: relationship with hydrographic characteristics," Biogeosciences **9**, 925 (2012).

17. C. Guallar, and J. Flos, "Linking phytoplankton primary production and chromophoric dissolved organic matter in the sea," Progress in Oceanography **176**, 102116 (2019).

18. A. Bricaud, M. Babin, H. Claustre, J. Ras, and F. Tièche, "Light absorption properties and absorption budget of Southeast Pacific waters," Journal of Geophysical Research: Oceans **115** (2010).

19. J.-E. Thrane, D. O. Hessen, and T. Andersen, "The absorption of light in lakes: negative impact of dissolved organic carbon on primary productivity," Ecosystems **17**, 1040-1052 (2014).

20. M. D. Benoit, R. M. Kudela, and A. R. Flegal, "Modeled trace element concentrations and partitioning in the San Francisco estuary, based on suspended solids concentration," Environmental science & technology **44**, 5956-5963 (2010).

21. S. L. Palacios, T. D. Peterson, and R. M. Kudela, "Development of synthetic salinity from remote sensing for the Columbia River plume," Journal of Geophysical Research: Oceans **114** (2009).

22. S. L. Palacios, T. D. Peterson, and R. M. Kudela, "Optical characterization of water masses within the Columbia River plume," Journal of Geophysical Research: Oceans **117** (2012).

23. R. M. Kudela, and S. L. Palacios, "Optical characterization and age estimates of river plumes on the US west coast," in *Coastal Ocean Remote Sensing*(International Society for Optics and Photonics2007), p. 66800L.

24. H. Loisel, and A. Morel, "Light scattering and chlorophyll concentration in case 1 waters: A reexamination," Limnology and Oceanography **43**, 847-858 (1998).

25. C. D. Mobley, "Light and Water: Radiative Transfer in Natural Waters," (Elsevier, 1994), p. 592.

26. N. Blough, O. Zafiriou, and J. Bonilla, "Optical absorption spectra of waters from the Orinoco River outflow: Terrestrial input of colored organic

matter to the Caribbean," Journal of Geophysical Research: Oceans **98**, 2271-2278 (1993).

27. J. Mueller, J. MuelIer, C. Pietras, S. Hooker, D. Clark, A. M. R. Frouin, and G. Fargion, "Ocean optics protocols for satellite ocean color sensor validation, revision 3, volumes 1 and 2," in *NASA tech. memo*(2002).

28. J. L. Mueller, and R. W. Austin, *Ocean optics protocols for SeaWiFS validation* (National Aeronautics and Space Administration, Goddard Space Flight Center, 1992).

29. M. D. McKay, R. J. Beckman, and W. J. Conover, "Comparison of three methods for selecting values of input variables in the analysis of output from a computer code," Technometrics **21**, 239-245 (1979).

30. B. Nechad, K. Ruddick, and Y. Park, "Calibration and validation of a generic multisensor algorithm for mapping of total suspended matter in turbid waters," Remote Sensing of Environment **114**, 854-866 (2010).

31. J. R. Gray, *Comparability of suspended-sediment concentration and total suspended solids data* (US Department of the interior, US Geological Survey, 2000).

32. A. Hilton, J. Bausell, and R. Kudela, "Quantification of Polychlorinated Biphenyl (PCB) Concentration in San Francisco Bay Using Satellite Imagery," Remote Sensing **10**, 1110 (2018).

33. G. R. Fournier, and J. L. Forand, "Analytic phase function for ocean water," in *Ocean Optics XII*(International Society for Optics and Photonics1994), pp. 194-201.

34. A. L. Whitmire, W. S. Pegau, L. Karp-Boss, E. Boss, and T. J. Cowles, "Spectral backscattering properties of marine phytoplankton cultures," Optics Express **18**, 15073-15093 (2010).

35. X. Zhang, and D. J. Gray, "Backscattering by very small particles in coastal waters," Journal of Geophysical Research: Oceans **120**, 6914-6926 (2015).

36. M. Chami, E. B. Shybanov, G. A. Khomenko, M. E.-G. Lee, O. V. Martynov, and G. K. Korotaev, "Spectral variation of the volume scattering function measured over the full range of scattering angles in a coastal environment," Applied optics **45**, 3605-3619 (2006).

37. E. Boss, W. Pegau, M. Lee, M. Twardowski, E. Shybanov, G. Korotaev, and F. Baratange, "Particulate backscattering ratio at LEO 15 and its use to study particle composition and distribution," Journal of Geophysical Research: Oceans **109** (2004).

38. A. Morel, and S. Maritorena, "Bio‐optical properties of oceanic waters: A reappraisal," Journal of Geophysical Research: Oceans **106**, 7163-7180 (2001).

39. A. L. Whitmire, E. Boss, T. Cowles, and W. S. Pegau, "Spectral variability of the particulate backscattering ratio," Optics Express **15**, 7019-7031 (2007).

40. A. Morel, and L. Prieur, "Analysis of variations in ocean color 1," Limnology and oceanography **22**, 709-722 (1977).

41. A. J. Irwin, Z. V. Finkel, O. M. Schofield, and P. G. Falkowski, "Scaling-up from nutrient physiology to the size-structure of phytoplankton communities," Journal of plankton research **28**, 459-471 (2006).

42. Y. Huot, A. Morel, M. Twardowski, D. Stramski, and R. Reynolds, "Particle optical backscattering along a chlorophyll gradient in the upper layer of the eastern South Pacific Ocean," Biogeosciences Discussions **4**, 4571-4604 (2007).

43. O. Ulloa, S. Sathyendranath, and T. Platt, "Effect of the particle-size distribution on the backscattering ratio in seawater," Applied Optics **33**, 7070-7077 (1994).

44. E. Aas, "Refractive index of phytoplankton derived from its metabolite composition," Journal of Plankton Research **18**, 2223-2249 (1996).

45. M. G. Allan, D. P. Hamilton, B. J. Hicks, and L. Brabyn, "Landsat remote sensing of chlorophyll a concentrations in central North Island lakes of New Zealand," International Journal of Remote Sensing **32**, 2037-2055 (2011).

46. T. S. Kostadinov, D. A. Siegel, S. Maritorena, and N. Guillocheau, "Optical assessment of particle size and composition in the Santa Barbara Channel, California," Applied optics **51**, 3171-3189 (2012).

47. X. Zhang, D. J. Gray, Y. Huot, Y. You, and L. Bi, "Comparison of optically derived particle size distributions: scattering over the full angular range

versus diffraction at near forward angles," Applied optics **51**, 5085-5099 (2012).

48. Q. Vanhellemont, and K. Ruddick, "Turbid wakes associated with offshore wind turbines observed with Landsat 8," Remote Sensing of Environment **145**, 105-115 (2014).

49. Z. Lee, "Reports of the International Ocean-Colour Coordinating Group," (2006).

50. C. Barnes, X. Irigoien, J. A. De Oliveira, D. Maxwell, and S. Jennings, "Predicting marine phytoplankton community size structure from empirical relationships with remotely sensed variables," Journal of Plankton Research **33**, 13-24 (2010).

51. T. Kostadinov, D. Siegel, and S. Maritorena, "Retrieval of the particle size distribution from satellite ocean color observations," Journal of Geophysical Research: Oceans **114** (2009).

52. B. B. Barnes, C. Hu, J. P. Cannizzaro, S. E. Craig, P. Hallock, D. L. Jones, J. C. Lehrter, N. Melo, B. A. Schaeffer, and R. Zepp, "Estimation of diffuse attenuation of ultraviolet light in optically shallow Florida Keys waters from MODIS measurements," Remote Sensing of Environment **140**, 519-532 (2014).

53. F. Cao, C. G. Fichot, S. B. Hooker, and W. L. Miller, "Improved algorithms for accurate retrieval of UV/visible diffuse attenuation coefficients in optically complex, inshore waters," Remote Sensing of Environment **144**, 11-27 (2014).

54. C. G. Fichot, S. Sathyendranath, and W. L. Miller, "SeaUV and SeaUV C: Algorithms for the retrieval of UV/Visible diffuse attenuation coefficients from ocean color," Remote Sensing of Environment **112**, 1584-1602 (2008).

55. Z. P. Lee, M. Darecki, K. L. Carder, C. O. Davis, D. Stramski, and W. J. Rhea, "Diffuse attenuation coefficient of downwelling irradiance: An evaluation of remote sensing methods," Journal of Geophysical Research: Oceans **110** (2005).

# Chapter 3: Comparison of different ac-s scattering correction approaches for improving optical closure in a dynamic coastal marine ecosystem

Jesse Bausell & Dr. Raphael Kudela

## Abstract

WET Labs absorption attenuation meter (ac-s) and HOBI Labs HydroScat-6 spectral backscattering sensor (HS6) are widely used by the ocean optics community to measure spectral absorption ($a(\lambda)$), attenuation ($c(\lambda)$), and particulate backscattering ($b_{bp}(\lambda)$) in-situ. An effective method of evaluating the accuracy of these instruments is to use their measurements to model light fields, or apparent optical properties (AOPs) according to radiative transfer theory. Evaluating optical closure, or the similarity of these modeled AOPs to in-situ AOPs measured contemporaneously at the same location, provides insight as to the cumulative accuracy of ac-s and HS6. Deployed in Monterey Bay, however, these instruments consistently fail to achieve optical closure with in-water optical profilers in the green; above-water AOPs modeled through radiative transfer theory underestimate those AOPs measured in-situ. To ascertain the cause of this lack of optical closure, we apply seven different scattering approaches (SCA) to ac-s measurements collected at five biologically and optically distinct sampling stations inside of Monterey Bay. At each station we modeled normalized water-leaving radiance ($[L_W(\lambda)]_N$) for each SCA using Hydrolight, software that models AOPs according to radiative transfer theory. We then compared them to $[L_W(\lambda)]_N$ measured with the Compact Optical Profiling System (C-OPS), a multi-spectral in-water optical profiler. Optical closure across our

five stations was best achieved with SCAs, that assume negligible absorption in the near infrared, as well as an iterative SCA that adjusts ac-s scattering using $b_{bp}(\lambda)$. These SCAs improved optical closure, especially in green maxima, reducing absolute percent differences (APD) between modeled and C-OPS measured $[L_W(\lambda)]_N$ to $\leq$ 5%. Our findings indicate that unaccounted scatter inside ac-s flow tubes explain previous failures to achieve optical closure in the green within Monterey Bay. They also point to the potential of modeling hyperspectral $[L_W(\lambda)]_N$ as a means to reliably characterize coastal ecosystems.

## 1. Introduction

Ocean color satellite and airborne sensors rely on algorithms to estimate optically active biogeochemical constituents from radiometric measurements taken above water. These algorithms are predicated on radiative transfer theory [1], namely the selective absorption ($a$) and scatter ($b$) of light by biological and chemical constituents at different wavelengths ($\lambda$). Also known as inherent optical properties (IOPs), $a$ and $b$ impact watermass light fields, or apparent optical properties (AOPs) [2-6]. In turn, these AOPs are measured by satellites and airborne sensors [7]. Algorithm development and validation thus assume that above-water AOPs are a product of the IOPs exhibited by their watermasses [8]. Software packages, such as Hydrolight, can test this assumption by modeling AOPs from in-situ IOPs according to radiative transfer theory (e.g., [5, 9]). In conjunction with IOPs measured in-situ, these modeled AOPs are advantageous for algorithm validation in that they are not

subject to the potential measurement errors associated with in-situ AOPs. However, Hydrolight-modeled AOPs are only as reliable as the in-situ IOPs, off of which they are based, underscoring the importance of measuring in-situ IOPs accurately and reliably (e.g. [10-12]).

Optical instrumentation is subject to error of varying degrees. This error can be systematic, typically the result of environmental factors such as temperature and salinity (e.g. [13]), or random, resulting from stochastic drift of optical sensors (e.g. [14]). Systematic errors caused by the environment can usually be corrected through the application of instrument-specific correction factors, while random errors can be mitigated with periodic instrument calibrations [13, 14]. Systematic errors caused by instrument design flaws, however, are much more difficult to correct [15, 16]. These errors can be associated with an instrument's platform (e.g. size, shape, and rate of descent), its sensors (e.g. signal to noise, spectral resolution, and optical path length), or its analog (e.g. ADC) [9, 15, 16]. Moreover, suitability of optical instrumentation can vary across ecosystems. Instruments well suited for sampling the open ocean, for example, may be less reliable in coastal or inland ecosystems that are characterized by elevated concentrations of bio-optical constituents such as phytoplankton, suspended sediments (detrital and non-mineral), and colored dissolved organic material (CDOM) [17].

WET Labs absorption attenuation meter (ac-s) and HOBI Labs HydroScat-6 spectral backscattering sensor (HS6) are widely utilized by the ocean optics community. The ac-s measures spectral absorption ($a(\lambda)$) and attenuation ($c(\lambda)$), while HS6 measures spectral backscattering coefficients, from which particulate backscattering ($b_{bp}(\lambda)$) can be computed (e.g., [8, 18]). Originally intended for the open ocean, both ac-s and HS6 have design shortcomings that impact their ability to sample coastal ecosystems. The ac-s measures $a(\lambda)$ and $c(\lambda)$ at 87-89 channels, centered on $\lambda$'s < 4 nm apart, in separate flow tubes. In the attenuation or *c*-tube, a beam of light is focused from one end of the tube into a 1 mm aperture; $c(\lambda)$ is computed as the difference in beam strength from its source and the aforementioned *c*-tube aperture. In the $a$-tube, a light beam is focused at a 45° angle out of phase with the beam inside the $c$-tube. Rather than a 1 mm aperture, the opposite end of the cylindrical $a$-tube is covered with a detector that collects non-absorbed photons. The walls of the $a$-tube are highly reflective as to direct scattered photons into the detector [19, 20]. WET Labs produces two ac-s models with different optical pathlengths, or distances that light beams travel through the medium they charcterize (e.g. length of flow tubes): 25 cm and 10 cm, designed for open ocean and coastal habitats respectively (Fig. 1). The 25 cm long ac-s optical pathlenth, however, causes measurement contamination from unaccounted scattering, especially in coastal habitats. In the $c$-tube, forward-scattered photons are re-deflected into the 1 mm aperture, causing underestimations in $c(\lambda)$. Conversely, ac-s overestimates $a(\lambda)$, as the reflective walls of the $a$-tube do not redirect all scattered photons into the detector [19]. Because of these directional

measurement contaminations, a scattering correction approach (SCA) is necessary to correct ac-s measurements for aforementioned unaccounted scatter inside the flow tubes. Measuring volume scattering function (VSF) at a single scattering angle, 140°, HS6 uses Oishi's [21] proportionality argument to derive $b_{bp}(\lambda)$ for six $\lambda$'s [15]. Proposed for the open ocean, Oishi's [21] assumption of a $\lambda$-independent conversion factor is potentially problematic in phytoplankton-dominated ecosystems where this conversion factor could be $\lambda$-dependent [22]. Moreover, HS6's long optical pathlength of 15 cm is also susceptible to contamination, this time from $a$ and $b$, which must be accounted for in what is known as a *sigma* correction [15, 23].

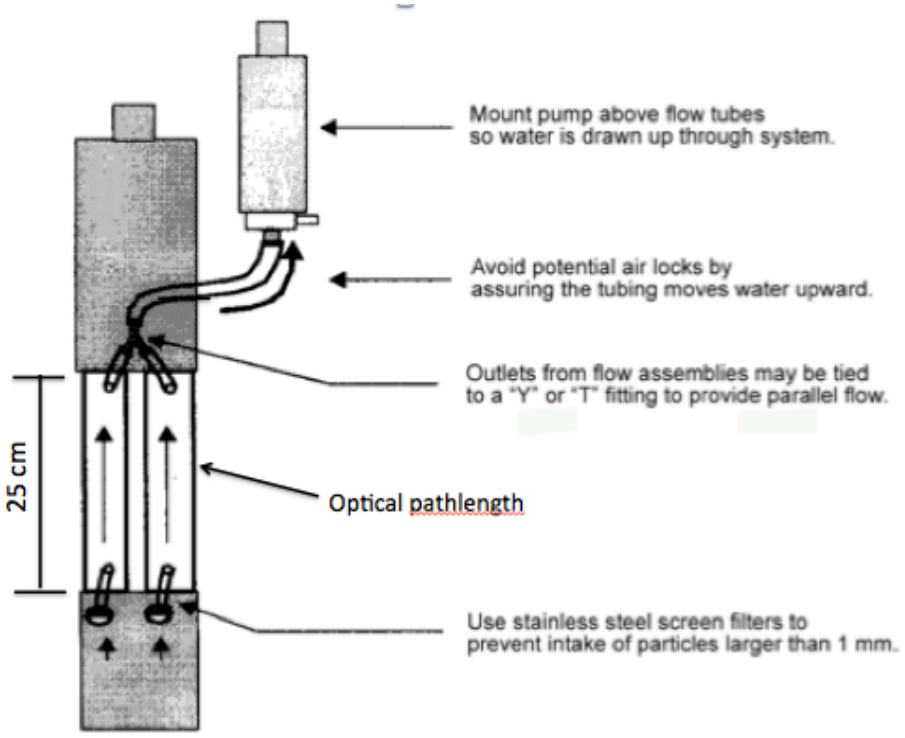



**Figure 1.** Diagram of WET Labs ac-s. 25 cm optical pathlength, or the distance between the beam origin and photon detectors, is indicated next to flow tubes (shown in white). Diagram from [20]

Accuracy and reliability of in-situ IOPs in characterizing particular ecosystems can be ascertained based on their ability to achieve optical closure. Optical closure is achieved when modeled AOPs, computed from in-situ IOPs using radiative transfer theory (e.g. Hydrolight), are similar to in-situ AOPs, contemporaneously measured from the same location. Comparing measured and modeled AOPs can help investigators determine whether in-situ IOPs, such as ac-s and HS6 measurements, accurately characterize a particular watermass. Using this approach to compare the utility of different phase functions in characterizing a Monterey Bay red tide event, Tuchow et al. [5] demonstrated that when using Doxaran et al.'s [23] proposed sigma correction method, HS6 achieved the highest degree of optical closure in terms of its similarity to above-water AOPs that were measured using HyperPro II (HP2), a commercially available in-water optical profiler manufactured by Satlantic. Thus Tuchow et al. [5] suggest that ECO-VSF3's ability to measure three scattering angles (as opposed to one) but only three $\lambda$'s is not a worthwhile tradeoff for watermasses with high phytoplankton biomass, as Doxaran et al.'s [23] sigma correction can eliminate $a$ and $b$ errors associated with HS6's 15 cm optical pathlength. While Doxaran-corrected HS6 measurements achieved the best optical closure overall in terms of similarity to HP2, they significantly underestimated above-water AOPs in the green [5].

As Doxaran et al. [23] can mitigate errors associated with HS6's long optical pathlength, WET Labs's 10 cm optical pathlength ac-s is designed to minimize unaccounted scattering inside ac-s flow tubes. However, because prohibitive costs commonly preclude the acquisition of a second ac-s, many investigators commonly sample coastal waters with 25 cm pathlength ac-s. These prohibitive costs underscore the necessity of SCAs in correcting ac-s measurements, despite the availability of a model better suited for coastal habitats. Indeed Tuchow et al. [5] relied upon a 25 cm optical pathlength ac-s in its modeling of above-water AOPs. Unaccounted scatter inside ac-s flow tubes could therefore explain Tuchow et al.'s [5] underestimation of modeled above-water AOPs in the green.

Tuchow et al.'s [5] findings are predicated on the assumption that HP2 measured the red tide accurately. However, Bausell et al. [9] suggest that HP2's low signal to noise ratio can introduce uncertainty into $[L_W(\lambda)]_N$. Nevertheless, Bausell et al. [9] report the similar above-water AOP discrepancies in the green between Hydrolight and C-OPS as Tuchow et al. [5] report for Hydrolight and HP2. Both studies modeled above-water AOPs using IOPs measured in-situ using ac-s and HS6. In the context of the elimination of HS6 pathlength errors by Doxaran et al. [23] and the reliability of C-OPS in coastal ecosystems, we believe that the underestimation of modeled above-water AOPs in the green may stem from failure of Bausell et al. [9] and Tuchow et al. [5] to properly correct unaccounted scatter inside 25 cm ac-s flow tubes. As such, a variety of SCAs have been proposed for ac-s that are subject to different underlying

assumptions (e.g. [16, 19, 24, 25]). Here we re-evaluate five optically biologically distinct stations that were originally analyzed in Bausell et al. [9], by using different SCAs with the intent of improving optical closure with C-OPS.

## 2. Methods

*2.1. Scattering Correction Approaches*

NASA Ocean Optics Protocols detail several SCAs for long-pathlength absorption and attenuation meters, such as ac-s and its predecessor, ac9 [26]. In this text we refer to these as 'self-contained' SCAs because they do not require any additional measurements aside from ac-s. These self-contained SCAs can be broken down into two categories: 'flat' and 'proportional'.

Flat SCAs assume that unaccounted scatter is $\lambda$-independent and can be characterized by $a$ measured in the NIR, commonly at $\lambda = 715$ nm (e.g. [16, 25]), that is then subtracted from the entire spectrum. Flat SCAs can be characterized as

$$a_n(\lambda) = a_m(\lambda) - (a_m(715) - a(715)) \quad (1)$$

where $a_m(\lambda)$ is ac-s measured spectral absorption prior to correcting for scatter, $a_m(715)$ and $a(715)$ are ac-s measured and *actual* absorption at $\lambda = 715$ nm, and $a_n(\lambda)$ is scatter-corrected spectral absorption. The most basic flat SCA, which assumes negligible $a$ in the NIR (e.g., $a(715) = 0$), uses $a_m(715)$ as a proxy for unaccounted scatter [25]. However, because $a(715)$ can be non-negligible as well

(e.g., [16]), flat SCAs can also assume non-negligible $a$ in the NIR by setting $a(715)$ equal to a constant fraction of $a_m(715)$ or estimating it empirically [16, 26].

Devised by Zeneveld et al. [25], proportional SCAs assume that unaccounted $a$-tube scatter inside is $\lambda$-dependent, which they quantify as a ratio of $a_m$ in the NIR (e.g., $a_m(715)$) . This ratio is defined as spectral scatter ($b(\lambda)$) over scatter in the NIR, typically set to $\lambda = 715$ nm. Proportional SCAs can be summarized as

$$a_n(\lambda) = a_m(\lambda) - (a_m(715) - a(715))\frac{\epsilon_c c_m(\lambda) - a_m(\lambda)}{\epsilon_c c_m(715) - a_m(715)} \quad (2)$$

where $c_m$ denotes $c$ measured by ac-s and $\epsilon_c$ denotes a $\lambda$-independent correction coefficient intended to account the underestimation of $c_m$ in the $c$-tube [16]. Similar to flat SCAs, proportional SCAs can be operated under the assumption of negligible and non-negligible $a(715)$.

While self-contained SCAs are advantageous in that they require no additional measurements to correct for unaccounted scatter, they only correct $a_m(\lambda)$. Iterative approaches on the other hand, such as McKee et al. [19, 24] correct scattering errors associated with both ac-s tubes. They utilize Monte Carlo simulations to ascertain the relationship between particulate backscattering ratio ($\tilde{b}_b(\lambda)$) (see below) and unaccounted scatter in ac-s tubes.

$$\tilde{b}_b(\lambda) = \frac{b_{bp}(\lambda)}{b(\lambda)} \quad (3)$$

McKee et al. [19, 24] offer promise in that they do not require ecosystem-specific assumptions, such as negligible vs. non-negligible $a$ in the NIR or $\lambda$ -dependent VSF. They do, however, require contemporaneously measured $b_{bp}(\lambda)$. This prerequisite for contemporaneous $b_{bp}(\lambda)$ limits the scope of application of these SCAs, especially in the context of historical datasets.

We compared utility of seven SCAs in achieving optical closure: two flat, three proportional, and two iterative. The flat SCAs with which we processed $a_m(\lambda)$ assumed that $a(715)$ was both negligible ($FL^0$) and non negligible ($FL$). Similar to flat SCAs, the proportional SCAs with which we processed $a_m(\lambda)$ assumed $a(715)$ was negligible ($PR^0$) and non-negligible ($PR$) as well. We also processed $a_m(\lambda)$ with a proportional SCA that assumed non-negligible $a(715)$ and $\epsilon_c = 1.79$ as proposed by Rottgers et al. [16] ($PR_C$). For self-contained SCAs that assume non-negligible $a$ in the NIR, we estimated $a(715)$ using an empirical relationship also established by Rottgers et al. [16]:

$$a(715) = 0.212\, a_m(715)^{1.135} \quad (4)$$

Finally, we processed $a_m(\lambda)$ using the iterative methods proposed by McKee et al. [19] ($Mc_{08}$), and updated by McKee et al. [24] ($Mc_{13}$). $Mc_{13}$ builds onto $Mc_{08}$ by quantifying degradation of ac-s' highly reflective $a$-tube walls that is likely to occur over time with continued usage. It takes into account the fractional reflectance efficiency of these walls ($r_W$) by modeling unaccounted scatter for ten values of $r_W$ ranging from 0.95 and 1, with $r_W = 1$ denoting fully reflective $a$-tube walls. Because

we cannot determine the $r_W$ of our ac-s $a$-tube, we computed $a_n(\lambda)$ for all ten $r_W$ values, modeled $[L_W(\lambda)]_N$ for each $r_W$ using Hydrolight, and then constrained $r_W$ using $[L_W(\lambda)]_N$ measured by C-OPS (*Section 2.2*). SCAs and their characteristics are summarized in Table 1.

**Table 1. Scattering correction approaches**

| SCA | $a(715)$ | $\epsilon_c$ | $a_n(\lambda)$ | $c_n(\lambda)$ | Sigma-Correction: $b_{bp}(\lambda)$ | Notes |
|---|---|---|---|---|---|---|
| $FL^0$ | 0 | --- | $Eq.1$ | $c_m(\lambda)$ | $a_n(\lambda)$[a] | Flat approach with negligible $a(715)$ |
| $FL$ | $Eq.4$ | --- | $Eq.1$ | $c_m(\lambda)$ | $a_n(\lambda)$ | Flat approach with non-negligible $a(715)$ |
| $PR^0$ | 0 | 1 | $Eq.2$ | $c_m(\lambda)$ | $a_n(\lambda)$ | Proportional approach with negligible $a(715)$ |
| $PR$ | $Eq.4$ | 1 | $Eq.2$ | $c_m(\lambda)$ | $a_n(\lambda)$ | Proportional approach with non-negligible $a(715)$ |
| $PR_C$ | $Eq.4$ | 1.79 | $Eq.2$ | $c_m(\lambda)$ | $a_n(\lambda)$ | Proportional approach with non-negligible $a(715)$. Corrects $c(\lambda)$, but only for $a_n(\lambda)$. |
| $Mc_{08}$ | --- | --- | Iterations | Iterations | $a_{CDOM}(\lambda) + a_P(\lambda)$[b] | McKee et al. [19]: Computes $a_n(\lambda)$ & $c_n(\lambda)$ using $b_{bp}(\lambda)$. |
| $Mc_{13}$ | --- | --- | Iterations | Iterations | $a_{CDOM}(\lambda) + a_P(\lambda)$ | McKee et al. [24]: Computes $a_n(\lambda)$ & $c_n(\lambda)$ using $b_{bp}(\lambda)$. |

[a] $a_n(\lambda)$ from specified SNA used to sigma-correct $b_{bp}(\lambda)$

[b] $a_{CDOM}(\lambda)$ & $a_P(\lambda)$ from water samples (see Section 2.2) used to sigma-correct $b_{bp}(\lambda)$

*2.2 Data Acquisition and Processing*

Our five sampling stations, CST17, CST18, OCE18, CHR1, and CHR2 were sampled as part of three NASA airborne campaigns: COAST (CST), OCEANA (OCE), and C-HARRIER (CHR). Data collection and processing standards were therefore consistent with NASA Ocean Optics Protocols [26]. Reported in Bausell et al. [9], the C-OPS was deployed by gently lowering the profiler off the side of the *R/V John Martin* and kiting it away from the vessel using its telemetry cable. Once in position, a cast was initiated by popping the irradiance sensor above the sea surface and then allowing it to free fall. Following best practices as described in [14], we completed three to four separate casts at each station, which were processed into $[L_W(\lambda)]_N$ (see [9]). The HP2 was deployed (consecutively) using these same protocols.

At each station, seawater was collected at the sea surface using a bucket after pre-rinsing it three times with ambient seawater. From these water samples we measured chlorophyll concentration (Chl), as well as particulate ($a_P(\lambda)$), and CDOM ($a_{CDOM}(\lambda)$) $a$ components. As reported in Bausell et al. [9], Chl was measured using methods outlined in Kudela et al. [27]. Three 250 $mL$ aliquots of sea water were filtered on Whatman Glass Fiber Filter (GF/F; nominally 0.7 $\mu m$) under low vacuum, stored on dry ice, later extracted following the non-acidification technique (see [28]), and measured with a Turner Designs 10 AU fluorometer. Our fluorometer was calibrated using a Turner Designs chlorophyll standard, which was verified using a spectrophotometric method (see [29]). Following procedures outlined in Kudela et al.

[30], $a_P(\lambda)$ was measured by first filtering seawater onto a GF/F under low vacuum until the filter changed color. GF/F was then placed in a cryovial and stored in liquid nitrogen and later measured using a Varian Cary® UV-Vis Spectrophotometer. $a_P(\lambda)$ was calibrated using blank GF/F and standardized for volume of filtered seawater. To measure $a_{CDOM}(\lambda)$, seawater was first forced through a 0.2 $\mu m$ filter to remove any particulate matter, collected in a 50 $mL$ centrifuge tube, and stored on ice pending analysis. Filtrate was placed in a 10 $cm$ quartz cuvette and measured using a Varian Cary® UV-Vis Spectrophotometer that was calibrated with MilliQ® water (see [6]). We tabulated spectrophotometric surface absorption (henceforth referred to as $a(\lambda)$) as

$$a(\lambda) = a_P(\lambda) + a_{CDOM}(\lambda) \tag{5}$$

Although Chl measurements are available for all five stations, reliable $a_P(\lambda)$ and $a_{CDOM}(\lambda)$ (and hence $a(\lambda)$) are unavailable for CHR stations.

Affixed to a metal cage with an integrated SeaBird sonde, ac-s and HS6 were then simultaneously lowered and raised through the water column multiple times in succession at each station. Because they are partitioned onto two holographic gratings, based on the side of the spectrum on which they are centered, ac-s' channels sample asynchronously. This asynchronous sampling inside $a$ and $c$-tubes commonly causes artificial offsets or 'jumps' occurring mid-spectrum (~553-557 nm) in raw ac-s measurements. We corrected these jumps by first linearly interpolating $a$ and $c$ for

the channel in the second holographic grating (upper spectrum) centered at lowest $\lambda$, using the three channels in the first grating with the highest $\lambda$'s. We then calculated an offset by subtracting these interpolated $a$ and $c$ values from measured $a$ and $c$ values, and finally, we subtracted these offsets from the upper halves of their respective spectra. Raw ac-s measurements were then preprocessed into $a_m(\lambda)$ and $c_m(\lambda)$ by discarding up-casts, applying pure-water calibration corrections, and correcting for directional biases associated with temperature and salinity (see [9]). We then processed $a_m(\lambda)$ according to each of the seven SCAs (see Table 1). Self-contained SCAs were applied to $a_m(\lambda)$ and the resulting $a_n(\lambda)$ underwent quality assurance and quality control (QA/QC) prior to averaging $a_n(\lambda)$ and $c_n(\lambda)$ into 0.5 m depth bins. This QA/QC protocol entailed discarding individual $a_n(\lambda)$ and their corresponding $c_n(\lambda)$ if either spectrum contained a negative value or if $a > c$ at any point in the visible ($\lambda < 700$ nm). After first subtracting pure-water backscattering coefficients approximated by Morel et al. [31], we proceeded to produce five sets of Doxaran et al. [23] sigma-corrected $b_{bp}(\lambda)$, one for each self-contained SCA. While performing each sigma-correction, individual $b_{bp}(\lambda)$ were corrected using the binned $a_n(\lambda)$ corresponding to their depth. These sigma-corrected $b_{bp}(\lambda)$'s were then depth-binned (0.5 m) and input into Hydrolight 5.3 along with similarly binned $a_n(\lambda)$ and $c_n(\lambda)$, as well as Chl for characterizing red fluorescence. Settings are outlined in Table 2. We disclose that although $PR$ was applied to ac-s data in Bausell et al. [9], we re-processed $a_n(\lambda)$ using $PR$ in order to ensure consistency between SCAs.

Because their application requires fully processed $b_{bp}(\lambda)$, we could not sigma-correct $b_{bp}(\lambda)$ with $a_n(\lambda)$ processed with $Mc_{08}$ and $Mc_{13}$without falling into a circular logic trap. We circumvented this dilemma for CST17, CST18, and OCE18 by sigma correcting $b_{bp}(\lambda)$ with $a(\lambda)$ (assumed to be constant with depth) prior to applying $Mc_{08}$ and $Mc_{13}$. Due to computational limitations, $a_m(\lambda)$ and $c_m(\lambda)$ were depth-binned before $Mc_{08}$ and $Mc_{13}$ were applied. As before, each set of binned $a_n(\lambda)$, $c_n(\lambda)$, and $b_{bp}(\lambda)$, along with Chl, were input into Hydrolight 5.3 (Table 2). CHR1 and CHR2 were processed using the same basic procedures, albeit sigma-correcting $b_{bp}(\lambda)$ with $a_m(\lambda)$ prior to applying $Mc_{08}$ and $Mc_{13}$ SCAs.

**Table 2. Hydrolight 5.3 Settings**

| Parameter | Setting | Input Source | Notes |
|---|---|---|---|
| $a(\lambda)$&$c(\lambda)$ | User-input $a(\lambda)$&$c(\lambda)$ | Depth-binned ac-s data file | Averaged. 0.5 m depth-bins |
| Phase Function | Fournier-Forand subroutine w/ user-input $b_{bp}(\lambda)/b(\lambda)$[a] | Depth-binned HS6 data file | Bootstrapped for each run |
| Inelastic Scatter | Chl Fluorescence (No Raman Scatter) | Surface Chl (GF/F) | Averaged. 0.5 m depth-bins |
| $T$ & $S$ | User-input | Seabird SeaCAT CTD | Constant w/ depth |
| Sky Model#1 | RADTRAN-X subroutine w/ user-input irradiance | HP2 solar reference sensor | Partitions into direct & diffuse irradiances |
| Sky Model#2 | HCNRAD subroutine | Date/GMT/ LAT/LON of station | Computes sky radiance from solar angle & irradiances |
| ATM[b] | Air Pressure/ Humidity/wind speed | WeatherHawk wind meter | Measured at Santa Cruz Wharf |
| Output $\lambda$ | Range: 400-715 nm Resolution: 3 nm | --- | --- |
| Output Depth | Range: 0-16 m Resolution: 0.5 m | --- | --- |
| Bottom Boundary | Infinite | --- | IOPs constant below 16 m |

[a] $b(\lambda) = c(\lambda) - a(\lambda)$
[b] Atmospheric/Meteorological Parameters

*2.3 Data Analysis*

Despite modeling hyperspectral $[L_W(\lambda)]_N$ (Table 2), we limited our optical closure evaluations to the λ's between 400-715 nm on which C-OPS channels were centered (see Figs. 1 & 2). At each station we first calculated root mean squared error (RMSE) between C-OPS $[L_W(\lambda)]_N$ and that of each SCA; then we ranked our seven SCAs according to lowest RMSE (Table 3). Although we modeled $[L_W(\lambda)]_N$ for $Mc_{13}$ ten times per station (once for each $r_W$ value), we constrained these outputs by selecting only the $r_W$ with the lowest RMSE relative to C-OPS. We then evaluated optical closures of three SCAs at each station: the self-contained SCA with the lowest RMSE (station dependent), the iterative SCA with the lowest RMSE, and $PR$, which was used by Bausell et al. [9] to model $[L_W(\lambda)]_N$.

We evaluated optical closure of the three aforementioned SCAs qualitatively and quantitatively within each station. An SCA achieved qualitative optical closure for a given λ if modeled $[L_W(\lambda)]_N$ fell within one standard deviation of (mean) C-OPS $[L_W(\lambda)]_N$. We evaluated quantitative optical closure by computing absolute percent difference (APD) between SCA modeled and C-OPS $[L_W(\lambda)]_N$. Although we do not provide a definitive cutoff for quantitative optical closure, we refer to Mueller et al.'s [32] classification of data as being of calibration quality (APD < 5%), validation quality (APD < 10%), and research quality (APD < 25%). We made qualitative and quantitative comparisons between C-OPS and mean $[L_W(\lambda)]_N$, as measured by HP2, to ascertain whether radiative transfer modeling improves accuracy of hyperspectral

$[L_W(\lambda)]_N$ relative to HP2. To provide additional context for our findings, we compared SCAs with HP2 in order to determine whether theoretical radiative transfer modeling improves $[L_W(\lambda)]_N$ relative to HP2. To provide additional context for our findings, we plot surface $a(\lambda)$ with $a_n(\lambda)$ at 0.75 m median depth-bin (0.5-1 m), or near-surface $a_n(\lambda)$ for stations at which the former is available. We selected this depth bin due to ac-s' inability to reliably measure the upper 0.5 m of the water column.

## 3. Results

According to RMSE, $Mc_{13}$, as well as $PR^0$ or $FL^0$ (depending on which station) were the most optimal SCAs for achieving optical closure across our five stations. $PR^0$ and $FL^0$, the two SCAs that assumed negligible $a$ in the NIR were the most optimal of the self-contained SCAs. One of these two SCAs exhibited either the lowest or second lowest RMSE at each station (Table 3). $Mc_{13}$ also performed well at four stations; it exhibited the lowest RMSE at CST18 and CHR2, the second lowest RMSE at CST17, and the third lowest RMSE at OCE18 (behind $PR^0$ and $FL^0$). In applying $Mc_{13}$ $r_W$ was constrained to different values at each station (Fig. 2).

**Table 3. RMSE of SCAs by Station**

| | CST17 | | OCE18 | | CST18 | | CHR1 | | CHR2 | |
|---|---|---|---|---|---|---|---|---|---|---|
| Rank | SCA | RMSE | SCA | RMSE | SCA | RMSE | SCA | RMSE | SCA | RMSE |
| 1 | $FL^0$ | 3.89e-2 | $PR^0$ | 5.04e-2 | $Mc_{13}$ | 5.90e-2 | $PR^0$ | 4.18e-2 | $Mc_{13}$ | 5.54e-2 |
| 2 | $Mc_{13}$ | 4.42e-2 | $FL^0$ | 5.07e-2 | $FL^0$ | 6.84e-2 | $PR_C$ | 6.24e-2 | $PR^0$ | 6.61e-2 |
| 3 | $PR_C$ | 4.44e-2 | $Mc_{13}$ | 5.54e-2 | $PR^0$ | 9.08e-2 | $FL^0$ | 6.34e-2 | $FL^0$ | 7.07e-2 |
| 4 | $PR$ | 4.49e-2 | $PR_C$ | 6.07e-2 | $FL$ | 8.71e-2 | $Mc_{13}$ | 6.77e-2 | $PR_C$ | 9.07e-2 |
| 5 | $FL$ | 6.09e-2 | $FL$ | 6.22e-2 | $PR$ | 9.87e-2 | $PR$ | 6.92e-2 | $PR$ | 9.63e-2 |
| 6 | $PR^0$ | 6.3e-2 | $PR$ | 6.71e-2 | $PR_C$ | 0.10 | $FL$ | 0.105 | $FL$ | 0.104 |
| 7 | $Mc_{08}$ | 0.167 | $Mc_{08}$ | 0.107 | $Mc_{08}$ | 0.125 | $Mc_{08}$ | 0.175 | $Mc_{08}$ | 0.167 |

Examining qualitative optical closure at CST17, we note that $FL^0$ and $Mc_{13}$ respectively achieve optical closure at ten ($\lambda \leq 625$, $\lambda = 665$ nm) and six ($\lambda = 412$, 490, 555, 560, 625, & 665 nm) of the 13 $\lambda$'s that we compared. $PR$ by contrast achieved optical closure at only four $\lambda$'s ($\lambda = 510$, 532, 665 & 670 nm) (Figs. 1a, 1b, & xa). At OCE18, $PR^0$ achieved qualitative optical closure for nine $\lambda$'s. $Mc_{13}$ achieved optical closure for seven $\lambda$'s; all of which except for $\lambda = 412$ nm overlapped with $FL^0$. Unlike at CST17, $Mc_{13}$ did not achieve optical closure at $\lambda = 555$ & 560 nm, the $\lambda$'s closest to the green maximum. Neither SCA achieved optical closure at $\lambda = 510$, 532, or 710 nm. However, $PR$, which achieved optical closure at 6 $\lambda$'s, did achieve optical closure at $\lambda = 510$ & 532 nm (Figs. 1c, 1d, & xc). At CST18, $Mc_{13}$ achieved qualitative optical closure at $\lambda \leq 670$ nm for all 11 $\lambda$'s (Fig. 2e). $FL^0$ only achieved optical closure for six of these $\lambda$'s $\leq 670$ (Fig. 2d & 3e). $PR$ achieved optical closure for 5 $\lambda$'s (Fig. 2e). Only $Mc_{13}$ achieved optical closure at $\lambda = 555$ & 560 nm at CST18 (Fig. 2f & 3e). $PR^0$ achieved the best qualitative optical

closure at CHR1, overlapping with C-OPS at 8 $\lambda$'s, including those closest to the green maximum. Contrary to our other four stations, $Mc_{13}$ did not improve optical closure relative to $PR$, overlapping with C-OPS at one less $\lambda$ (4 total) (Fig. 2g, 2h, & 3b). CHR2 demonstrated a very different pattern than CHR1. Here, $Mc_{13}$ exhibited the highest qualitative optical closure of the SCAs, overlapping with C-OPS at 8 $\lambda$'s, included $\lambda = 555$, the C-OPS centered $\lambda$ closest to the green maximum. $PR^0$ did improve optical closure relative to $PR$, but like $PR$, also failed to characterize the green maximum at this station in terms its magnitude (Fig. 2j, 2k, & 3d). SCA modeled $[L_W(\lambda)]_N$ exhibited the same spectral shape as HP2 across all stations. However, modeling $[L_W(\lambda)]_N$ with an optimal SCA improved overlap with C-OPS relative HP2 at all stations. With the exception of CHR2, mean HP2 $[L_W(\lambda)]_N$ did not overlap within one standard deviation of C-OPS at any $\lambda < 555$ nm (Fig. 3).

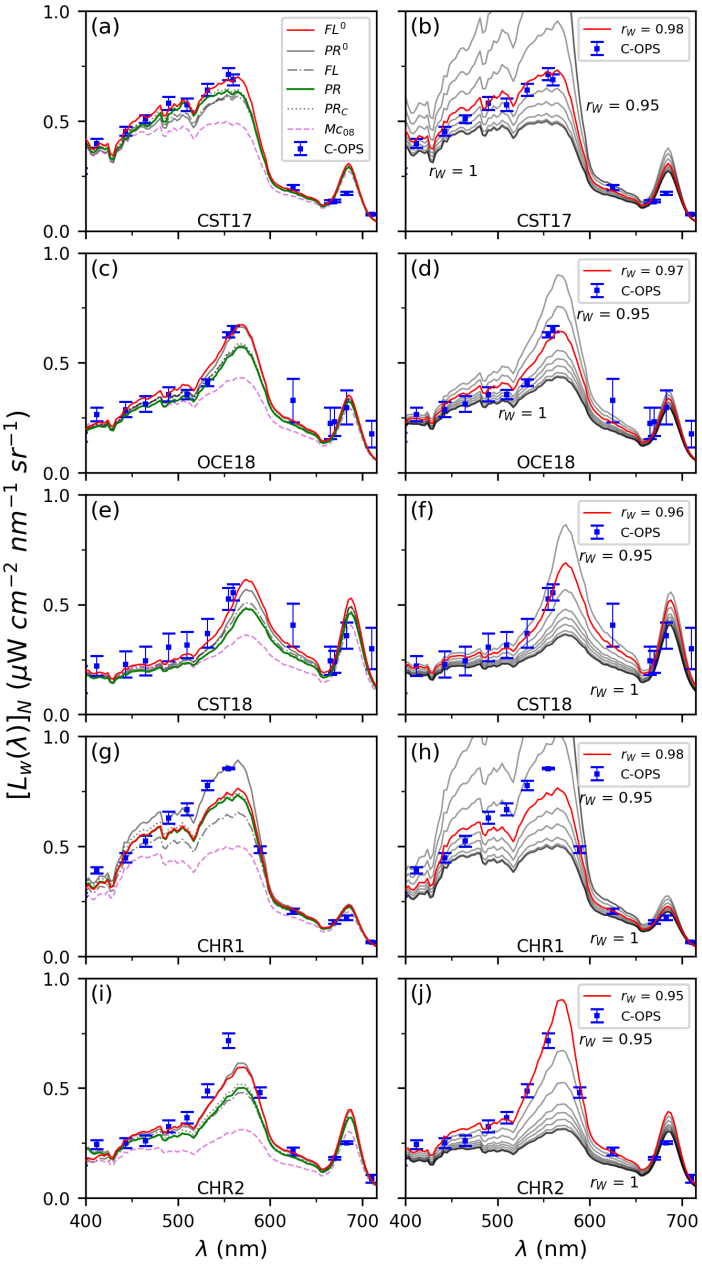



**Figure 2.** $[L_W(\lambda)]_N$ modeled from each SCA overlaid with mean $[L_W(\lambda)]_N$ ($\pm$ standard deviation bars) as measured by C-OPS for each station (rows). Left column contains all SCAs except $Mc_{13}$. Right column contains the ten $[L_W(\lambda)]_N$ modeled from $Mc_{13}$ for each $r_W$. $[L_W(\lambda)]_N$ modeled by $Mc_{13}$with constrained $r_W$ is in red.

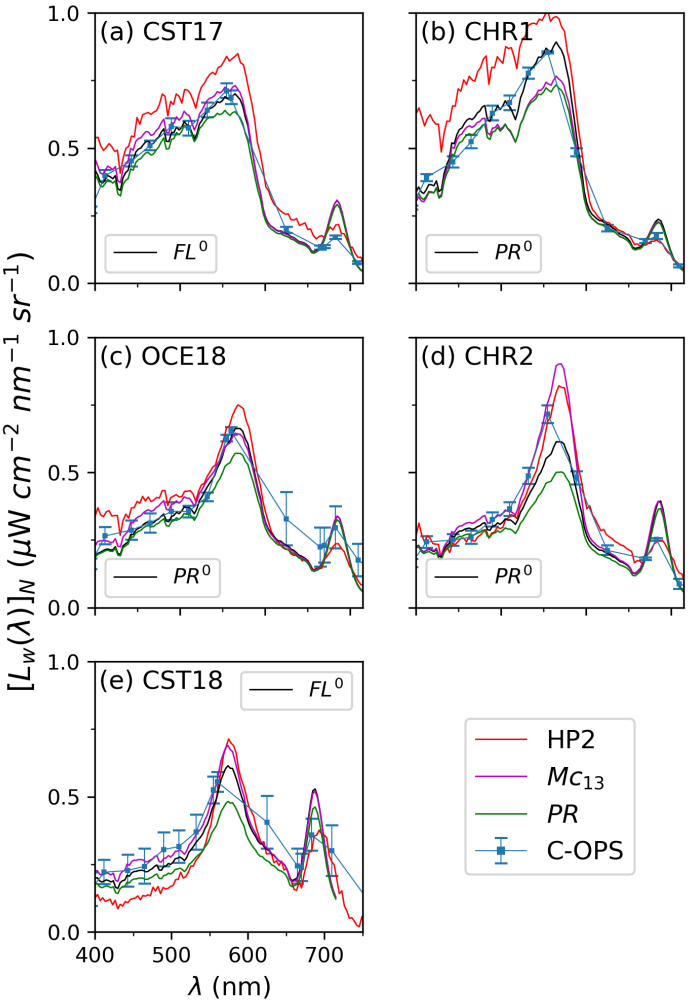



**Figure 3.** SCA-modeled $[L_W(\lambda)]_N$ overlaid with mean $[L_W(\lambda)]_N$ ($\pm$ standard deviation bars) as measured by C-OPS, and mean $[L_W(\lambda)]_N$ as measured by HP2. SCAs were limited to $PR$, $Mc_{13}$, and either $FL^0$ or $PR^0$ (depending on the station).

Quantitative optical closure evaluation revealed that $FL^0$ and $Mc_{13}$ exhibited validation research quality $[L_W(\lambda)]_N$ for ten λ's ($\lambda \leq 670$ nm) at CST17. $FL^0$ demonstrated validation quality at seven of these ten λ's. At $\lambda > 670$ nm, $FL^0$ and $Mc_{13}$ produced research quality $[L_W(\lambda)]_N$ for two of the three remaining λ's ($\lambda = 683$ & 710 nm), while $PR$ $[L_W(\lambda)]_N$ was research quality only for $\lambda = 683$ (Fig. 4a). $FL^0$

had the best quantitative optical closure overall at CST17, as all λ's ≤ 665 nm (except for $\lambda = 625$ nm) exhibited APD < 5%, or calibration quality $[L_W(\lambda)]_N$. We also note that APD < 5% with regard to $Mc_{13}$ for $\lambda = 555$ and 560 nm, the λ's closest to the green maximum (Fig. 4a). At OCE18, $PR^0$ and $Mc_{13}$ $[L_W(\lambda)]_N$'s were of research quality for nine $\lambda$'s ($\lambda \leq 560$, $\lambda = 670$ & 683 nm). $PR$ demonstrated a similar trend, except for $\lambda = 670$. Similar to CST17, $FL^0$ and $Mc_{13}$ exhibited APD < 5% for $\lambda =$ 555 and 560 nm (Fig. 4c). $Mc_{13}$, $FL^0$, and $PR$ exhibited the most pronounced differences in quantitative optical closure at CST18. $Mc_{13}$ yielded the lowest APDs overall, followed by $FL^0$ and $PR$. Of the ten λ's for which $Mc_{13}$ and $FL^0$ exhibited research quality $[L_W(\lambda)]_N$, $Mc_{13}$ $[L_W(\lambda)]_N$ was of validation quality for eight of these λ's (including $\lambda = 555$ and 560 nm). Using $PR$ only four $\lambda$'s were of research quality or better (Fig. 4e). With the exception of $PR^0$ at $\lambda = 683$ nm, $PR^0$, $Mc_{13}$, and $PR$ were of research quality for all C-OPS centered $\lambda$'s at CHR1. However, $PR^0$ was of validation quality for seven $\lambda$'s (calibration quality for $\lambda = 490$, 510, 532, 555, and 670 nm) (Fig. 4b). At CHR2 $PR^0$ and $Mc_{13}$ improve quantitative optical closure relative to $PR$, exhibiting research quality for 11 of 12 $\lambda$'s. $Mc_{13}$ exhibited validation quality for seven of these $\lambda$'s. With the exception of CHR2, APD between C-OPS and HP2 was higher than that of C-OPS and $Mc_{13}$, as well as C-OPS and $PR^0$ (or $FL^0$ depending on the station). This was true for all but a handful of $\lambda$'s, especially true in the blue (4d).

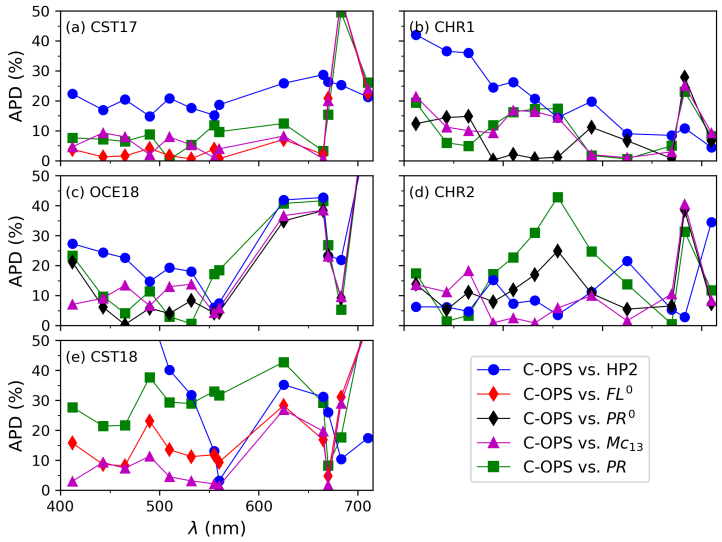



**Figure 4.** Absolute percent differences (APD) of C-OPS vs. $Mc_{13}$, $FL^0$, $PR^0$, and $PR$ at each station calculated for C-OPS centered $\lambda$'s.

In the blue and to a lesser extend the red, near surface (0.5-1 m depth bin) $a_n(\lambda)$ underestimated $a(\lambda)$ at stations for which the later was available. These discrepancies, however, decrease in the green (Fig. 5). At CST17 and CST18, near surface $a_n(\lambda)$ corrected using $FL^0$ and $Mc_{13}$ mirrored $a(\lambda)$ between $\lambda =$ 550-650 nm, a region of low phytoplankton $a$ (Figs. 3a, b, e, & f). However, at OCE18 near surface $FL^0$ and $Mc_{13}$ $a_n(\lambda) < a(\lambda)$ ran parallel to $a(\lambda)$ between 550-650 nm (Figs. 3c & d). With the exception $Mc_{13}$ at OCE18, $PR$-corrected near surface $a_n(\lambda)$ was greater than $Mc_{13}$ and $FL^0$ across the visible at all stations (Fig. 5). Except for $FL^0$ at CST18, there are no discernible differences in near surface $b_{bp}(\lambda)$ sigma-corrected with $a_n(\lambda)$ that were processed using self-contained SCAs (Fig. 6). Due to large differences in magnitude between $a(\lambda)$ and $a_n(\lambda)$ at OCE18 and CST18 (see Fig. 5), near surface $b_{bp}(\lambda)$ sigma-corrected with $a(\lambda)$ were higher than near surface $b_{bp}(\lambda)$

sigma-corrected with $a_n(\lambda)$ for $\lambda \leq 510$ (Fig. 6). By contrasting differences in near surface $a_n(\lambda)$ and $b_{bp}(\lambda)$ with differences in $[L_W(\lambda)]_N$ between SCAs, (including $Mc_{13}$ outputs for different $r_W$), we observed $[L_W(\lambda)]_N$ to be most sensitive to IOP changes in the green, but less sensitive to changes in the blue or the red (Figs. 1 & 3). While we couldn't compare $a_n(\lambda)$ with $a(\lambda)$ at CHR stations, we do note large discrepancies between $Mc_{13}$ and $PR^0$ at both stations, especially in the green, (Figs. 3g, 3h, 3i, & 3j), which are reflected in their $[L_W(\lambda)]_N$ comparisons (Figs. 1 & 2).

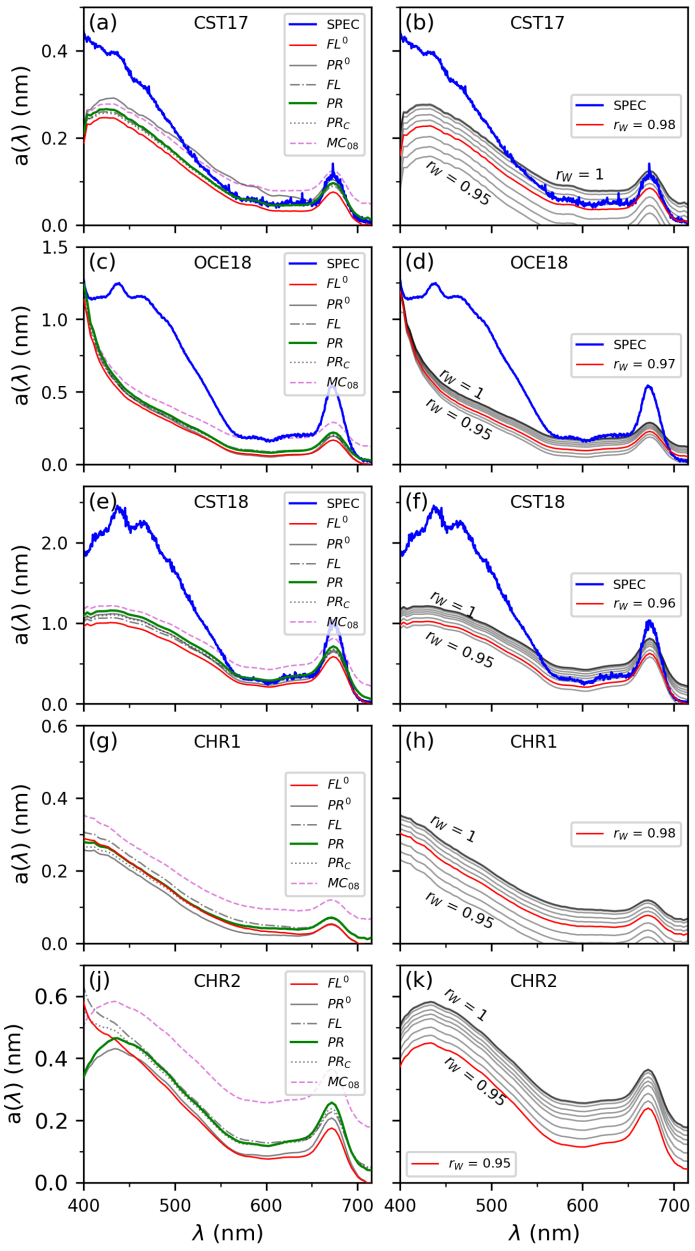



**Figure 5.** Binned near surface $a_n(\lambda)$ processed from each SCA overlaid with spectrophotometer-measured $a(\lambda)$ (*Eq. 4*) for each station (rows). Left column contains all near surface $a_n(\lambda)$'s except $Mc_{13}$. Right column contains the ten near surface $a_n(\lambda)$'s processed for each $r_W$ using $Mc_{13}$. Near surface $a_n(\lambda)$ processed by $Mc_{13}$using constrained $r_W$ is in red. NOTE: spectrophotometer-measured $a(\lambda)$ (SPEC) was unavailable for CHR1 and CHR2.

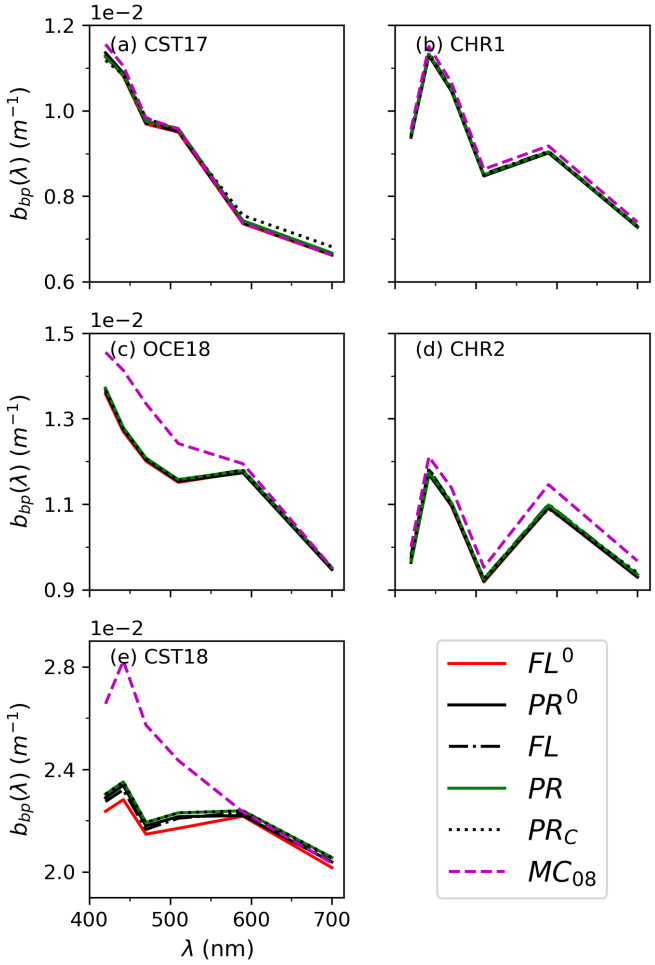



**Figure 6.** Near surface $b_{bp}(\lambda)$ corresponding to different SCAs. With the exception of $Mc_{08}$ and $Mc_{13}$, $b_{bp}(\lambda)$ were sigma-corrected using $a_n(\lambda)$ from their respective SCAs. $Mc_{08}$ and $Mc_{13}$ $b_{bp}(\lambda)$ (labeled $Mc_{08}$) were sigma-corrected using $a(\lambda)$ or $a_m(\lambda)$ depending on the station.

## 4. Discussion

Bausell et al.'s [9] analysis of mean Chl ($\overline{\text{Chl}}$) and mean optical depth at 490 nm ($\overline{\text{OD}}_{490}$) (derived from C-OPS) at the sea surface (see Table 4), indicate differences between phytoplankton biomass and bio-optical properties across our five stations. With their low $\overline{\text{Chl}}$ and high $\overline{\text{OD}}_{490}$ (Table 4), as well as their proximity to Monterey

Bay's M0 buoy, we believe that CST17 and CHR1 represents low-biomass stations. Conversely, CST18's high $\overline{\mathrm{Chl}}$, low $\overline{\mathrm{OD}}_{490}$, and location inside Monterey Bay's 'upwelling shadow', indicate it to be representative of an intense phytoplankton bloom, or a high-biomass station. We believe OCE18 and CHR2, with their intermediate $\overline{\mathrm{Chl}}$ and $\overline{\mathrm{OD}}_{490}$ are characterized phytoplanktons bloom that are less intense than CST18; we consider OCE18 and CHR2 therefore to be medium-biomass stations. Our five stations therefore allowed us to test SCAs under a diverse array of bio-optical properties that are characteristic of Monterey Bay.

**Table 4. Station Sea surface Biomass Descriptors**

| Station | $\overline{\mathrm{Chl}}$ (mg L$^{-1}$) | $\overline{OD}_{490}$ (m) | Location |
|---|---|---|---|
| CST17 | 6.81±0.275 | 3.72±0.43 | M0 |
| CHR1 | 3.13±0.016 | 3.92±0.31 | M0 |
| OCE18 | 12.31±0.01 | 1.89±0.87 | US |
| CHR2 | 17.64±0.35 | 2.04±0.02 | US |
| CST18 | 52.84±0.62 | 0.75±0.12 | US |

Improvements in optical closure brought about by using $PR^0$ or $FL^0$ (station dependent), and $Mc_{13}$ instead of $PR$ (e.g. [9]) suggest that within Monterey Bay, unaccounted ac-s scatter was responsible for the inability of previous studies to achieve optical closure in the green (e.g. [5, 9]). The decreased sensitivity of $[L_W(\lambda)]_N$ to fluctuations of IOPs in the blue and red, with respect to the green explains how optical closure could be achieved in both of these regions despite an inaccurate SCA (Figs. 1, 3, & 5). We attribute our inconsistency in characterizing $[L_W(\lambda)]_N$ in the red and NIR to Hydrolight's use of Chl to compute inelastic scatter (phytoplankton fluorescence). The utility of $FL^0$ or $PR^0$in achieving optical closure

across stations could be due to the fact that $a$ of phytoplankton assemblages in Monterey Bay were negligible in the NIR, as indicated by spectrophotometer-measured $a(715)$ (Figs. 3a, 3b, & 3c). This negligible $a$ may explain why either $FL^0$ or $PR^0$ exhibited the lowest or second lowest RMSE (second to $Mc_{13}$) across our stations regardless of biomass (e.g., Table 4). Also of import, *Eq. 4,* on which $PR$, $PR_C$, and $FL$ are based, was derived from the North Sea, River Elbe, German Bight, and Baltic Sea, as well as laboratory phytoplankton cultures [16]. Therefore, *Eq. 4* may not be relevant to Monterey Bay. By the same token, while $FL^0$ may be optimal for our stations, it might be problematic in coastal and inland ecosystems with significant terrigenous inputs (e.g. River Elbe) or even different Monterey Bay watermasses, as phytoplankton $a$ in the NIR can vary widely [16].

A potential drawback of our protocols, as they relate to self-contained SCAs, is the removal of individual $a_n(\lambda)$ because $a > c$. These removals are potentially problematic because $c_n(\lambda)$ is underestimated in the $c$-tube, meaning that in certain circumstances removed $a_n(\lambda)$ might not be erroneous. Notwithstanding, we employed the aforementioned quality assurance/quality control protocol (*Section 2.2*) in order to help ensure that $a_n(\lambda)$ outliers that are large in magnitude are representative of the water column and not artifacts associated with ac-s' $a$-tube. Because Monterey Bay is phytoplankton-dominated, we would expect increases in $a_n(\lambda)$ to be accompanied by increases in $b_{bp}(\lambda)$ (and hence $c_n(\lambda)$) [33] and indeed instances of $a > c$ were extremely rare. Furthermore, self-contained SCAs require no

additional measurements (e.g., $b_{bp}(\lambda)$) in order to correct $a_m(\lambda)$, making them ideal for historical datasets that do not contain $b_{bp}(\lambda)$. However, because all self-contained SCAs are undergirded by specific sets of assumptions, we postulate that the chances of selecting an accurate SCA substantially improves with increased understanding of the optical properties associated with the target ecosystem. This increased understanding would be especially true in the absence of reliably measured AOPs (e.g. C-OPS) that could be leveraged to evaluate optical closure.

Constraining $r_w$ with C-OPS was an effective strategy for achieving optical closure with $Mc_{13}$. The fact that constrained $r_w$ decreased with station $\overline{\mathrm{OD}}_{490}$ and not instrument wear and tear (e.g. CST17 and CST18 were sampled two years prior to OCE18 using the same ac-s), indicates that the relationship between $\tilde{b}_b(\lambda)$ and unaccounted $a$-tube scatter changes in response to phytoplankton biomass. As such, the absence of $r_w$ for constraining outputs can explain why $Mc_{08}$, achieved poor optical closure across our stations (Table 3; Fig. 2). $Mc_{08}$ uses the same iterative method as $Mc_{13}$ to process $a_n(\lambda)$ but relies on a static relationship between $\tilde{b}_b(\lambda)$ and unaccounted $a$-tube scatter that would be unable to change in response to environmental conditions (e.g. increased phytoplankton biomass). $Mc_{13}$'s theoretical basis coupled with reliably-measured AOPs to constrain $r_W$ (e.g. C-OPS), increase its potential versatility across different ecosystems. Moreover, its iterative structure frees it from reliance on the underlying sets of assumptions on which self-contained SCAs depend. However, $Mc_{13}$ requires reliable $b_{bp}(\lambda)$ in order to calculate unaccounted

scattering, which limits the historical ac-s data to which it can be applied. Furthermore, our application of $Mc_{13}$ also requires sigma-correcting HS6 measurements prior to processing. This requirement means that $b_{bp}(\lambda)$ would ideally be sigma-corrected using independently measured $a(\lambda)$. Should $a(\lambda)$ be unavailable (e.g. CHR1 and CHR2) $b_{bp}(\lambda)$ would need to be sigma-corrected using $a_m(\lambda)$, diminishing its potential accuracy. We point out that some commercially available instruments, such as ECO-VSF3, measure $b_{bp}(\lambda)$ at a short optical pathlength and therefore do not require a sigma correction. ECO-VSF3 could be advantageous when applying $Mc_{13}$ as its measurements do not require sigma correction. However, Tuchow et al. [5] suggest that ECO-VSF3's diminished spectral resolution (e.g., three $\lambda$'s) may decrease optical closure relative to HS6.

Discrepancies between $a(\lambda)$ and near-surface $a_n(\lambda)$ may stem in part from the fact that during field sampling, our ac-s was configured in such a way to inhibit reliable and accurate sampling of the upper 0.5 m of the water column. Phytoplankton assemblages at medium and high biomass stations were dominated by *Akashiwo sanguinea*, a vertically motile dinoflagellate. These organisms commonly aggregate at the sea surface during the daytime due to phototaxis [4]. It is therefore plausible for the upper 0.5 m of the water column to have higher phytoplankton concentrations than the rest of the water column. Elevated phytoplankton would correspond with higher $a(\lambda)$ in the blue and red, regions in which photosynthetic pigments primarily absorb [4]. Bausell et al. [9] cite the inability of ac-s and HS6 to sample the upper 0.5

m of the water column as an explanation for the lack of optical closure between C-OPS and modeled $[L_W(\lambda)]_N$ at CST18. However, the utility of $Mc_{13}$ and $FL^0$ (to a lesser extent) in achieving optical closure at this station suggests that this explanation is unlikely. We believe that because of its aforementioned insensitivity in the blue and red, $[L_W(\lambda)]_N$ is not as impacted in these spectral regions by increases in phytoplankton concentration. This insensitivity stands in contrast to $\lambda =$ 550-600 nm, the region for which $[L_W(\lambda)]_N$ appears to be much more sensitive to changes in $a(\lambda)$. Here surface $a(\lambda)$ is nearly identical to $Mc_{13}$ and $FL^0$ $a_n(\lambda)$ binned at 0.75 m (Fig. 5e & 5f). Nevertheless, despite $[L_W(\lambda)]_N$'s insensitivity in the blue, we believe discrepancies between $b_{bp}(\lambda)$ sigma-corrected using $a(\lambda)$ ($Mc_{13}$) and $a_n(\lambda)$ ($FL^0$) at CST18 (Fig. 6c) were still sufficient to elevate $Mc_{13}$ $[L_W(\lambda)]_N$ in the blue (albeit modestly), thus improving its optical closure compared with $FL^0$. Similarly, we believe differences between $b_{bp}(\lambda)$ sigma-corrected with $a(\lambda)$ and $a_n(\lambda)$ to be the reason that $Mc_{13}$ $[L_W(\lambda)]_N$ is greater in magnitude than $PR$ $[L_W(\lambda)]_N$ in the green (Figs. 2c & 2d) (therefore exhibiting better optical closure) at OCE18 despite $PR$ having slightly lower near surface $a_n(\lambda)$ in this region (Figs. 5c & 5d).

An alternative explanation for discrepancies between near surface $a_n(\lambda)$ and $a(\lambda)$ at CST18 is that they were caused by the spatial heterogeneity, or 'patchiness' of phytoplankton blooms that can occur over very short spatial scales [34, 35]. Indeed, findings by Bausell et al. [9] support the existence of such patchiness at CST18. Because C-OPS, ac-s/HS6, and buckets were deployed consecutively rather than

concurrently, it is possible that $a(\lambda)$ measured a denser surface aggregate of phytoplankton than C-OPS. While consecutive deployments of instruments could explain optical closure between Hydrolight-modeled and C-OPS measured $[L_W(\lambda)]_N$, this explanation is also improbable. CST17, CST18, and OCE18 all exhibit $a(\lambda) > a_n(\lambda)$ in the blue and red, suggesting that bio-optical constituents commonly aggregate at or near the surface within Monterey Bay watermasses. Optical closure between C-OPS and $Mc_{13}$ and $FL^0$ at this station casts further doubt upon this possibility. Although spatial heterogeneity could also explain how $Mc_{13}$ and $FL^0$ achieved optical closure in the green at OCE18 despite underestimating near surface $a_n(\lambda)$ for $\lambda = 550$-600 nm relative to $a(\lambda)$, we believe that failure to properly calibrate Varian Cary® UV-Vis Spectrophotometer is a more plausible explanation.

## 5. Conclusion

Our study demonstrates that correcting for unaccounted scatter inside ac-s tubes could substantially improve optical closure in coastal ecosystems. It provides evidence that the previously reported lack of optical closure in Monterey Bay between above-water AOPs measured with a profiler and those AOPs modeled from in-situ ac-s and HS6 measurements (especially in the green) are caused by unaccounted scatter inside ac-s tubes. C-OPS possesses the vertical resolution and signal to noise ratio to adequately characterize light fields of coastal watermasses and accurately extrapolate $[L_W(\lambda)]_N$; however, it does so at coarse spectral resolution. Many hyperspectral in-water optical profilers on the other hand (e.g., HP2) lack the vertical resolution and signal to noise

ratio to accurately characterize coastal watermasses [9]. Here, we demonstrate that by correcting unaccounted scattering inside ac-s' flow tubes, we can reliably model hyperspectral $[L_W(\lambda)]_N$ using Hydrolight. The availability of C-OPS serves as a mechanism with which to check modeled $[L_W(\lambda)]_N$. Similarity in shape between modeled and HP2-measured $[L_W(\lambda)]_N$ suggests that spectral shapes of above-water AOPs can be reliably modeled in the visible. Moreover, increased agreement between C-OPS and modeled $[L_W(\lambda)]_N$, relative to C_OPS and HP2 $[L_W(\lambda)]_N$, suggest that modeling may be a better alternative to HP2 when it comes to characterizing watermasses with hyperspectral $[L_W(\lambda)]_N$.

By improving optical closure with C-OPS, we advance towards a best of both worlds scenario: the ability to generate hyperspectral $[L_W(\lambda)]_N$ that reliably and accurately characterizes watermasses with diverse properties. Finally, we conclude that selection of an appropriate SCA for ac-s is ultimately dependent on optical properties of the ecosystem, the types of in-situ data that are available, and goals of the investigator(s). Assuming the availability of high-quality $b_{bp}(\lambda)$ and AOPs we believe $Mc_{13}$ to be the optimal SCA, especially if little is known regarding an ecosystem's optical properties. In the absence of reliable AOPs with which to constrain $r_W$, self-contained SCAs may be preferable, especially if definitive knowledge of an ecosystem's optical properties is available.

## 6. References


1. S. Chandrasekhar, *Radiative Transfer* (Dover Publications Inc, 1960).

2. S. Hooker, J. Morrow, and A. Matsuoka, "The 1% and 1 cm perspective in deriving and validating AOP data products," Biogeosciences Discussions **9** (2012).

3. R. M. Pope, and E. S. Fry, "Absorption spectrum (380–700 nm) of pure water. II. Integrating cavity measurements," Applied optics **36**, 8710-8723 (1997).

4. L. Prieur, and S. Sathyendranath, "An optical classification of coastal and oceanic waters based on the specific spectral absorption curves of phytoplankton pigments, dissolved organic matter, and other particulate materials," Limnology and Oceanography **26**, 671-689 (1981).

5. N. Tuchow, J. Broughton, and R. Kudela, "Sensitivity analysis of volume scattering phase functions," Optics express **24**, 18559-18570 (2016).

6. M. S. Twardowski, E. Boss, J. M. Sullivan, and P. L. Donaghay, "Modeling the spectral shape of absorption by chromophoric dissolved organic matter," Marine Chemistry **89**, 69-88 (2004).

7. M. G. Allan, D. P. Hamilton, B. J. Hicks, and L. Brabyn, "Landsat remote sensing of chlorophyll a concentrations in central North Island lakes of New Zealand," International Journal of Remote Sensing **32**, 2037-2055 (2011).

8. Z. Lee, "Reports of the International Ocean-Colour Coordinating Group," (2006).

9. J. Bausell, and R. Kudela, "Comparison of two in-water optical profilers in a dynamic coastal marine ecosystem," Applied optics **58**, 7319-7330 (2019).

10. L. R. Lain, S. Bernard, and M. W. Matthews, "Understanding the contribution of phytoplankton phase functions to uncertainties in the water colour signal," Optics Express **25**, A151-A165 (2017).

11. J. Pitarch, G. Volpe, S. Colella, R. Santoleri, and V. Brando, "Absorption correction and phase function shape effects on the closure of apparent optical properties," Applied optics **55**, 8618-8636 (2016).

12. C. D. Mobley, L. K. Sundman, and E. Boss, "Phase function effects on oceanic light fields," Applied optics **41**, 1035-1050 (2002).

13. J. M. Sullivan, M. S. Twardowski, J. R. V. Zaneveld, C. M. Moore, A. H. Barnard, P. L. Donaghay, and B. Rhoades, "Hyperspectral temperature and

salt dependencies of absorption by water and heavy water in the 400-750 nm spectral range," Applied Optics **45**, 5294-5309 (2006).

14. Biospherical Instruments Inc., "Compact Optical Profiling System: Hardware User's Manual (Doc 006406UA)," (2010).

15. P. Jørgensen, G. Tilstone, J. Høkedal, and W. Schönfeld, "Intercomparison of Spectral Backscattering Coefficients Measured In Situ Using Several Hydroscat Instruments Results from PlymCal-2 and REVAMP Cruises," in *ESA Special Publication*(2003).

16. R. Röttgers, D. McKee, and S. B. Woźniak, "Evaluation of scatter corrections for ac-9 absorption measurements in coastal waters," Methods in Oceanography **7**, 21-39 (2013).

17. J. T. Kirk, *Light and photosynthesis in aquatic ecosystems* (Cambridge university press, 1994).

18. P. J. Werdell, "An evaluation of Inherent Optical Property data for inclusion in the NASA bio-Optical Marine Algorithm Data set," NASA Ocean Biology Processing Group, Science Systems and Applications, Inc. Document Version **1** (2005).

19. D. McKee, J. Piskozub, and I. Brown, "Scattering error corrections for in situ absorption and attenuation measurements," Optics Express **16**, 19480-19492 (2008).

20. WET Labs Inc., "Spectral Absorption and Attenuation Meter User's Guide," (2008).

21. T. Oishi, "Significant relationship between the backward scattering coefficient of sea water and the scatterance at 120," Applied Optics **29**, 4658-4665 (1990).

22. M. Chami, E. Marken, J. Stamnes, G. Khomenko, and G. Korotaev, "Variability of the relationship between the particulate backscattering coefficient and the volume scattering function measured at fixed angles," Journal of Geophysical Research: Oceans **111** (2006).

23. D. Doxaran, E. Leymarie, B. Nechad, A. Dogliotti, K. Ruddick, P. Gernez, and E. Knaeps, "Improved correction methods for field measurements of particulate light backscattering in turbid waters," Optics express **24**, 3615-3637 (2016).

24. D. McKee, J. Piskozub, R. Röttgers, and R. A. Reynolds, "Evaluation and improvement of an iterative scattering correction scheme for in situ absorption

and attenuation measurements," Journal of atmospheric and oceanic technology **30**, 1527-1541 (2013).

25. J. R. V. Zaneveld, J. C. Kitchen, and C. C. Moore, "Scattering error correction of reflection-tube absorption meters," in *Ocean Optics XII*(International Society for Optics and Photonics1994), pp. 44-55.

26. J. Mueller, J. MuelIer, C. Pietras, S. Hooker, D. Clark, A. M. R. Frouin, and G. Fargion, "Ocean optics protocols for satellite ocean color sensor validation, revision 3, volumes 1 and 2," in *NASA tech. memo*(2002).

27. R. M. Kudela, W. P. Cochlan, T. D. Peterson, and C. G. Trick, "Impacts on phytoplankton biomass and productivity in the Pacific Northwest during the warm ocean conditions of 2005," Geophysical Research Letters **33** (2006).

28. N. A. Welschmeyer, "Fluorometric analysis of chlorophyll a in the presence of chlorophyll b and pheopigments," Limnology and Oceanography **39**, 1985-1992 (1994).

29. E. Arar, "Method 446.0 In Vitro Determination of Chlorophylls a, b, c1+ c2 and//Visible Spectrophotometry. Revision 1.2 National Exposure Research Laboratory," (US Environmental Protection Agency Cincinatti, OH, 1997).

30. R. M. Kudela, N. Garfield, and K. W. Bruland, "Bio-optical signatures and biogeochemistry from intense upwelling and relaxation in coastal California," Deep Sea Research Part II: Topical Studies in Oceanography **53**, 2999-3022 (2006).

31. A. Morel, and L. Prieur, "Analysis of variations in ocean color 1," Limnology and oceanography **22**, 709-722 (1977).

32. J. L. Mueller, S. Brown, D. Clark, B. Johnson, H. Yoon, K. Lykke, S. Flora, M. Feinholz, N. Souaidia, C. Pietras, T. Stone, M. Yarbrough, Y. Kim, and R. Barnes, "Ocean Optics Protocols For Satellite Ocean Color Sensor Validation, Revision 5. Volume VI: Special Topics in Ocean Optics Protocols, Part 2," (2004).

33. Y. Xiong, X. Zhang, S. He, and D. J. Gray, "Re-examining the effect of particle phase functions on the remote-sensing reflectance," Applied optics **56**, 6881-6888 (2017).

34. J. Ryan, M. McManus, R. Kudela, M. L. Artigas, J. Bellingham, F. Chavez, G. Doucette, D. Foley, M. Godin, and J. Harvey, "Boundary influences on HAB

phytoplankton ecology in a stratification-enhanced upwelling shadow," Deep Sea Research Part II: Topical Studies in Oceanography **101**, 63-79 (2014).

35. J. P. Ryan, M. A. McManus, and J. M. Sullivan, "Interacting physical, chemical and biological forcing of phytoplankton thin-layer variability in Monterey Bay, California," Continental Shelf Research **30**, 7-16 (2010).

## CONCLUSION

The findings presented above build upon the ocean color community's capabilities to leverage profiler data towards validating satellite and airborne sensors, as well as algorithm development. Chapter 1 suggests that C-OPS can accurately and reliably characterize a variety of watermass types that occur in Monterey Bay. These watermass types range being low in phytoplankton biomass to being characterized by intense phytoplankton blooms [1, 2]. Conversely, Chapter 1 also suggests that HP2 lacks the sensor sensitivity and the vertical resolution necessary to measure Monterey Bay accurately and reliably. The low signal to noise ratio of HP2, coupled with its low vertical resolution, increase the profiler's susceptibility to platform and environmental perturbations.

Chapter 1 has two major implications for validating above-water sensor measurements and their algorithmic data products. First, the chapter suggests that it may be problematic to rely on HP2 for validating legacy hyperspectral above-water sensors, such as HICO and AVIRIS (e.g., [3, 4]). Although reasonable $[L_W(\lambda)]_N$ estimates in the visible can be obtained by averaging multiple HP2 casts, uncertainty of these above-water measurements range from 10-25% per cast. Second, Chapter 1 infers that measurements taken from different commercially available profiler models are not interchangeable, regardless of whether their channels are centered on the same $\lambda$'s. Because of HP2's high uncertainty above-water, for example, it would be unclear whether $[L_W(\lambda)]_N$ differences between HP2 casts are the result of differences in IOPs or measurement uncertainties in HP2.

Chapter 1 findings improve the potential accuracy and reliability of sensor validation and algorithm development in coastal and inland ecosystems. They also limit the volume of profiler data available for these activities, as they imply that above-water AOPs measured with different profilers should no longer be combined in a single dataset. This particular finding is potentially problematic for algorithm development, as it restricts the ecosystems in which radiometric data products can be validated and recently developed algorithms can be evaluated. It suggests, for example, that an empirical algorithm derived from C-OPS cannot be reliably evaluated in a different ecosystem with measurements taken from HP2. Moreover, Chapter 1 demonstrates the inadequacy of C-OPS in characterizing $[L_W(\lambda)]_N$ spectral shape, due to its low spectral resolution. C-OPS' low spectral resolution precludes its use in validating hyperspectral above-water sensors; it is also an obstacle in validating above-water sensors whose channels do not align with C-OPS. As such, Chapters 2 and 3 leverage modeling to address limitations associated with C-OPS.

Because C-OPS can accurately measure coastal and inland ecosystems, it is ideal for the development of empirical band ratio algorithms, such as end-member approach (EMA). C-OPS is ideal in large part because it can be assumed with reasonable confidence that uncertainties in estimating bio-optical properties stem from the algorithm itself and not the radiometric measurements that undergird it. Chapter 2 demonstrates that evaluating an empirical algorithm using optical data modeled off

of realistic bio-optical properties provides insight into mechanisms responsible for its success. The availability of IOPs and AOPs that achieve optical closure can also help to determine the underlying mechanisms (including phase function) behind an algorithm's success or failure in particular ecosystems. Understanding *why* a particular algorithm is successful can help investigators predict its utility in ecosystems that have not yet been sampled. Additionally, because optical data can be modeled at any $\lambda$, they can also be used to predict the feasibility of applying an algorithm to specific above-water sensors. In this way, Chapter 2 helps to compensate for the aforementioned spectral limitations associated with C-OPS.

The methods outlined in Chapter 2 do not supplant the role of in-situ sampling in extending optical algorithms to particular ecosystems. Rather, Chapter 2 methods enhance effectiveness of in-situ sampling by enabling investigators to pre-screen ecosystems before committing their limited financial, labor, and time resources to them. However, based on Chapter 1, C-OPS' limited spectral resolution may preclude its use in validating radiometric and algorithmic data products for above-water sensors if their channels are not aligned. In this respect, Chapter 3 enhances the capability of C-OPS to validate above-water sensors. The methods presented in Chapter 3, which center on achieving optical closure between C-OPS and modeled $[L_W(\lambda)]_N$ (at $\lambda$'s corresponding to the former), enable the characterization of $[L_W(\lambda)]_N$ at hyperspectral resolution. Observed similarities in spectral shape between $[L_W(\lambda)]_N$ modeled by Hydrolight and $[L_W(\lambda)]_N$ measured by HP2 (see Chapter 1) further suggest that ecosystems can be characterized by modeled

$[L_W(\lambda)]_N$. Chapter 3 methods result in improved agreement with C-OPS compared to methods reported in Chapter 1. Modeled hyperspectral $[L_W(\lambda)]_N$, as demonstrated by Chapter 3, could thus be leveraged to validate a multitude of above-water sensors, including hyperspectral above-water sensors, in sampling coastal ecosystems.

As next-generation satellites and unmanned aerial vehicles (UAVs) become more available to the ocean color community, so too will the need for reliable ground truth measurements from an assortment of costal and inland ecosystems. Moving forward, this dissertation lays important groundwork for characterizing and monitoring these important ecosystems from above. Once an investigator has determined a target ecosystem to monitor, he/she can use Chapter 2 as a template for determining which algorithms are likely to adequately characterize it. Upon making a satisfactory assessment, C-OPS, ac-s and HS6 can then be deployed contemporaneously in order to model $[L_W(\lambda)]_N$ hyperspectrally. Modeled $[L_W(\lambda)]_N$, in turn, would be used to validate the radiometric and algorithmic data products of these novel sensors.

Moving forward, the approaches outlined in Chapters 1-3 could be advanced by technological innovations in instrument design. First, many present-day instruments, such as ac-s and HS6, do not measure effectively in the UV or NIR, which relegates hyperspectral modeling to the visible. Second, physical dimensions of ac-s and HS6 hinder their ability to measure the upper meter of the water column

when they are affixed to scaffolding and deployed off of a ship to measure vertical profiles (e.g., Chapters 1 & 3). Although these limitations do not appear limiting in Monterey Bay in terms of optical closure, they could become a factor when vertically profiling habitats that are characterized by shallow water (e.g., 1-3 m) or an upper meter that is optically distinct from the rest of the water column. With these issues in mind, the ocean color community could benefit from more compact IOP meters with channels centered in the UV and NIR as well as the visible. Absorption and backscattering meters would also benefit from shorter optical pathlengths, so long as they do not come at the expense of spectral resolution (e.g., [5]). Shorter optical pathlength would likely improve accuracy and reliability of modeled hyperspectral $[L_W(\lambda)]_N$, especially if contemporaneous C-OPS measurements are unavailable. And finally, the advent of an in-water optical profiler that samples with the sensitivity and vertical resolution of C-OPS but does so hyperspectrally, would provide a 'best of both worlds' scenario in terms of developing optical algorithms, and in terms of validating radiometric and algorithmic data products of above-water sensors.

## References

1. W. Graham, J. Field, and D. Potts, "Persistent "upwelling shadows" and their influence on zooplankton distributions," Marine Biology **114**, 561-570 (1992).

2. L. K. Rosenfeld, F. B. Schwing, N. Garfield, and D. E. Tracy, "Bifurcated flow from an upwelling center: a cold water source for Monterey Bay," Continental Shelf Research **14**, 931-964 (1994).

3. S. L. Palacios, R. M. Kudela, L. S. Guild, K. H. Negrey, J. Torres-Perez, and J. Broughton, "Remote sensing of phytoplankton functional types in the coastal ocean from the HyspIRI Preparatory Flight Campaign," Remote Sensing of Environment **167**, 269-280 (2015).

4. J. P. Ryan, C. O. Davis, N. B. Tufillaro, R. M. Kudela, and B.-C. Gao, "Application of the hyperspectral imager for the coastal ocean to phytoplankton ecology studies in Monterey Bay, CA, USA," Remote Sensing **6**, 1007-1025 (2014).

5. N. Tuchow, J. Broughton, and R. Kudela, "Sensitivity analysis of volume scattering phase functions," Optics express **24**, 18559-18570 (2016).